



Elliptic Integrals and the Schwarz-Christoffel Transformation

W. C. HASSENPFUG

Department of Mechanical Engineering, University of Stellenbosch
Stellenbosch, South Africa

(Received December 1996; accepted January 1997)

Abstract—The real elliptic integrals of the first and second kind in Jacobi's normal form are computed efficiently, using the convolution number in conjunction with the method of Frobenius. For this purpose certain treatments of the Laurent series are included. Different regions of convergence on the real axis are determined, and for each one a different series is developed. The real elliptic integral of the third kind is solved within a limited parameter plane by the same method.

The integral of the Schwarz-Christoffel transformation is solved in the complex variable by complex convolution number algebra, using the unit disk as mapping region. Different regions of convergence of Frobenius, Laurent, and Taylor series are determined to cover the whole disk. The complex evaluation of the elliptic integral of the third kind is included. A Schwarz-Christoffel formula for an infinite periodic mapping is given. The solutions for exterior, interior, periodic, and cyclic polygons are separately treated. Examples of several polygon mappings are presented graphically, and compared with previous numerically integrated solutions.

The parameter problem is solved by the Newton-Raphson method, using a quotient matrix as approximation for the Jacobian matrix. The coordinate relations are simplified by using an overdetermined system. An exact analytical Jacobian matrix is computed, solving Leibniz' derivative of the Schwarz-Christoffel integral, and results are compared with the approximate quotient matrix method.

Keywords—Schwarz-Christoffel transformation, Elliptic integrals, Conformal mapping, Convolution number, Series expansions.

1. INTRODUCTION

The Schwarz-Christoffel transformation (SCT) maps a polygon on a halfplane or a circular disk. The SCT is formulated as an integral that leads only in the simplest cases to elliptic integrals; the general case is usually considered unsolvable, in the sense that it cannot be expressed in terms of well-known and tabulated functions. The advancement in computers that has made finite difference and finite element solutions possible can now be used to find the analytical solutions, albeit not in the restricted classic sense.

Analytical methods dominated in the solution of physical problems from the beginning of analysis centuries ago. As problems became more and more demanding, analytical functions were developed, resulting in numerous special functions, recorded in mathematical treatises and handbooks. Yet the struggle to formulate solutions in terms of known functions became harder as accurate solutions of real problems were demanded.

Already from 1905, practically minded Carl Runge developed the numerical integration techniques, realizing that a general differential equation will probably never be solved analytically. Since then, analytic and numerical methods have always run parallel. With the advent of the computer, numerical methods have overtaken analytical methods, since about the 1960's.

The Schwarz-Christoffel transformation was a popular analytic tool in fluid problems with polygon boundaries, in free streamline problems, and in plane elastic systems. Interest in the

analytic solution of the SCT stopped around the 1960's, when analytical methods were overtaken by purely numerical methods in the solution of partial differential equations. From here on, roads of numerical and analytical solution methods parted.

Along a different path of development, the computer has also been used to handle analytical methods in what are called symbolic computer languages. Yet these still rely on classic well-known analytic functions.

Since the 1970's, numerical methods have solved the SCT successfully [1,2]. One of the best known and popular methods was developed by Trefethen [3], particularly well explained, also discussed and advocated by Henrici [4]. That method is developed as a computer package, called SCPACK, which is freely available from its author. Variations and improvements of the numerical solution continue to appear [5–8]. An improvement for elongated regions, using Trefethen's numerical integration, is given in [9]. An application package with unlimited scope for MATLAB¹ is given in [10].

The result is that the SCT is used more frequently again, but now in the fields of hybrid micro-electronics [11], VLSI design [12], magnetics [13–15], microwave theory [16,17], electromagnetic fields [18], but also in fracture mechanics [19]. Many of these workers use their own numerical techniques, others use Trefethen's SCPACK, i.e., [11,12,19].

In this paper, we present an analytic method for the computation of elliptic integrals and the solution of the SCT, turning the clock back by some 20 years. There does not seem to be a need of a new method any more, but we present our method as an alternative method to use the computer to achieve the analytical solution and its numerical evaluation. From the crossroads, we turn the clock forward again on the alternate analytical path, by how much we cannot estimate ourselves.

The analytical solution of a physical problem consists of selecting suitable functions from the set that has been developed during the last three centuries, and then to determine the coefficients. To evaluate, the functions need to be evaluated numerically. In the SCT the functions are generally not available; they are actually new functions defined by the SCT. An efficient and general method to evaluate such new functions is by expansion in Taylor series. Computations are done on the sequence of coefficients which are regarded as a number, called convolution number [20]. The operations on the sequences are treated as operations on a number with convolution algebra [20], making the expansion problem a simple algebraic problem, easily implemented on a computer.

Different well-known routines for the computation of the three basic elliptic integrals, $F(\phi, k)$, $E(\phi, k)$, $\Pi(\phi, k)$, are available, notably in the handbooks [21,22] or in treatises on applications [23,24]. Much effort has been made to write more efficient routines, as in [25,26]. Some more efficient ones were developed recently in [27], where many more references are given. To program these may be quite an effort in itself, but it does not solve the problem if the elliptic integrals are not one of the three basic types. In that case, the relations with the three basic types must first be found, as in the tables of [21]. But then those integrals may involve many times the computational effort of one elliptic integral, the worst case occurring when the original integral is expressed as infinite series of elliptic integrals. Using the convolution number as computational tool, all elliptic integrals are solved directly by the same method.

The range of integration of elliptic integrals and the SCT approaches or includes singular points. Then the method of Frobenius produces an analytic solution near the singularity [28], which is used in conjunction with the convolution number, as was suggested in [20]. The Frobenius expansion is particularly well suited to singular points which are infinities, which are such a problem in numerical integration. For this purpose, the range of integration near, or including, the known singular points must be partitioned into suitable regions of convergence for the practical application of series. It was previously suggested [29] that we can approximate to any required accuracy by using enough terms of a single central Taylor series. However, even a good

¹MATLAB is a registered trademark of The MathWorks, Inc.

approximation would need a few thousand terms, and the singularities can still not be computed, even less so if they are infinities. It is shown in the following how the convolution number is used to develop additional Frobenius and Laurent series to cover the whole range efficiently. For each value of the parameters, the series can be developed easily on a personal computer. All corner-points are singularities and need Frobenius disks, except the special case $\alpha = -1$ and winding points, $\alpha = -2 \dots$. But singularities need not be infinities, as suggested in [11].

For the real elliptic integral, a region on the real line is partitioned into line segments on which the chosen series converge. For the SCT, the unit disk is chosen as mapping region, so that the whole range can be covered by a finite number of circular convergence regions, the number of which depends on the number and position of the singular points on the circle. An efficient covering is then achieved by using Frobenius, Laurent, and Taylor series.

The relation of the coordinates of the polygon corners with the position of the singular points on the circle is called the parameter problem. This is solved by a Newton-Raphson iteration.

The solution is then available in analytical form, in the sense as described in [20].

2. PRELIMINARIES

2.1. Binomial Theorem

It is worthwhile to add the binomial formula to the convolution number routines of [20], because the SCT formula consists of factors which are binomials to some power. The binomial formula is simpler than the general convolution routine that computes $\bar{c}^{-*\alpha}$, as described in [20], because the pointer convolution numbers in that routine are not needed for the simple binomial. Ordinary convolution numbers are then sufficient for the solution of the SCT.

Generally for

$$f(z) \equiv (a_0 + a_1 z)^\alpha = \underline{Z} \cdot \bar{f}, \quad (2.1)$$

the coefficients are given by the recurrence formula

$$f_0 = a_0^\alpha, \quad f_i = f_{i-1} \frac{\alpha - (i-1)}{i a_0} a_1, \quad \text{for } i = 1, \dots, n. \quad (2.2)$$

2.2. Laurent Series

There are many occasions where the Laurent series can be used to obtain a more efficient covering of a region within a range of interest than the Taylor series. We will therefore need symbols to include Laurent series in expansions, even though convolution algebra cannot be done on a sequence of Laurent coefficients [20]. For our purposes, the full-Laurent series is split into two half-infinite series, one of which is a half-infinite Laurent series, called *half-Laurent series*, and the other is a Taylor series. The half-Laurent series is then a Taylor series of the inverted variable.

We introduce the new symbol for the half-Laurent series, for numerical purposes truncated to n terms,

$$\frac{a_1}{z} + \frac{a_2}{z^2} + \dots + \frac{a_n}{z^n} = \underline{Z} \cdot \tilde{a} \quad (2.3)$$

with the definitions similar to the Taylor convolution number,

$$\underline{Z} \equiv \left[\frac{1}{z}, \frac{1}{z^2}, \dots, \frac{1}{z^n} \right], \quad (2.4)$$

$$\tilde{a} \equiv \{a_1, a_2, \dots, a_n\}, \quad (2.5)$$

where we call the sequence \tilde{a} the *Laurent number*. In equation (2.3) it acts as a column vector. With the transformation $s = 1/z$, the half-Laurent series can be expressed as a Taylor series

$$a_1 s + a_2 s^2 + \cdots + a_n s^n = \underline{S} \cdot \bar{a}, \quad (2.6)$$

where \bar{a} is the *Taylor convolution number*, which is the same sequence as \tilde{a} but with a different meaning. It is this meaning that distinguishes \tilde{a} and \bar{a} ; in particular, the differentiation and integration is different. Otherwise, the two numbers are stored the same way in a computer, and no negative subscripts are used.

The algebra of Laurent numbers is defined by the corresponding algebra of Taylor series, e.g., multiplication

$$\underline{V} \cdot \tilde{a} \times \underline{V} \cdot \tilde{b} = \underline{V} \cdot \tilde{a} * \tilde{b} \quad (2.7)$$

is equivalent to the product of Taylor convolution numbers

$$\underline{Z} \cdot \bar{a} \times \underline{Z} \cdot \bar{b} = \underline{Z} \cdot \bar{a} * \bar{b}.$$

The distinction is only necessary if both Taylor and half-Laurent series occur in the same context.

A full-Laurent series is then expressed as the sum of a half-Laurent series and a Taylor series

$$\frac{a_{1n}}{z^n} + \cdots + \frac{a_{12}}{z^2} + \frac{a_{11}}{z} + a_{20} + a_{21}z + a_{22}z^2 + \cdots + a_{2n}z^n = \underline{Z} \cdot \tilde{a}_1 + \underline{Z} \cdot \bar{a}_2, \quad (2.8)$$

where the constant a_0 is always taken into the Taylor series.

What happens typically in elliptic integrals and the SCT is that the function to be integrated is given in factors $a(z) = a_1(z)a_2(z)$, of which the first part is expanded in a half-Laurent series and the second in a Taylor series, both in z about same the point $z = 0$, which we express now as

$$a(z) = a_1(z) \times a_2(z) = \underline{Z} \cdot \tilde{a}_1 \times \underline{Z} \cdot \bar{a}_2, \quad (2.9)$$

which has to be expressed as a single full-Laurent series

$$a_1(z) \times a_2(z) = b_1(z) + b_2(z) = \underline{Z} \cdot \tilde{b}_1 + \underline{Z} \cdot \bar{b}_2 \equiv b(z). \quad (2.10)$$

Although the functions $a(z)$ and $b(z)$ are analytically the same, we give their different forms different names.

In contrast to the convolution number, each Laurent coefficient in equation (2.10) consists of an infinite sum of the terms of \tilde{a}_1 and \bar{a}_2 . The best we can do numerically is not to lose any of the products of the truncated series that contribute to the product, which are shown in Figure 2.1.

The multiplication and partitioning in half-Laurent and Taylor coefficients of equation (2.10) is then done according to

$$b_{1i} = \sum_{k_1}^{k_2} a_{1k} a_{2k-i}, \quad \text{for } i = i_1, \dots, i_2, \quad (2.11)$$

where

$$\begin{aligned} i_1 &= \max(1, l_1 - m_2), & i_2 &= \max(0, m_1 - l_2), \\ k_1 &= \max(l_1, l_2 + i), & k_2 &= \min(m_1, m_2 + i), \end{aligned}$$

and

$$b_{2i} = \sum_{k_1}^{k_2} a_{1k} a_{2k+i}, \quad \text{for } i = i_1, \dots, i_2, \quad (2.12)$$

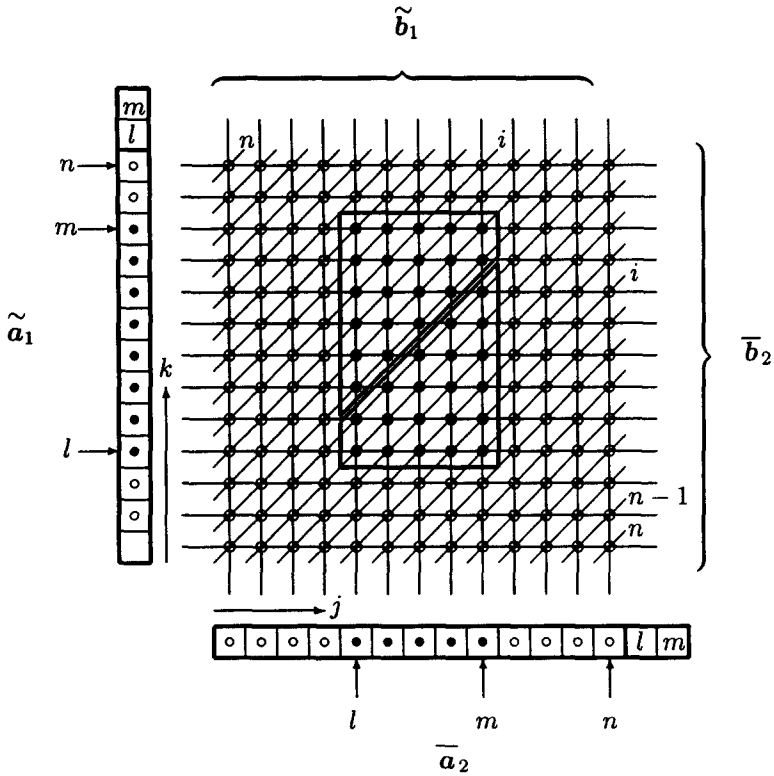


Figure 2.1. Convolution number multiplication $\tilde{a}_1 * \bar{a}_2 = [\tilde{b}_1, \bar{b}_2]$.

where

$$\begin{aligned}
 i_1 &= \max(0, l_2 - m_1), & i_2 &= \max(-1, m_2 - l_1), \\
 k_1 &= \max(l_1, l_2 - i), & k_2 &= \min(m_1, m_2 - i),
 \end{aligned}$$

and the pointers l_1, m_1, l_2, m_2 are taken from the numbers \tilde{a}_1 and \bar{a}_2 , see [20].

In Figure 2.1, the parts that contribute to the two different numbers are shown enclosed by the thick lines. Note that in Figure 2.1 we have shown \tilde{a} with an empty space in the 0-position, according to equation (2.3), but we allow for an occupied position there before multiplication and separation, which occurs from the development of \tilde{a} by a binomial expansion.

Symbolically we express the operations of equations (2.11) and (2.12) by the notation

$$\tilde{a}_1 * \bar{a}_2 = [\tilde{b}_1, \bar{b}_2], \tag{2.13}$$

or by the simpler symbol

$$\tilde{a}_1 * \bar{a}_2 \Rightarrow \tilde{b}_1, \bar{b}_2. \tag{2.14}$$

The relation between equations (2.13),(2.14) with (2.9) and (2.10) is formally expressed by

$$\underline{Z} \cdot \tilde{a}_1 \times \underline{Z} \cdot \bar{a}_2 = \underline{\underline{Z}} \cdot \tilde{a}_1 * \bar{a}_2 = \underline{\underline{Z}} \cdot \tilde{b} = \underline{\underline{Z}} \cdot \tilde{b}_1 + \underline{Z} \cdot \bar{b}_2. \tag{2.15}$$

Contrary to convolution numbers, Laurent coefficients obtained by this method are not exact; each coefficient is defined by an infinite series.

The general integration of a half-Laurent series

$$a(z) = \frac{a_1}{z} + \frac{a_2}{z^2} + \cdots + \frac{a_n}{z^n} \equiv \underline{Z} \cdot \tilde{a} \quad (2.16)$$

to $b(z) = \int a(z) dz$ results in

$$\begin{aligned} b(z) &= a_1 \log z + \frac{-a_2}{z} + \frac{1-a_3}{2z^2} + \cdots + \frac{1-g_n}{nz^{n-1}} \\ &\equiv a_1 \log z + \frac{b_1}{z} + \frac{b_2}{z^2} + \cdots + \frac{b_{n-1}}{z^{n-1}} = a_1 \log z + \underline{Z} \cdot \tilde{b}, \end{aligned} \quad (2.17)$$

so that the coefficients of the new Laurent number are computed as

$$b_i = -\frac{a_{i+1}}{i}, \quad \text{for } i = i_1, \dots, i_2, \quad (2.18)$$

where i_1 and i_2 are determined from the pointers in \tilde{a} by

$$i_1 = \max(2, l_a) - 1, \quad i_2 = \max(2, m_a) - 1.$$

We write the integration formally without the logarithmic term as

$$\tilde{b} = \int \tilde{a}. \quad (2.19)$$

When the Taylor and Laurent series are considered as special cases of Frobenius series, discussed in the next section, the arrangement of the coefficients of the integrated series will be slightly different.

2.3. Frobenius Series

Series solutions of functions that are obtained by the method of Frobenius about a singular point are often called Frobenius series, e.g., see [30].

For our purposes, we will call any expansion consisting of a Taylor or half-Laurent series in z , multiplied a fractional power z^α , a Frobenius series, in particular, a Frobenius-Taylor series or Frobenius-Laurent series if the distinction is necessary, even when the series is not expanded about the singular point. For example, the following expansion

$$\sqrt{1+z} = z^{3/2} \left(\frac{1}{z} + \frac{1}{2} \frac{1}{z^2} - \frac{1}{2 \cdot 4} \frac{1}{z^3} + \frac{1 \cdot 3}{2 \cdot 4 \cdot 6} \frac{1}{z^4} \cdots \right) \quad (2.20)$$

is a Frobenius-Laurent series about the point $z = 0$, but the singular point is at $z = -1$, and the series converges outside the disk $|z| > 1$. The notation which separates functions and numbers of equation (2.20) is

$$\sqrt{1+z} \equiv z^{3/2} h(z) = z^{3/2} \times \underline{Z} \cdot \tilde{h}. \quad (2.21)$$

The Frobenius-Taylor series of the form

$$\begin{aligned} a_F(z) &= z^\alpha a(z) = z^\alpha (a_0 + a_1 z + a_2 z^2 + \cdots) \\ &= z^\alpha \underline{U} \cdot \bar{a} \end{aligned} \quad (2.22)$$

is integrated to

$$\begin{aligned} \int a_F(z) dz &\equiv b_F(z) = b_{F0} + z^{\alpha+1} \left(\frac{a_0}{\alpha+1} + \frac{a_1}{\alpha+2} z + \frac{a_2}{\alpha+3} z^2 + \cdots \right) \\ &\equiv b_{F0} + z^{\alpha+1} (b_0 + b_1 z + b_2 z^2 + \cdots) \\ &= b_{F0} + z^{\alpha+1} \underline{Z} \cdot \bar{b} \\ &= b_{F0} + z^{\alpha+1} b(z), \end{aligned} \quad (2.23)$$

where $a(z)$ and $b(z)$ are the Taylor series factors. Note how the factor in front of the series is constructed to cause a well-determined form when $-1 < \alpha < 0$. We have not made provision for the constant of integration, b_{F0} , to be contained in the convolution number \bar{b} as in the case of the Taylor convolution number.

Therefore a Frobenius-Taylor integration routine is programmed for the coefficients

$$b_i = \frac{a_i}{(\alpha + i + 1)}, \quad \text{for } i = l_a, \dots, m_a, \quad (2.24)$$

and we write the integration formally without fractional power factor as

$$\bar{b} = \int_{(\alpha)} \bar{a}. \quad (2.25)$$

There is one exception to the formula of equation (2.24). It may easily happen that $\alpha = -m$ is a negative integer, in which case the integral of the $(m-1)^{\text{th}}$ term is $\int a_{m-1} z^{-1} dz = a_{m-1} \log z$. In numerical computation it is not good enough to distinguish only between the exponent -1 and $\neq -1$, because at ≈ -1 large inaccuracy already occurs. Therefore the integration of the $(m-1)^{\text{th}}$ term will be done different as soon as $\alpha \approx -\text{integer } m$. Integrate the term

$$\int z^\alpha z^{m-1} dz = C + \frac{z^{\alpha+m}}{\alpha+m} = C + \frac{1}{\alpha+m} e^{(\alpha+m) \log z}$$

and expand the exponential. Choosing the constant $C = -1/(\alpha+m)$, we arrive at the expansion

$$\begin{aligned} \int z^\alpha z^{m-1} dz &= \int z^{(\alpha+m-1 \approx -1)} dz \\ &= \log z + \frac{1}{2}(\alpha+m)(\log z)^2 + \frac{1}{2 \cdot 3}(\alpha+m)^2(\log z)^3 + \dots \end{aligned} \quad (2.26)$$

This series-term is then multiplied by the coefficient a_{m-1} and added to the remaining terms of equation (2.23). The solution differs from equation (2.23) by the constant C , but this is compensated by the determination of b_{F0} .

The symbolic integration of equation (2.25) will then not include the term a_{m-1} , and the integration of a Frobenius-Taylor series is written as

$$\int z^\alpha \times \underline{Z} \cdot \bar{a} dz = b_{F0} + h(\log z) + z^{\alpha+1} \times \underline{Z} \cdot \bar{b}. \quad (2.27)$$

For the applications, it is convenient not to take the one factor of z in $z^{\alpha+1}$ of the integral into the series, because it allows for the proper condition when $-1 < \alpha < 0$.

The same method can be applied to the Frobenius-full-Laurent series by pulling the term $z^{\alpha-n}$ to the front, but in our computer implementation the full-Laurent series is stored in two parts, each with a coefficient sequence of length n . Therefore a separate integration for the Frobenius-Laurent series is used.

The Frobenius-Laurent series of the form

$$\begin{aligned} a_F(z) &= z^\alpha a(z) = z^\alpha \left(\frac{a_1}{z} + \frac{a_2}{z^2} + \frac{a_3}{z^3} + \dots \right) \\ &= z^\alpha \underline{Z} \cdot \tilde{a} \end{aligned} \quad (2.28)$$

is integrated to

$$\begin{aligned} b_F(z) &= z^{\alpha+1} \left(\frac{a_1}{\alpha} \frac{1}{z} + \frac{a_2}{\alpha-1} \frac{1}{z^2} + \frac{a_3}{\alpha-2} \frac{1}{z^3} + \dots \right) \\ &\equiv z^{\alpha+1} \left(\frac{b_1}{z} + \frac{b_2}{z^2} + \frac{b_3}{z^3} + \dots \right) \\ &= z^{\alpha+1} \underline{Z} \cdot \tilde{b} \\ &= z^{\alpha+1} b(z), \end{aligned} \quad (2.29)$$

where $a(z)$ and $b(z)$ are the half-Laurent series factors. The integration constant is left to the Frobenius-Taylor part.

The Frobenius-Laurent integral coefficients are determined by

$$b_i = \frac{a_i}{(\alpha - i + 1)}, \quad \text{for } i = l_a, \dots, m_a, \quad (2.30)$$

and the integration is formally formally written without fractional power factor as

$$\tilde{b} = \int_{(\alpha)} \tilde{a}. \quad (2.31)$$

The same exception is made when $\alpha \approx +$ integer m , including 0. The integral of the $(m + 1)^{\text{th}}$ term is

$$\int z^\alpha \frac{1}{z^{m+1}} dz = \log z + \frac{1}{2}(\alpha - m)(\log z)^2 + \frac{1}{2 \cdot 3}(\alpha - m)^2(\log z)^3 + \dots \quad (2.32)$$

The term of equation (2.32) is multiplied by the coefficient a_{m+1} and added to the remaining terms of equation (2.29). Again, the symbolic integration in equation (2.31) does not include the coefficient a_{m+1} , and the integration is formally written as

$$\int z^\alpha \times \underline{\tilde{z}} \cdot \tilde{a} dz = b_{F0} + h(\log z) + z^{\alpha+1} \times \underline{\tilde{z}} \cdot \tilde{b}. \quad (2.33)$$

This integration includes the ordinary case of a half-Laurent series, which is equivalent to the case $\alpha = 0$, but the form is slightly different from equation (2.17).

In the applications, α is a real number, but care must be taken to take the correct complex branch of $z^{\alpha+1}$ and $\log z$. Integrals of Frobenius series can always be integrated further, but then with increasing number of products of the form $z^n(\log z)^m$.

2.4. Numerical Radius of Convergence

Assuming a computer with a particular number of digits, e.g., seven digits for a personal computer in single precision, the accuracy of the evaluated function by series in z depends on both the variable to radius of convergence ratio, r_c , and the number n of coefficients of the truncated series, a smaller radius r_c requiring a smaller number of coefficients. On the other hand, the number of regions to be covered in a range of interest increases with smaller r_c , requiring more series expansions. A study of the optimum number n and the corresponding r_c is beyond the scope of this paper. The radius used to achieve machine accuracy for the chosen length of convolution number is called numerical radius of convergence in [20]. We have found that for a 7-digit computer, we can achieve machine accuracy in all cases with a Taylor series when

$$r_c = 0.7, \quad n = 40, \quad (2.34)$$

which coincides with experiments in [20, p. 89]. Therefore a Taylor series with theoretical radius of convergence of r_a will have a numerical radius of convergence of

$$r_t = 0.7 r_a. \quad (2.35)$$

While in most cases a length $n = 25$ at $r_c = 0.7$ was found to be accurate, corresponding to [20], in some cases this did not achieve 7-digit accuracy. In most cases, a length of $n = 12$ to 20 is sufficient for practical purposes, meaning 3- to 6-digit accuracy. In any case, we will use the fixed number of $r_c = 0.7$ throughout, which has a profound influence on the partition of a range of interest into separate regions. If less accuracy is required, the same partition into regions can

be kept and simply the number of coefficients n decreased. The length n is always used as a programmable variable.

As an example of the efficiency of a small numerical radius, the value of π can be computed with a 7-digit machine by $6 \times$ the series $\arcsin(1/2)$, which converges numerically to full 7-digit accuracy at 8 terms. At the edge of the convergence disk, the $\arcsin(1)$ series converges numerically only after 30000 terms, and only to 3-digit accuracy. The well-known series $4 \arctan(1)$ needs 14000 terms to converge numerically to 5-digit accuracy.

If we consider a half-Laurent series in z , with a theoretical inner radius of convergence of r_a , then by transforming $s = 1/z$, the Taylor series in s will by equation (2.35) have a numerical radius of convergence of $0.7/r_a$. If the Taylor part of a full-Laurent series has a theoretical radius of convergence of r_b , then the numerical inner radius r_i and outer radius r_o of the annulus of convergence of the full-Laurent series are

$$r_i = \frac{r_a}{0.7}, \quad r_o = 0.7 r_b. \tag{2.36}$$

From equation (2.36) it is clear that the numerical annulus of convergence of the Laurent series shrinks to zero as soon as r_a and r_b come so close together that $r_a/0.7 = 0.7 r_b$, or

$$\frac{r_a}{r_b} = 0.7^2 = 0.49. \tag{2.37}$$

This corresponds to the known fact that a Fourier series, which is a mapping of the Laurent series, needs a large number of terms if the singularities of the function are close to the real line, which is a mapping of the mean radius of the annulus.

The partition of the range of interest into numerical regions of convergence will be done according to the limits given by equations (2.35) and (2.36).

As we have developed the program over a number of years, changes were made according to the available computers. The first SC integrals were solved on an HP 9836, which has 12-digit accuracy. As the IBM PC took over with 7 digits, we became aware of the problem caused by large numbers at the end of a series, caused by the magnitude of the variable rather than numerical radius. To eliminate this problem, a scaled variable is used. The use of scaled variables in the convolution algebra is discussed in Appendix A.

2.5. A Binomial Expansion by Biconvolution Number

The biconvolution number \overline{G} is defined in [20] as the array of coefficients of the expansion of a function $g(u, v)$ of the two variables u and v in a double series as

$$g(u, v) = \underline{u} \cdot \overline{G} \cdot \overline{v}.$$

To conform to the previous sections, we may also use the notation

$$g(u, v) = \underline{U} \cdot \overline{G} \cdot \overline{V} \tag{2.38}$$

with a slight difference in interpretation. The \underline{u} and \overline{v} indicate rather a particular value of the variable, while \underline{U} and \overline{V} indicate a complete base. In a particular application, we require the expansion

$$(a_0 + a_1 u)^{sv} = \underline{U} \cdot \overline{G} \cdot \overline{V} \tag{2.39}$$

with generally complex constants a_0, a_1 , but restricted to real parameter s and real variable v . The computation follows the binomial expansion, separating u and v conveniently,

$$\begin{aligned}
(a_0 + a_1 u)^{\cdot sv} &= a_0^{\cdot sv} \begin{pmatrix} 1 \\ +u a_0^{-1} a_1 sv \\ +u^2 a_0^{-2} a_1^2 \frac{sv(sv-1)}{2} \\ +u^3 a_0^{-3} a_1^3 \frac{sv(sv-1)(sv-2)}{3 \cdot 2} \\ \vdots \end{pmatrix} \\
&= a_0^{\cdot sv} \begin{pmatrix} 1 \\ +u \underline{c}^1 \cdot \bar{V} \\ +u^2 \underline{c}^2 \cdot \bar{V} \\ +u^3 \underline{c}^3 \cdot \bar{V} \\ \vdots \end{pmatrix} = a_0^{\cdot sv} \{1 \ u \ u^2 \ u^3\} \cdot \begin{bmatrix} \underline{c}^0 \\ \underline{c}^1 \\ \underline{c}^2 \\ \underline{c}^3 \\ \vdots \end{bmatrix} \cdot \bar{V} \\
&\equiv a_0^{\cdot sv} \times \underline{U} \cdot \underline{\bar{C}} \cdot \bar{V}, \tag{2.40}
\end{aligned}$$

where \underline{c}^i are row-convolution numbers. They are determined by the recursion

$$\begin{aligned}
\underline{c}^i &= a_0^{-1} a_1 \underline{c}^{i-1} * \underline{b}^i \\
\underline{b}^i \cdot \bar{V} &= \frac{(sv+i-1)}{i} = \left\{ \frac{(-i+1)}{i}, \frac{1}{i} \right\} \cdot \bar{V}. \tag{2.41}
\end{aligned}$$

To distinguish quite clearly between superscripts and exponents in the equations (2.40),(2.41) above, the exponents are indicated with a leading \cdot (the indices of u can be interpreted as exponents and superscripts at the same time!). The factor in front is expanded

$$\begin{aligned}
a_0^{\cdot sv} &= \left(|a_0| e^{\hat{i} \phi} \right)^{\cdot sv} \\
&= |a_0|^{\cdot sv} \times \underline{e} \cdot \bar{V} \equiv \underline{a} \cdot \bar{V}, \tag{2.42}
\end{aligned}$$

where $|a_0|$ is the amplitude² and ϕ the phase of the complex number a_0 . The real property of s and v has been used in equation (2.42). For the sake of completeness we note, however, that an extension to complex number s and complex variable is readily made, albeit with more computational effort. The convolution number \underline{e} is the Taylor transform of the exponential function $\cos(\phi sv) + \hat{i} \sin(\phi sv)$. Care must be taken to take the proper branch for the phase ϕ . The biconvolution number $\underline{\bar{G}}$ is now determined by

$$\underline{a} \cdot \bar{V} \times \underline{U} \cdot \underline{\bar{C}} \cdot \bar{V} = \underline{U} \cdot \begin{bmatrix} \underline{a} * \underline{c}^0 \\ \underline{a} * \underline{c}^1 \\ \underline{a} * \underline{c}^2 \\ \underline{a} * \underline{c}^3 \\ \vdots \end{bmatrix} \equiv \underline{U} \cdot \underline{\bar{G}} \cdot \bar{V}. \tag{2.43}$$

It is convenient to write equation (2.43) formally as

$$\underline{a} \cdot \bar{V} \times \underline{U} \cdot \underline{\bar{C}} \cdot \bar{V} = \underline{U} \cdot \underline{\bar{A}} \cdot \bar{V} \times \underline{U} \cdot \underline{\bar{C}} \cdot \bar{V} = \underline{U} \cdot \underline{\bar{A}} * \underline{\bar{C}} \cdot \bar{V} = \underline{U} \cdot \underline{\bar{G}} \cdot \bar{V}, \tag{2.44}$$

²The term *amplitude* is used here for the absolute value of a complex number.

but it may even be computationally convenient to construct the biconvolution number

$$\underline{\bar{A}} = \left[\begin{array}{c} \underline{a} \\ -\frac{\underline{a}}{0} - \end{array} \right]. \quad (2.45)$$

2.6. Partial Frobenius Integration

The bivariate Frobenius-Taylor series of the form

$$a_F(u, v) = u^\alpha \underline{U} \cdot \underline{\bar{A}} \cdot \underline{\bar{V}} \quad (2.46)$$

is partially integrated over the variable u as in Section 2.3, with $\underline{a}^i \cdot \underline{\bar{V}}$ as factors,

$$\begin{aligned} \int a_F(u, v) du &= c^F(v) + u^{\alpha+1} \left(\begin{array}{c} \frac{1}{\alpha+1} \underline{a}^0 \cdot \underline{\bar{V}} \\ u \frac{1}{\alpha+2} \underline{a}^1 \cdot \underline{\bar{V}} \\ u^2 \frac{1}{\alpha+3} \underline{a}^2 \cdot \underline{\bar{V}} \\ \vdots \end{array} \right) \\ &= \underline{c}^F \cdot \underline{\bar{V}} + u^{\alpha+1} \left(\begin{array}{c} \underline{b}^0 \cdot \underline{\bar{V}} \\ u \underline{b}^1 \cdot \underline{\bar{V}} \\ u^2 \underline{b}^2 \cdot \underline{\bar{V}} \\ \vdots \end{array} \right) \\ &= \underline{c}^F \cdot \underline{\bar{V}} + u^{\alpha+1} \{ 1 \ u \ u^2 \ u^3 \} \cdot \left[\begin{array}{c} \underline{b}^0 \\ \underline{b}^1 \\ \underline{b}^2 \\ \underline{b}^3 \\ \vdots \end{array} \right] \cdot \underline{\bar{V}} \\ &\equiv \underline{c}^F \cdot \underline{\bar{V}} + u^{\alpha+1} \times \underline{U} \cdot \underline{\bar{B}} \cdot \underline{\bar{V}}, \end{aligned} \quad (2.47)$$

where $c^F(v)$ is the arbitrary function of partial integration, and $\underline{c}^F \cdot \underline{\bar{V}}$ is its Taylor expansion, so that the convolution constant \underline{c}^F corresponds to the integration constant.

As in Section 2.3, if $\alpha = m$ is a negative integer, the integration of the $(m - 1)^{\text{th}}$ row becomes

$$\int u^{-m} u^{m-1} \underline{a}^{m-1} \cdot \underline{\bar{V}} du = \log u \underline{a}^{m-1} \cdot \underline{\bar{V}}, \quad (2.48)$$

and the integration of equation (2.47) is written

$$\int \underline{U} \cdot \underline{\bar{A}} \cdot \underline{\bar{V}} du = \underline{c}^F \cdot \underline{\bar{V}} + \log u \underline{a}^{m-1} \cdot \underline{\bar{V}} + \underline{U} \cdot \underline{\bar{B}} \cdot \underline{\bar{V}}, \quad (2.49)$$

where the $(m - 1)^{\text{th}}$ row of $\underline{\bar{B}}$ is $\underline{0}$.

3. ELLIPTIC INTEGRALS

The evaluation of real elliptic integrals of a real variable is given in this section. Complex elliptic integrals can be evaluated as cases of the Schwarz-Christoffel transformation.

3.1. Elliptic Integral of the First Kind

The elliptic integral of the first kind in Jacobi's normal form is, in the notation of [21],

$$F = \int_0^t \frac{d\tau}{\sqrt{1-\tau^2}\sqrt{1-k^2\tau^2}}. \quad (3.1)$$

The integrand is a function given in factors

$$g(t) = (1-t)^{-1/2}(1+t)^{-1/2}(1-kt)^{-1/2}(1+kt)^{-1/2} \quad (3.2)$$

$$\equiv g_1(t)g_2(t)g_3(t)g_4(t). \quad (3.3)$$

The integrand will be expanded as series using convolution algebra on the sequences of coefficients, called convolution numbers [20].

The singularities of the function $g(t)$ are those of g_1 at 1, of g_2 at -1 , of g_3 at $1/k$, and of g_4 at $-1/k$. If k is small enough, the whole range $0 \leq t \leq 1$ of the function can be covered by one Frobenius series about $t = 1/k$ as shown in Figure 3.1a for $k = .35$. The numerical radius of convergence is either bounded by the singularity at -1 or the singularity at $1/k$. This condition remains valid for values of k until the numerical Frobenius disk touches the origin, when

$$0.7 \left(\frac{1}{k} - 1 \right) = 1 \quad (3.4)$$

which gives the solution $k = 0.411\dots$, therefore we take

$$k = 0.4 \quad (3.5)$$

as practical limit.

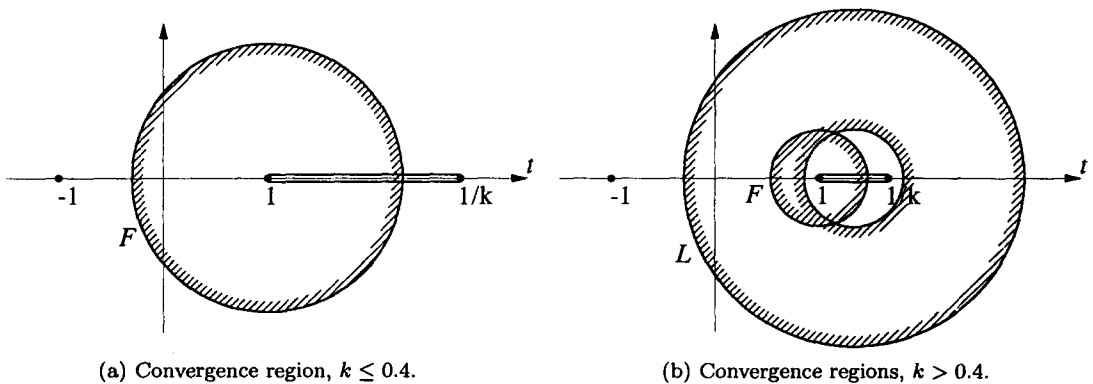


Figure 3.1. Convergence regions for elliptic integral of the first kind.

As soon as $k > 0.411\dots$, the Frobenius disk does not reach the origin any more. The numerical radius of convergence of the Frobenius series, which we will call Frobenius radius in this context and denote by r_F , is restricted by the singularities at 1 and $1/k$ such that

$$r_F = 0.7 \min \left(1, \frac{1}{k} - 1 \right). \quad (3.6)$$

An additional series must be used to fill the gap between $t = 0$ and $t = 1 - r_F$. The first choice seems to be a Taylor series with a disk covering the gap. However as $k \rightarrow 1$, we find that the

Frobenius disk becomes so small that the Taylor disk cannot reach it, and more and more smaller Taylor disks would have to be used to fill the smaller and smaller gaps, remembering that we can only utilize 0.7 of the theoretical radius of convergence. On the other hand, the Frobenius series about the point $t = 1$ must be retained because it is the only one that covers the region near and including that point.

Another possible choice is then a Laurent series, conveniently about the center of the singularities at 1 and $1/k$, i.e., about a point

$$t_0 = \frac{1 + 1/k}{2}. \tag{3.7}$$

The outer radius r_o of the numerical annulus of convergence of the Laurent series, limited by the singularity at $t = -1$, is given by

$$r_o = 0.7(1 + t_0). \tag{3.8}$$

This covers the origin when $k > (1 - 0.7)/(3 \cdot 0.7 - 1) = 0.272\dots$, which is well below the value of $0.411\dots$ as limit of the single Frobenius series. The inner radius is given according to equation (2.36) by

$$r_i = \frac{(1/k - 1)/2}{0.7}. \tag{3.9}$$

It can be shown that the thickness of the annulus, according to equation (2.36), is greater than zero for the value of $k > 0.272\dots$, and that the Frobenius disk around $t = 1$ always overlaps with the annulus of the Laurent series. Therefore for the whole range of $k > 0.4$, the arrangement of one Frobenius series and one Laurent series covers the range of $0 \leq t \leq 1$, as shown in Figure 3.1b for $k = 0.6$.

FROBENIUS SERIES. Each function is expanded about $t = 1$ for all values of k . The Frobenius radius shrinks to 0 as $k \rightarrow 1$, with the result that a series in $t - 1$ will produce highly divergent sequences, even though the series converge, which the convolution algebra cannot handle. Therefore the Frobenius expansion is done with a variable scaled proportional to the Frobenius radius,

$$u = \frac{(t - 1)}{r_F}. \tag{3.10}$$

We define now new functions

$$g_1(u) = (-u)^{-1/2}, \tag{3.11}$$

$$a_2(u) = 2 + r_F u = \underline{U} \cdot \bar{a}_2, \tag{3.12}$$

$$a_3(u) = (1 - k) - k r_F u = \underline{U} \cdot \bar{a}_3, \tag{3.13}$$

$$a_4(u) = (1 + k) + k r_F u = \underline{U} \cdot \bar{a}_4. \tag{3.14}$$

The expansion of $g(t)$ is then obtained as a function of u by the product

$$g_F(u) = (-u)^{-1/2} \times \underline{U} \cdot \bar{g} \times r_F^{-1/2}, \tag{3.15}$$

where \bar{g} is obtained by convolution number algebra of multiplication, square root, and inversion [20],

$$\bar{g} = \frac{\bar{\delta}_0}{\sqrt{\bar{a}_2 * \bar{a}_3 * \bar{a}_4}}. \tag{3.16}$$

In equation (3.15), we have denoted the Frobenius series by $g_F(u)$, and $g(u) = \underline{U} \cdot \bar{g}$ as the regular Taylor series factor.

The real Frobenius series is of the form

$$g_F(u) = (-u)^\alpha (g_0 + g_1 u + g_2 u^2 + \dots), \quad (3.17)$$

which is slightly different from the form in equation (2.22), and for real negative values of u is rather determined separately. The integral with respect to u is

$$\begin{aligned} f_F(u) &= f_{F0} + (-u)^{\alpha+1} \left(\frac{-g_0}{\alpha+1} + \frac{-g_1}{\alpha+2} u + \frac{-g_2}{\alpha+3} u^2 + \dots \right) \\ &\equiv f_{F0} + (-u)^{\alpha+1} (f_0 + f_1 u + f_2 u^2 + \dots) \\ &= f_{F0} + (-u)^{\alpha+1} \underline{U} \cdot \bar{f}, \end{aligned} \quad (3.18)$$

where $f(u)$ is the Taylor series factor.

Therefore a Frobenius integration routine is programmed for the coefficients

$$f_i = \frac{-g_i}{(\alpha + i + 1)}, \quad \text{for } i = 0, \dots, n. \quad (3.19)$$

The real elliptic integral of the first kind is therefore given by the Frobenius series in terms of $u = (t - 1)/r_F$,

$$\int g(t) dt = r_F \int g_F(u) du = f_F(u) = f_{F0} + (-u r_F)^{1/2} \times \underline{U} \cdot \bar{f}. \quad (3.20)$$

To determine the constant in equation (3.20), the known part is evaluated at the lower boundary, which in the case of $k \leq 0.4$ is $t = 0$, $u = -1/r_F$, where the integral is zero, i.e.,

$$f_{F0} = -\underline{U} \left(u = -\frac{1}{r_F} \right) \cdot \bar{f}, \quad k \leq 0.4. \quad (3.21)$$

The actual evaluation of the series, which is implied by the dot-product, is always implemented by using the well-conditioned nested sequence, also used in [27]. The constant f_{F0} is identical to the complete elliptic integral of the first kind, $K(k)$.

LAURENT SERIES $k > 0.4$. Each factor in equation (3.2) is expanded about $t = t_0$; with the transformation

$$v = t - t_0, \quad (3.22)$$

the functions g_1 and g_3 are expanded as Frobenius-Laurent series in v , and with the further transformation

$$s = \frac{1}{v}, \quad (3.23)$$

the half-Laurent series can be treated as a Taylor series with convolution algebra. Defining the functions

$$a_1(s) = 1 + \frac{t_0 - 1}{v} = 1 + (t_0 - 1)s = \underline{S} \cdot \bar{a}_1, \quad (3.24)$$

$$a_3(s) = k + \frac{kt_0 - 1}{v} = k + (kt_0 - 1)s = \underline{S} \cdot \bar{a}_3, \quad (3.25)$$

the product is obtained as

$$\begin{aligned} g_1 g_3 &= \frac{(-v)^{-1/2} (-v)^{-1/2}}{\sqrt{a_1(s) a_3(s)}} \\ &= -\frac{s}{\sqrt{a_1(s) a_3(s)}} \\ &\equiv \underline{S} \cdot \bar{g}_{a_1} = g_{a_1}(s), \end{aligned} \quad (3.26)$$

where \bar{g}_{a1} is obtained by convolution number algebra [20],

$$\bar{g}_{a1} = -\frac{\bar{\delta}_1}{\sqrt{\bar{a}_1 * \bar{a}_3}}. \quad (3.27)$$

The function $g_{a1}(s)$ was developed as the product of two Frobenius series and just happens by chance to be a half-Laurent series; the method itself does not depend on this special case.

Once \bar{g}_{a1} is determined, the function $g_{a1}(v)$ is formally written as half-Laurent series

$$g_{a1}(v) = \underline{V} \cdot \tilde{g}_{a1}. \quad (3.28)$$

The functions g_2 and g_4 are expanded as Frobenius-Taylor series in v , with

$$a_2(v) = (1 + t_0) + v = \underline{V} \cdot \bar{a}_2, \quad (3.29)$$

$$a_4(v) = (1 + kt_0) + kv = \underline{V} \cdot \bar{a}_4, \quad (3.30)$$

and the product becomes

$$\begin{aligned} g_2 g_4 &= \frac{1}{\sqrt{a_2(v) a_4(v)}} \\ &\equiv \underline{V} \cdot \bar{g}_{a2} = g_{a2}(v), \end{aligned} \quad (3.31)$$

where again by convolution number algebra

$$\bar{g}_{a2} = \frac{\bar{\delta}_0}{\sqrt{\bar{a}_2 * \bar{a}_4}}. \quad (3.32)$$

The expansion of $g(t)$ is now obtained as a function of v by the product

$$g_L(v) = \underline{V} \cdot \tilde{g}_{a1} \times \underline{V} \cdot \bar{g}_{a2} \quad (3.33)$$

$$= \underline{V} \cdot \tilde{g}_{b1} + \underline{V} \cdot \bar{g}_{b2} \quad (3.34)$$

with the procedure implied by equation (2.13), expressed as in equation (2.14) as

$$\tilde{g}_{a1} * \bar{g}_{a2} \Rightarrow \tilde{g}_{b1}, \bar{g}_{b2}. \quad (3.35)$$

The function $g_L(v)$ is integrated by integrating the half-Laurent and Taylor series separately,

$$\begin{aligned} \int g_L(v) dv &= \int g_{b1}(v) dv + \int g_{b2}(v) dv \\ &= f_L(v) = g_{b11} \log(-v) + \underline{V} \cdot \tilde{f}_{b1} + \underline{V} \cdot \bar{f}_{b2}, \end{aligned} \quad (3.36)$$

where g_{b11} is the 1-element in the Laurent number \tilde{g}_{b1} . The convolution numbers of the integrals are determined by the method in Section 2.1 and [20]

$$\tilde{f}_{b1} = \int \tilde{g}_{b1}, \quad (3.37)$$

$$\bar{f}_{ib2} = \int \bar{g}_{b2}. \quad (3.38)$$

The subscript $ib2$ indicates that the constant f_{b20} is not determined yet and taken as 0. This constant is determined by evaluation of the known part at the lower boundary, $t = 0$, $v = -t_0$, where the integral is zero, therefore

$$f_{b20} = -\left(g_{b11} \log(t_0) + \underline{V}(v = -t_0) \cdot \tilde{f}_{b1} + \underline{V}(v = -t_0) \cdot \bar{f}_{ib2}\right) \quad (3.39)$$

and introduced into the position 0 of the convolution number \overline{f}_{ib2} , which is then the complete convolution number \overline{f}_{b2} in equation (3.36).

FROBENIUS SERIES $k > 0.4$. The constant f_{F0} in equation (3.18) is now determined differently, viz. by the overlapping region of the Frobenius and Laurent series. The middle of the overlapping region is

$$t_m = \frac{(t_0 - r_i + 1 - r_F)}{2}, \quad u_m = 1 - t_m, \quad v_m = t_0 - t_m, \quad (3.40)$$

and the Laurent series and Frobenius series are evaluated here to determine the constant

$$f_m = g_{b11} \log(-v_m) + \underline{V}(v = v_m) \cdot \tilde{f}_{b1} + \underline{V}(v = v_m) \cdot \overline{f}_{b2}, \quad (3.41)$$

$$f_{F0} = f_m - (-u_m r_F)^{1/2} \times \underline{U}(u = u_m) \cdot \overline{f}. \quad (3.42)$$

The value of the elliptic integral of the first kind for values $k \leq 0.4$ is now computed according to the value of the upper boundary t , by equation (3.20). For values $k > 0.4$, it is computed according to the value of the upper boundary t , for $t < t_m$, by equation (3.20), and for $t > t_m$, by equation (3.36).

RESULTS. The equations above have been used to program a subroutine on a personal computer in standard (single) precision, using QuickBASIC³. For various values of k in the range $0 < k \leq 1$ and a range of values of t in the range $0 \leq t \leq 1$, the results coincide with the values given in [21,22] within all the available digits for $n = 40$, while for $n = 30$ only the last digit may differ in some range. The only value that the subroutine cannot compute is $F(t = 1, k = 1)$.

The reason that shorter convolution numbers can be used is due to the fact that regions overlap and the numerical radius is actually never reached.

3.2. Elliptic Integral of the Second Kind

The elliptic integral of the second kind in Jacobi's normal form is [21]

$$F = \int_0^t \sqrt{\frac{1 - k^2 \tau^2}{1 - \tau^2}} d\tau. \quad (3.43)$$

The integrand is a function given in factors

$$g(t) = (1 - t)^{-1/2} (1 + t)^{-1/2} (1 - kt)^{1/2} (1 + kt)^{1/2} \quad (3.44)$$

$$\equiv g_1(t) g_2(t) g_3(t) g_4(t). \quad (3.45)$$

The binomial factors are the same as for the elliptic integral of the first kind, and therefore the singularities, and consequent division of the range into regions according to the value of k , are the same as shown in Figures 3.2a and 3.2b.

FROBENIUS SERIES. The transformation of equation (3.10) is applied, and the functions $g_1(u)$, $a_2(u)$, $a_3(u)$, and $a_4(u)$ are defined as in equations (3.11)–(3.14). The expansion of $g(t)$ becomes, as in equation (3.15),

$$g_F(u) = (-u)^{-1/2} \times \underline{U} \cdot \overline{g} \times r_F^{-1/2}, \quad (3.46)$$

where \overline{g} is now obtained by convolution number algebra

$$\overline{g} = \sqrt{\frac{\overline{a_4}}{a_3 * \frac{\overline{a_4}}{a_2}}}. \quad (3.47)$$

³QuickBASIC is a registered trademark of Microsoft Corporation.

The Frobenius series of equation (3.46) is integrated according to equations (3.18) and (3.19), and the same form as equation (3.20) is obtained. For $k \leq 0$, the constant f_{F0} is determined as in equation (3.21), which is now identical to the complete elliptic integral of the second kind, $E(k)$.

LAURENT SERIES $k > 0.4$. For the range $k > 0.4$, the series are developed as for the elliptic integral of the first kind, with the the transformations according to equations (3.22) and (3.23), and the same definitions of the functions $a_1(s)$ and $a_3(s)$ as in equations (3.24) and (3.25). The product for the half-Laurent series factor is now obtained as

$$\begin{aligned} g_1 g_3 &= \frac{(-v)^{-1/2} \sqrt{a_3(s)}}{(-v)^{-1/2} \sqrt{a_1(s)}} \\ &= \sqrt{\frac{a_3(s)}{a_1(s)}} \\ &\equiv \underline{S} \cdot \overline{g}_{a_1} = g_{a_1}(s), \end{aligned} \tag{3.48}$$

where \overline{g}_{a_1} is obtained by convolution number algebra

$$\overline{g}_{a_1} = \sqrt{\frac{\overline{a_3}}{a_1}} \tag{3.49}$$

with which the half-Laurent series is expressed as in equation (3.28).

The Taylor series factor consists now of the same functions $a_2(v)$ and $a_4(v)$ of equations (3.29) and (3.30), but with the product

$$\begin{aligned} g_2 g_4 &= \sqrt{\frac{a_4(v)}{a_2(v)}} \\ &\equiv \underline{V} \cdot \overline{g}_{a_2} = g_{a_2}(v), \end{aligned} \tag{3.50}$$

where again by convolution number algebra

$$\overline{g}_{a_2} = \sqrt{\frac{\overline{a_4}}{a_2}}. \tag{3.51}$$

From here onwards, the equations for the Laurent series of the elliptic integral of the second kind, and the determination of the constant f_{b20} , are exactly the same as equations (3.33)–(3.39) for the elliptic integral of the first kind.

FROBENIUS SERIES $k > 0.4$. The matching with the Laurent series to obtain the constant f_{F0} is exactly the same as equations (3.40)–(3.42) for the elliptic integral of the first kind.

RESULTS. The elliptic integral of the second kind has been programmed with the equations above, and numerical tests revealed the same quality of results as for the elliptic integral of the first kind mentioned earlier.

3.3. Elliptic Integral of the Third Kind

The elliptic integral of the third kind in Jacobi's normal form is [21]

$$\Pi = \int_0^t \frac{d\tau}{(1 - \alpha^2 \tau^2) \sqrt{1 - \tau^2} \sqrt{1 - k^2 \tau^2}}, \quad 0 \leq k \leq 1, \quad -\infty < \alpha^2 < \infty. \tag{3.52}$$

The different regions of convergence into which the range $0 \leq t \leq 1$ can be partitioned depend on both parameters k and α^2 . To construct a general routine for all k and α^2 in equation (3.52),

the region of applicability of different possible combinations of convergence regions can be put into a k, α^2 -plane until it is completely covered.

The scope of this paper does not include this topological problem. Instead we show how the series can be developed for a specific value of α^2 , and for which regions in the k, α^2 -plane it will then be applicable.

As an example, we choose $\alpha^2 \leq 0$, so that the singularities of the term $(1 - \alpha^2 t^2)$ lie in the complex plane at $\pm \hat{i} 1/|\alpha|$. These are called circular cases [21].

We write the integrand in factors

$$g(t) = (1-t)^{-1/2}(1+t)^{-1/2}(1-kt)^{-1/2}(1+kt)^{-1/2}(1-\alpha^2 t^2)^{-1} \quad (3.53)$$

$$\equiv g_1(t) g_2(t) g_3(t) g_4(t) g_5(t). \quad (3.54)$$

Let

$$a = \frac{1}{\sqrt{-\alpha^2}}, \quad (3.55)$$

then the singularities of g_5 lie at $\pm \hat{i} a$ on the imaginary axis. The regions of convergence that were chosen for the integrals $F(t, k)$ and $E(t, k)$, Figures 3.1a and 3.1b, do not reach the origin any more if $\hat{i} a$ lies too close to the axis. The regions chosen for such a case are shown in Figure 3.2a for smaller k and in Figure 3.2b for larger k , the actual limits to be determined later. The same Frobenius and Laurent series are used as before, their radius of convergence now being limited by the singularity at $t = \hat{i} a$. A Taylor series is chosen to cover the origin at the center of the gap between the origin and the Frobenius or Laurent disk. Such an arrangement is possible as long as a is not too small, i.e., $-\alpha^2$ is not too large. Figure 3 is drawn for $a = 0.5$, $\alpha^2 = -4$, while $k = 0.35$ in Figure 3.2a and $k = 0.65$ in Figure 3.2b.

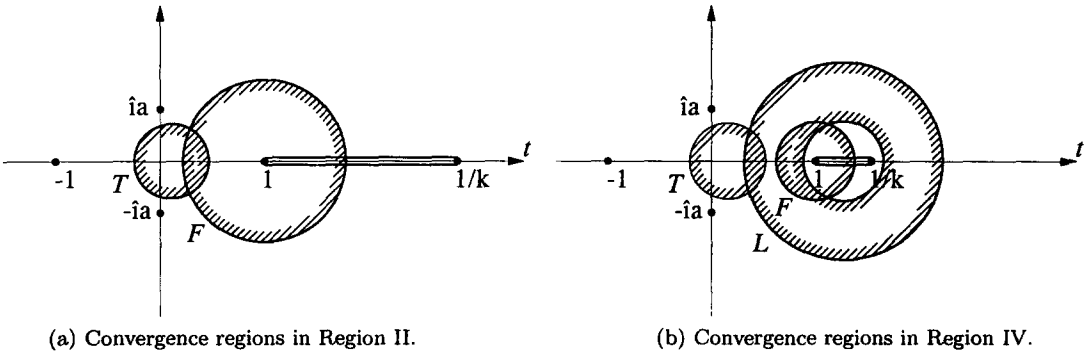


Figure 3.2. Convergence regions for elliptic integral of the third kind.

Let the Frobenius numerical radius of convergence be r_F , which leaves a gap h from to the origin,

$$r_F = 0.7 \min \left(\sqrt{1+a^2}, \frac{1}{k} - 1, 1 \right), \quad (3.56)$$

$$h = 1 - r_F. \quad (3.57)$$

The three limits of the Frobenius disk are used as a safety precaution, so that the routine can be used for all values of k and a .

If the gap is negative, for larger values of a , then for $k \leq 0.4$ only the Frobenius series is required, as in Figure 3.1a, which we will call parameter Region I in the k, α^2 -plane.

If the gap is positive, we place the Taylor disk at the middle of the gap at

$$t_1 = \frac{h}{2} \quad (3.58)$$

as shown in Figure 3.2a, which we call parameter Region II in the k, α^2 -plane. The Taylor numerical radius of convergence may be limited by either $t = \hat{t}a$ or $t = 1$, therefore we take

$$r_T = 0.7 \min \left(\sqrt{t_1^2 + a^2}, 1 - t_1 \right). \quad (3.59)$$

When the Taylor disk cannot reach the Frobenius disk any more, we will use the arrangement of the Laurent disk and Frobenius disk again, as in Figure 3.1b, and we call this parameter Region III in the k, α^2 -plane. But if a is too small, there is a gap left between the Laurent disk and the origin, in which case we will use again a Taylor series to fill the gap. Let the Laurent numerical outer radius of convergence be r_o , the center at t_0 from equation (3.7), which leaves a gap h to the origin, therefore

$$r_o = 0.7 \min \left(\sqrt{t_0 + a^2}, 1 + t_0 \right), \quad (3.60)$$

$$h = t_0 - r_o, \quad (3.61)$$

and place the Taylor disk at the middle of the gap at $t = t_1$ according to equation (3.58). This arrangement is shown in Figure 3.2b, and we call it parameter Region IV in the k, α^2 -plane.

TAYLOR SERIES. The Taylor radius r_T can become quite small, and to prevent too large numbers in the convolution number, a scaled transformation similar to equation (3.10) is used:

$$w = \frac{(t - t_1)}{r_T}. \quad (3.62)$$

We define the functions

$$a_1(w) = (1 - t_1) - r_T w = \underline{W} \cdot \bar{a}_1, \quad (3.63)$$

$$a_2(w) = (1 + t_1) + r_T w = \underline{W} \cdot \bar{a}_2, \quad (3.64)$$

$$a_3(w) = (1 - kt_1) - k r_T w = \underline{W} \cdot \bar{a}_3, \quad (3.65)$$

$$a_4(w) = (1 + kt_1) + k r_T w = \underline{W} \cdot \bar{a}_4, \quad (3.66)$$

$$a_5(w) = 1 - \alpha^2(w + t_1)^2 = (1 - \alpha^2 t_1^2) - 2\alpha^2 t_1 r_T w - \alpha^2 r_T^2 w^2 = \underline{W} \cdot \bar{a}_5. \quad (3.67)$$

The last function was not written in terms of binomial factors to avoid complex numbers.

The expansion of $g(t)$ is a Taylor series of w

$$g(w) = \underline{W} \cdot \bar{g}, \quad (3.68)$$

where \bar{g} is obtained by convolution algebra

$$\bar{g} = \frac{\bar{\delta}_0}{\left(\bar{a}_5 * \sqrt{\bar{a}_1 * \bar{a}_2 * \bar{a}_3 * \bar{a}_4} \right)}. \quad (3.69)$$

Integration produces the expansion

$$\int g(w) dt = r_T \times \int g(w) dw = r_T \times f_T(w) = r_T \times \underline{W} \cdot \bar{f}_T, \quad (3.70)$$

where \bar{f}_T is the convolution number corresponding to integration, first with zero constant, in the notation of [20],

$$\bar{f}_i = \int \bar{g}. \quad (3.71)$$

Afterwards the factor r_T can be included in \bar{f}_T . The constant f_{T0} in \bar{f}_T is determined by the value zero at $t = 0$, $w = -t_1/r_T$, by using the incomplete convolution number \bar{f}_i with zero leading element,

$$f_{T0} = -\underline{W}\left(w = -\frac{t_1}{r_T}\right) \cdot \bar{f}_i, \quad (3.72)$$

which is then entered into \bar{f}_i to complete the convolution number \bar{f}_T . The center of the overlapping region of Taylor and Frobenius disk in Region II, or of Taylor disk and Laurent disk in Region IV, is

$$t_m = \frac{(h + t_1 + r_T)}{2}, \quad (3.73)$$

where h is determined from equation (3.57) for Region II and from equation (3.61) in Region IV, and the Taylor series is used for $t \leq t_m$ only.

LAURENT SERIES. The Laurent series is developed with the transformations of equations (3.22) and (3.23), and the half-Laurent series factor by the equations (3.24)–(3.28), resulting in the Laurent number \tilde{g}_{a1} .

The Frobenius-Taylor series factor is obtained starting with the same factors as for the first kind in equations (3.29) and (3.30), but now the additional factor for the third kind is included by defining the function

$$a_5(v) = (1 - \alpha^2 t_0^2) - 2\alpha^2 t_0 v - \alpha^2 v^2 = \underline{V} \cdot \bar{a}_5, \quad (3.74)$$

and the product is

$$\begin{aligned} g_2 g_4 g_5 &= \frac{1}{\left(a_5(v) \sqrt{a_2(v) a_4(v)}\right)} \\ &\equiv \underline{V} \cdot \bar{g}_{a2} = g_{a2}(v), \end{aligned} \quad (3.75)$$

where \bar{g}_{a2} is obtained by convolution number algebra

$$\bar{g}_{a2} = \frac{\bar{\delta}_0}{\left(\bar{a}_5 * \sqrt{\bar{a}_2 * \bar{a}_4}\right)}. \quad (3.76)$$

The product, separation into half-Laurent and Taylor series, and integration follows from equations (3.33)–(3.38).

In Region III, the constant f_{b20} is determined by the matching at the origin by equation (3.39).

In Region IV, the constant f_{b20} is determined by the matching at the middle of the overlapping of Taylor and Laurent series, at t_{m1} determined by

$$t_{m1} = \frac{(t_1 + r_T + t_0 - r_o)}{2}. \quad (3.77)$$

With $w_{m1} = (t_{m1} - t_1)/r_T$,

$$f_{m1} = \underline{W}(w = w_{m1}) \cdot \bar{f}_T, \quad (3.78)$$

and the equation (3.39) is modified to

$$f_{b20} = f_{m1} - \left(g_{b11} \log(t_0) + \underline{V}(v = -t_0) \cdot \tilde{f}_{b1} + \underline{V}(v = -t_0) \cdot \bar{f}_{ib2}\right). \quad (3.79)$$

The result is as equation (3.36), reproduced here,

$$f_L(v) = g_{b11} \log(-v) + \underline{V} \cdot \tilde{f}_{b1} + \underline{V} \cdot \bar{f}_{b2}. \quad (3.80)$$

The Laurent series is used for t from t_{m1} up to t_{m2} , where it overlaps the Frobenius disk,

$$t_{m2} = \frac{(t_0 - r_i + 1 - r_F)}{2}, \quad (3.81)$$

where the inner numerical radius of the Laurent series is r_i from equation (3.9), and the Frobenius numerical radius is r_F from equation (3.56).

FROBENIUS SERIES. For the remaining range of $t_{m2} < t \leq 1$, the Frobenius series is developed again starting within equations (3.10)–(3.14), and then defining the additional factor, similar to equation (3.67),

$$a_5(u) = (1 - \alpha^2) - 2\alpha^2 r_F u - \alpha^2 r_F^2 u^2 = \underline{U} \cdot \bar{a}_5. \quad (3.82)$$

The expansion of $g(t)$ is the Frobenius series as in equation (3.15), where \bar{g} is now obtained by convolution algebra similar to equation (3.16),

$$\bar{g} = \frac{\bar{\delta}_0}{\left(\bar{a}_5 * \sqrt{\bar{a}_2 * \bar{a}_3 * \bar{a}_4} \right)}. \quad (3.83)$$

Integration of the Frobenius series follows the method of equation (3.20), but the constant f_{F0} is now determined at the matching point depending on the parameter region. In Region I, the matching point is the origin, the constant determined by equation (3.21). In Region II, the matching point is in the Taylor disk at $t = t_m$ by equation (3.73), where f_m is obtained from the Taylor series of equation (3.70), with $w_m = (t_m - t1)/r_T$,

$$f_m = \underline{W}(w = w_m) \cdot \bar{f}_T. \quad (3.84)$$

The Frobenius series is then as equation (3.20), reproduced here for reference,

$$f_F(u) = f_{F0} + (-u r_F)^{1/2} \times \underline{U} \cdot \bar{f}. \quad (3.85)$$

In Region I, $f_{F0} = \Pi(\alpha^2, k)$. The elliptic integral for Region II is given by the Taylor series equation (3.70) for $0 \leq t_m$, and by the Frobenius series equation (3.85) for $t_m < t \leq 1$.

In Region IV, the constant f_{F0} is determined by the matching of Laurent and Frobenius series, according to equations (3.41),(3.42), where for the second matching point t_{m2} in this Region IV

$$u_m = 1 - t_{m2}, \quad v_m = t_0 - t_{m2}. \quad (3.86)$$

The elliptic integral for Region IV is given by the Taylor series equation (3.70) for $0 \leq t_{m1}$, by the Laurent series equation (3.80) for $t_{m1} < t \leq t_{m2}$, and by the Frobenius series equation (3.85) for $t_{m2} < t \leq 1$.

REGIONS IN THE k, α^2 -PLANE. The convergence regions in the t -plane are also valid for certain positive values of α^2 , which cause singularities on the real axis at $t = \pm 1/\alpha$, in which case let

$$c = \frac{1}{\alpha}. \quad (3.87)$$

The parameter Regions I to IV as restricted by either \hat{a} or c are shown in Figure 3.3.

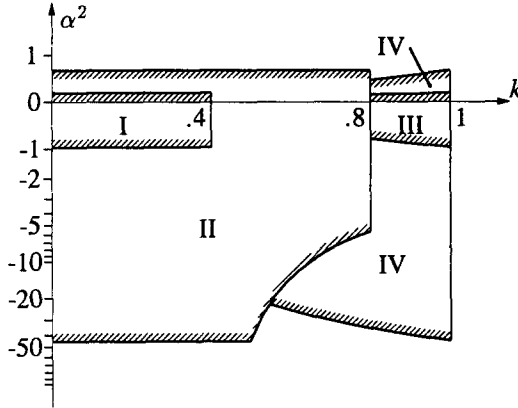


Figure 3.3. Regions in the k, α^2 -plane for elliptic integral of the third kind.⁴

Region I, for $k \leq 0.4$, is valid as long as the Frobenius disk still reaches the origin, which can be shown to be for

$$-0.961 < \alpha^2 < 0.170. \quad (3.88)$$

Region II is bounded by k by the condition that the Taylor disk can still fill the gap between origin and Frobenius disk, which leads to

$$k < 0.799. \quad (3.89)$$

For smaller k , the singularity can be due to real c , which is the upper bound of Region II at

$$\alpha^2 < 0.638. \quad (3.90)$$

If the singularity lies at \hat{a} , the condition that for each $k < 0.799$ the Taylor disk can still fill the gap leads to

$$\frac{3.843}{(1 + 1/k)^2} < \alpha^2, \quad (3.91)$$

which is the lower curved boundary of Region II. But this condition is again limited by the smallest Taylor disk that can still reach the origin from its center t_1 , which occurs at

$$-44.992 < \alpha^2, \quad (3.92)$$

which is the lower straight boundary of Region II.

For $k > 0.799$, the Region III is bounded by the condition that either \hat{a} or c are large enough so that the Laurent disk can reach the origin, which leads to

$$-\frac{0.678}{(1 + 1/k)^2} < \alpha^2 < \frac{3.843}{(1 + 1/k)^2}, \quad (3.93)$$

which are the two curved boundaries of Region III.

For $k > 0.799$, the Region IV is bounded by the condition that the smallest Laurent disk is possible if the gap can be filled by the Taylor disk. On the lower boundary, the Taylor disk is restricted by \hat{a} . On the upper boundary, the Laurent disk is restricted by c , resulting in the condition

$$\alpha^2 < \frac{1}{(1.214(1 + 1/k) - 1.176)^2}, \quad (3.94)$$

⁴The vertical scale is drawn on a 'double logarithmic' scale $y = \log(x + \sqrt{x^2 + 1})$, which is linear at 0 and logarithmic at both far ends.

which is the upper curved boundary of Region IV. It intersects the vertical boundary of Region II at $\alpha^2 = 0.412$, and reaches $\alpha^2 = 0.638$ at $k = 1$. On the lower boundary, the Taylor disk is restricted by $\hat{t}a$, resulting in the condition

$$-\frac{179.968}{(1 + 1/k)^2} < \alpha^2, \tag{3.95}$$

which is the lower curved boundary of Region IV. It intersects the curved boundary of Region II at $k = 0.545$, $\alpha^2 = -22.369$, and reaches $\alpha^2 = -44.992$ at $k = 1$.

Figure 3.3 shows the total region in the k, α^2 -plane for which the elliptic integral of the third kind can be computed by the expansions of this Section 3.3.

RESULTS. The elliptic integral of the third kind has been programmed with the equations above. For comparison we have used the values for $\alpha^2 = 0.1$ and 0.5 in [27] (there called γ^2). For $n = 20$, the first six decimal places agreed, except at $\theta = 88^\circ$, $\phi = 90^\circ$ (their notation), but that is not a convergence problem. It is due to the single precision of the converted value to t (in our notation). The derivative $\frac{d}{dt}\Pi(\theta = 88^\circ, \gamma^2 = 0.1, \phi = 90^\circ) = 912$ and $\frac{d}{dt}\Pi(\theta = 88^\circ, \gamma^2 = 0.5, \phi = 90^\circ) = 1640$, which means that an error in the absent digit in t causes an error of the last two digits in the value of Π .

In double precision, all values coincide, except sometimes not the last digit, when $n = 50$, where all values had converged to 13 digits. However, we found a discrepancy in the last four digits in the two cases listed in Table 3.1 below, in the notation of [27].

Table 3.1. Comparison of values of $\Pi(\gamma^2, \theta, \phi)$.

γ^2	θ°	ϕ°	L & M Value	Our Value	Region
0.1	90	1	1.655894132724	1.655894134445	I
0.5	90	1	2.221639684918	2.221639682703	II

If need be, values of the integral can be computed a little outside the convergence regions with increased n . As example, the parameters $\alpha^2 = 0.5$, $k = 0.8$ lie above Region IV, but the Laurent disk is then still only .771 of the theoretical radius. When $n > 100$, the Laurent variable must also be scaled to prevent overflow in the convolution algebra routines.

The two different parameters in the elliptic integral of the third kind require generally much planning of the convergence regions. That is done in the general solution of the Schwarz-Christoffel transformation, which can then be used to solve the elliptic integral with any parameters; see Sections 5.5 and 8.2.

3.4. Concluding Remarks

The three incomplete elliptic integrals can now be evaluated by using the equations for the appropriate range of k . As it often happens, the functions have to be computed for a set of values of t for the same k , therefore a computer subroutine will only compute the convolution numbers that are required for the range of k and t when first required. Also, in a computer program, storage for all the intermediate convolution numbers is not required because many of them can use the same storage. Some may prefer to multiply the simple binomial factors analytically instead of by convolution products, but with correctly programmed convolution products, the saving is negligible. Actual implementation of fixed computer routines for the standard elliptic integrals, that require speed of computation, will not use original series expansions, just like the implementation of sine and cosine functions do not use the original Taylor series.

The complete elliptic integrals can also be evaluated by the same formulas, using $t = 1$. Compared to the well-known expansions of the complete elliptic integrals in k , the computation time may be more. Nevertheless, applications using only complete elliptic integrals should use expansions in k^2 and α^2 .

Compared to the known methods of evaluating elliptic integrals, the advantage of the method by convolution numbers is not necessarily speed of evaluation, but simplicity and the general application to similar integrals. The method does not need a study of all the characteristics of the particular function, on which the classic expansions are based.

If any other integral has a known expression in terms of the three basic integrals, it depends on the complexity of the relation whether a new expansion should be done.

The results using the convolution number technique are in analytical form which is directly accessible to the user. Integrals and higher derivatives can easily be taken. The analytical form is also valid for the complex variable.

The convolution number length n is a variable, therefore it can simply be altered to strike a balance between accuracy and computer time and storage.

Still, in a practical situation it must first be decided whether a much simpler numerical integration is sufficient.

4. THE SCHWARZ-CHRISTOFFEL TRANSFORMATION

4.1. Introduction

The Schwarz-Christoffel transformation (STC) is an integral formula of a function $z = f(s)$ which maps a simple region in the complex s -plane conformally on a simply connected region bounded by a polygon in the complex z -plane. The simple region in the s -plane can be the upper or lower half-plane, or the inside or the outside of a circular disk. The simply connected region bounded by the polygon can be the inside or outside of the polygon.

There are mainly three different approaches in the derivation of the formula, each of which presents, as it were, a different perspective of the transformation. The first is the geometrical approach, followed in [31,32], where use is made of the 2-dimensional vector-like property of the complex variable, or rather its differential. The second approach is a more analytical, followed in [33–35], which starts with the development of a second order differential equation of the reverse function. An even more elaborate treatment is given by von Koppenfels and Stallmann [28], who start with Schwarz's third-order differential equation that maps a polygon of circular arcs on the half-plane or circular disk. The third is a rather unique physical approach by Betz [36], where the turning angles are mapped by a hydrodynamic analogy of sources and sinks. Based on this approach, the mapping equation for the circular arc triangle is also derived in [36].

Various notations exist for the description of the angles of the polygon, some using interior angles [28,31,33–35], others using exterior turning angles [32,36]. The angles are either measured in radians [31,36], or in multiples of π [32–35].

The notation used here is to use radians for turning angles denoted by a_i , but to use exponents denoted by α_i in multiples of π which gives the simplest appearance of the formula. Consistency for the interior and exterior polygon formula is preserved by denoting counterclockwise turning angles positive and clockwise turning angles negative for both interior and exterior polygons. The sides of the polygon are always followed consistently during complex integration with the enclosed region on the left, which is a counterclockwise direction for the interior polygon, and an apparent clockwise direction for the exterior polygon. A particular important variation is the mapping of the periodic polygon, of which one segment is mapped on the complete circular disk in the s -plane.

The Schwarz-Christoffel formula that maps the polygon with n corners in the z -plane, on the inside of the unit circular disk in the s -plane, is

$$z = f(s) = \int_{s_0}^s s^{(1-m)/m} (s - s_{a_1})^{-\alpha_1} (s - s_{a_2})^{-\alpha_2} (s - s_{a_3})^{-\alpha_3} \dots (s - s_{a_n})^{-\alpha_n} ds \quad (4.1)$$

$$\equiv \int_{s_0}^s g(s) ds \quad (4.2)$$

$$\alpha_i = \frac{a_i}{\pi}, \quad \sum \alpha_i = \frac{2}{m}.$$

The angles are not limited by theory, the formula allows for overlapping regions, see [28], which may represent a two-dimensional physical problem in a thin sheet.

The scaling and turning constant is left out in the formulas because it does not have any bearing on the general analysis, i.e., equation (4.1) applies to congruent polygons. Integration constants are introduced in the sections where they are required by applications.

The index m is as follows:

$$m = 1, \quad \text{for interior polygons,} \quad (4.3)$$

$$m = -1, \quad \text{for exterior polygons,} \quad (4.4)$$

$$m > 1, \quad \text{for interior cyclic polygons,} \quad (4.5)$$

$$m < -1, \quad \text{for exterior cyclic polygons,} \quad (4.6)$$

$$m = \infty, \quad \text{for straight periodic polygons.} \quad (4.7)$$

The number of interior polygon periods is m , and the number of exterior polygon periods is $-m$. The formula is also valid for noninteger m , which results in multiple sheets of a Riemann plane in the z -plane, although we are not aware of a practical application for such a case.

One case that has apparently not been derived in the literature is the SCT formula for a straight periodic polygon with infinite number of periods, such that $m = \infty$, of which the derivation is given in Appendix B.

The notation for the formula of equation (4.1) is shown in Figures 4.1a and 4.1b for the interior polygon $m = 1$. The notation for the exterior polygon $m = -1$ is shown in Figures 4.1c and 4.1d, where the SC integral has a singularity at the center of the circle. Figures 4.1e and 4.1f show the notation for the periodic polygon, with a discontinuity of the SC integral in the s -plane.

The corresponding mapping on the outside region of the circular disk in the ζ -plane can be obtained by an additional transformation $s = 1/\zeta$, so that the solution is still expanded in series on the inside of the disk in the s -plane, rather than changing the form of the transformation integral.

The analytical solution of the general mapping problem was considered unsolvable in the past, because it cannot be reduced to an expression involving only the classic known functions. The reason is that generally each SCT represents a new and different analytical function. Therefore, each such analytical solution must be developed from first principles. The differential form is expanded in terms Taylor and Frobenius series, and integrated, which can be done easily on a computer using the convolution number [20] if the parameters α_i and s_{a_i} in the equation are known. The expansion about a single cornerpoint in Frobenius series is given in [28], where the purpose was to assist numerical integration over the singular points.

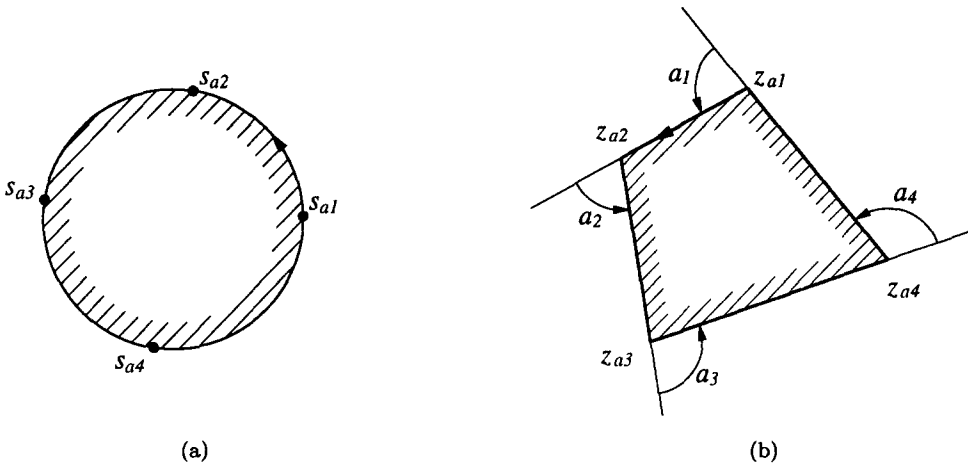
The complete analytical solution consists of a set of series. For this purpose, several convergence disks for the different series have to be chosen to cover the complete unit disk. Such a procedure is then one step in some iteration scheme to determine the parameters s_{a_i} , which is known as the the parameter problem [4,28,37].

The form of equation (4.1) is invariant under Möbius transformation only for the interior polygon, $m = 1$. Forms for other m are introduced in the corresponding application Sections 7, 8, and 9.

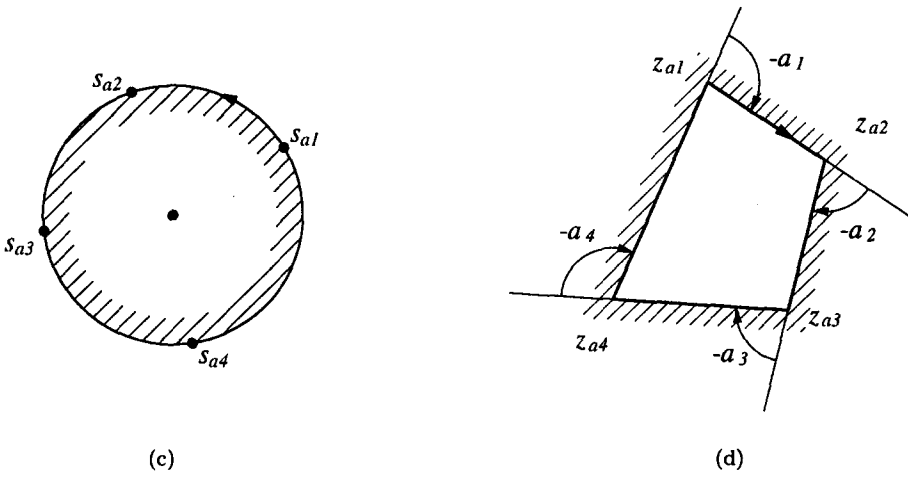
4.2. Outline of the Method

In this and the following sections, the notation n is used for both the number of polygon corners and convolution number length, but the distinction should be clear from the context.

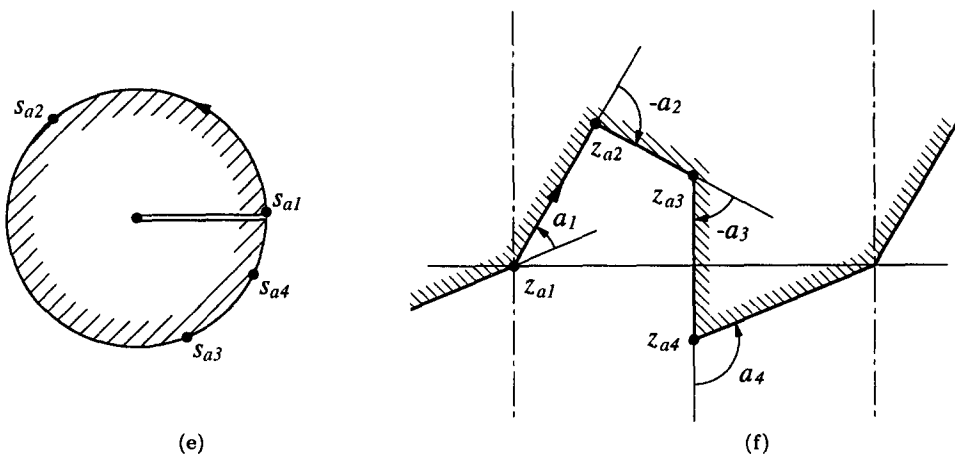
For the theory of analytical expansions, we assume that the corner points $s_{a_1}, s_{a_2}, s_{a_3}, \dots$ are given on the unit circle in the s -plane. The interior of the unit circular disk will be used because



Mapping of the interior polygon.



Mapping of the exterior polygon.



Mapping of the periodic polygon.

Figure 4.1. Notation for the Schwarz-Christoffel formula.

of its finite area. Compared to the half-plane, this may have some disadvantages, but it would be too complicated to cover the half-plane with convergence disks.

Around each cornerpoint in the s -plane, the integrand $g(s)$ in equation (4.2) is expanded in a Frobenius series whose numerical radius of convergence is 0.7 times the distance to the nearest of the two neighboring cornerpoints. The Frobenius series are then integrated. The integration constant is determined later, after a system of overlapping disks is established. The centers and radii of these Frobenius disks are fixed by the singular points s_{ai} . Whether the Frobenius disks overlap or not, there is generally uncovered area left in the interior and including parts of the boundary. A sequence of additional Taylor series is then introduced around suitable points, their numerical radius of convergence determined by the nearest of all surrounding cornerpoints. Starting at a position where a Taylor disk overlaps with any Frobenius disk, theoretically the sequence can be continued until the whole s -disk is covered by these two kinds of overlapping disks.

When some cornerpoints are too close on the circle, a situation which exists readily in the great distortions that occur in conformal mapping, the covering by Taylor disks is inefficient. Therefore, after the Frobenius disks are determined, an additional arrangement of Laurent series may be introduced which contain two or more closely spaced cornerpoint singularities. Their inside and outside numerical radii of convergence are determined, and the Laurent disk is used only if it is efficient by covering a substantial region. The function $g(s)$ is expanded in a Laurent series around the Laurent center, and integrated, without yet the integration constant. Only afterwards are the Taylor disks placed to cover the remaining open regions. Similarly, the function $g(s)$ is expanded in Taylor series in each disk and integrated, also yet without the integration constant.

Any one Frobenius or Taylor disk is taken as reference, the value of the integral $f(s)$ at the center of this disk, s_0 , is taken as 0, which means that the point s_0 is mapped on the point $z = 0$.

The integration constant of all other series is determined by evaluating the Frobenius, Laurent, and Taylor series at a suitable matching point in the overlapping region of two convergence disks. These Frobenius integration constants are the cornerpoints in the z -plane.

The covering with Taylor disks is done in a sequence of two different operations. First, only the boundary, i.e., the circle in the s -plane, is completely covered. This is sufficient if only the mapping of the cornerpoints and boundary of the polygon in the z -plane is required. Afterwards the interior region of the s -disk is covered, if the mapping of the complete polygon region is required.

All expansions are done using the convolution algebra of [20] and Section 2. The result is a set of convolution numbers and integration constants, which is the analytical representation of the function $f(s)$ of equation (4.1), which is denoted as

$$f(s) = S_C \left[\begin{array}{cccc} s_{a1}, & s_{a2}, & s_{a3}, & \cdots s_{an} \\ \alpha_1, & \alpha_2, & \alpha_3, & \cdots \alpha_n \end{array} ; s \right], \tag{4.8}$$

similar to the notation used in [35]. We may then use a position constant \hat{c}_1 and a scaling and rotation constant \hat{c}_2 for a scaled mapping

$$z = \hat{c}_1 + \hat{c}_2 f(s). \tag{4.9}$$

4.3. Internal Polygon

COVERING BY CONVERGENCE DISKS. As an example, consider the circle of Figure 4.2a with six points s_{a1}, \dots, s_{a6} given as shown, each of which is specified by a single real variable, to be mapped on the interior of a 6-sided polygon whose turning angles a_1, \dots, a_6 are specified at the corners z_{a1}, \dots, z_{a6} . The function $\log(s)$, rather than s , is plotted in the circle to show the mapping of the circle on the polygon graphically.

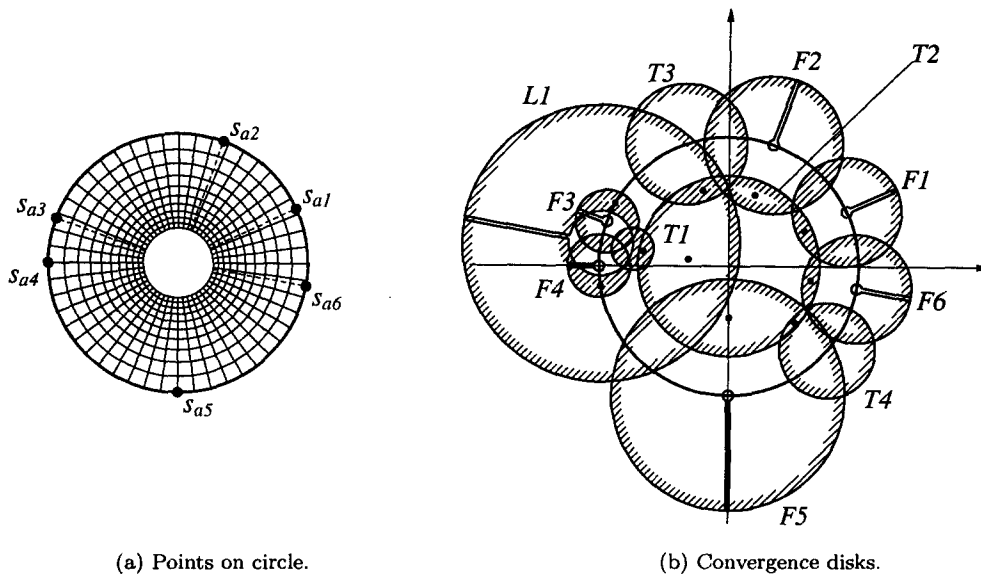


Figure 4.2. Expansions over circle.

The series expansion of the integrand $g(s)$ will consist primarily of six Frobenius-Taylor series centered around s_{a1}, \dots, s_{a6} . Their convergence disks are shown as F_1, \dots, F_6 in Figure 4.2b. Their radii of convergence are determined by the neighboring points according to Section 2.4. The discontinuity branches are chosen radially to the outside. Each Frobenius series is determined independently by the integrand $g(s)$.

An efficient covering is achieved by placing a Laurent disk, marked L_1 , over the two smaller Frobenius disks F_3 and F_4 , with the Laurent center on the circle for simplicity, in the middle between s_{a3} and s_{a4} . There will still be a resulting discontinuity branch, taken radially outwards, so that the expansion in this disk will actually be a Frobenius-Laurent expansion.

There are two gaps left on the boundary, between F_2 and L_1 , and between F_5 and F_6 . These gaps which do not contain any singularities are covered with Taylor disks, centered on the circle for simplicity, marked T_3 and T_4 in the figure. The boundary is now completely covered.

The outer radius of the Laurent disk L_1 is determined as in Section 2.4, which still leaves an uncovered internal region. This remaining open region is covered by a central Taylor disk, marked T_2 , with radius of convergence 0.7. This central Taylor disk as taken as reference, which means that the integration constant is 0,

$$z = f(s = 0) = 0, \quad (4.10)$$

from which all other integration constants will be matched. The central Taylor disk overlaps with the Frobenius disks, except F_3 and F_4 , which will be matched at points marked by bullets \bullet in the overlapping region.

The Laurent disk is also matched with the central Taylor disk, then the Frobenius disks F_3 and F_4 with the Laurent disk.

A tiny circular-arc triangle is left uncovered between the Laurent disk and the Frobenius disks F_3 and F_4 . This is a direct result of limiting the numerical radius of convergence to 0.7 of the theoretical; the uncovered triangle would only have vanished by using a ratio of at least 0.8. Therefore a small Taylor disk, T_1 , is placed over the triangle on the inner Laurent circle, and it is matched at the indicated point with the Laurent disk (not the central Taylor disk).

There are now altogether 11 disks to cover the boundary as well as all of the interior.

In a computer program, all the information so far is stored in a table to be accessed when the series expansions are executed.

TAYLOR SERIES. The integrand consists of the factors

$$g(s) = (s - s_{a1})^{-\alpha_1} \cdots (s - s_{a6})^{\alpha_6} = g_1(s) \cdots g_6(s). \quad (4.11)$$

Each factor is expanded in a Taylor series by the Binomial Theorem,

$$g_1(s) = \underline{S} \cdot \bar{g}_1, \dots, g_6(s) = \underline{S} \cdot \bar{g}_6, \quad (4.12)$$

and the central Taylor series is obtained by the convolution product

$$g(s) = \underline{S} \cdot \bar{g} = \underline{S} \cdot \bar{g}_1 * \cdots * \bar{g}_6. \quad (4.13)$$

The integral is straightforward:

$$f(s) = \underline{S} \cdot \bar{f}, \quad \bar{f} = \int \bar{g}, \quad (4.14)$$

with integration constant 0 in view of equation (4.10).

FROBENIUS-TAYLOR SERIES. For the expansion about a particular singular point s_{ak} , the variable s is transformed

$$u = s - s_{ak}, \quad (4.15)$$

and the function is written

$$g(u) = (s_{ak} - s_{a1} + u)^{-\alpha_1} \cdots u^{-\alpha_k} \cdots (s_{ak} - s_{a6} + u)^{-\alpha_6} \quad (4.16)$$

$$= u^{-\alpha_k} \times g_1(u) \cdots g_6(u) \quad (4.17)$$

with g_k left out. Each factor is expanded in a Taylor series by the Binomial Theorem

$$g_i(u) = \underline{U} \cdot \bar{g}_i, \quad (4.18)$$

so that the Frobenius series is obtained by the product

$$g(u) = u^{-\alpha_k} \times \underline{U} \cdot \bar{g}_1 * \cdots * \bar{g}_6 \quad (\text{without the factor } \bar{g}_k) \quad (4.19)$$

$$= u^{-\alpha_k} \times \underline{U} \cdot \bar{g}_F. \quad (4.20)$$

The integration, as described in Section 2.3, produces the integral

$$f(u) = f_{F0} + u^{-\alpha_k+1} \times \underline{U} \cdot \bar{f}_F + h(\log u). \quad (4.21)$$

FROBENIUS-LAURENT SERIES. Let the center of the Laurent disk (which is actually an annulus) be s_0 , therefore for the expansion around the center, the variable s is transformed

$$u = s - s_0. \quad (4.22)$$

The factors that have a singularity within the Laurent annulus are, in this example,

$$a_1(s) = (s_0 - s_{a3} + u)^{-\alpha_3} (s_0 - s_{a4} + u)^{-\alpha_4}. \quad (4.23)$$

These two factors can be expanded by the Binomial Theorem into a Laurent series

$$a_1(u) = u^{-\alpha_3} u^{-\alpha_4} \left(1 + \frac{s_0 - s_{a3}}{u}\right)^{-\alpha_3} \left(1 + \frac{s_0 - s_{a4}}{u}\right)^{-\alpha_4} \quad (4.24)$$

$$= u^{-\alpha_3 - \alpha_4} \times \underline{U} \cdot \tilde{a}_{13} \times \underline{U} \cdot \tilde{a}_{14}$$

$$= u^{-\alpha_3 - \alpha_4} \times \underline{U} \cdot \tilde{a}_{13} * \tilde{a}_{14}$$

$$= u^{-\alpha_3 - \alpha_4} \times \underline{U} \cdot \tilde{a}_1. \quad (4.25)$$

The remaining factors that have singularities outside the Laurent disk are expanded in Taylor series by the Binomial Theorem

$$a_2(s) = (s_0 - s_{a1} + u)^{-\alpha_1} \cdots (s_0 - s_{a6} + u)^{-\alpha_6} \quad (\text{without the factors 3 and 4}) \quad (4.26)$$

$$= \underline{S} \cdot \overline{a}_{21} * \overline{a}_{22} * \overline{a}_{25} * \overline{a}_{26}$$

$$= \underline{S} \cdot \overline{a}_2. \quad (4.27)$$

The two factors of the complete Laurent series are separated according to Section 2.2, producing a Frobenius-Laurent series and a Frobenius-Taylor series

$$g(u) = u^{-\alpha_3} u^{-\alpha_4} \left(\underline{U} \cdot \tilde{a}_1 \times \underline{U} \cdot \overline{a}_2 \right) = u^{-\alpha_3} u^{-\alpha_4} \times \underline{U} \cdot \tilde{b}_1 + u^{-\alpha_3} u^{-\alpha_4} \times \underline{U} \cdot \overline{b}_1. \quad (4.28)$$

The two terms of this expansion are integrated according to Section 2.3

$$f(u) = f_{F0} + h(\log u) + u^{-\alpha_3 - \alpha_4 + 1} \times \underline{U} \cdot \tilde{b}_1 + u^{-\alpha_3 - \alpha_4 + 1} \times \underline{U} \cdot \overline{b}_2. \quad (4.29)$$

Care must be taken in the collection of the two powers of u that the branches at s_{a3} and s_{a4} are specified in a continuous manner. Otherwise another factor of the form $e^{2i\pi\alpha}$ will have to compensate for the jump.

MATCHING. The integration constant of the central Taylor series is set at 0. The sequence of matching consists of evaluating the series of two overlapping disks a and b , and equating at the common matchpoint s_m

$$a_{F0} + a_F(s_m) = b_{F0} + b_F(s_m) \quad (4.30)$$

in which the integration constant b_{F0} is the only unknown.

All Taylor integration constants are included as 0th element of the corresponding convolution number. The Laurent and Frobenius integration constants are kept in a separate table.

RESULT. The polygon is shown in Figure 4.3, the mapping defined graphically by plotting the same function $\log(s)$. A particular extreme example has been chosen by specifying the turning angles

$$a_1 = 140^\circ, \quad a_2 = 140^\circ, \quad a_3 = 140^\circ, \quad a_4 = 90^\circ, \quad a_5 = -240^\circ, \quad a_6 = 90^\circ.$$

There is one overlapping region, starting at point 5, which is called a winding point [28]. In the overlapping region, the function $s = f^{-1}(z)$ is a multivalued function, a feature that is physically possible only for a two-dimensional sheet. The multivalued z is also obtained by the numerical integration methods using the explicit integral $f(s)$. But such a function cannot be obtained in the z -plane with boundary element methods, and would be very difficult to implement with finite difference methods in the z -plane.

For practical purposes, the accuracy need not be more than the accuracy of the graphic display; in this example, the series length is $n = 10$.

The function $f(s)$ from Figure 4.3 is a newly defined analytic function. To the user, the value $z = f(s)$ is obtained by one simple call of a computer routine. Within this routine the appropriate convergence disk is found and the corresponding series coefficients used. The first analytic derivative $g(s)$ is available, and higher analytic derivatives can easily be obtained from the series expansions in their respective disks.

At first it may seem that the representation of the result by as many as 11 series is quite a complication. On closer analysis, however, this turns out to be the computational advantage of the method. Details around one corner are much better described by the local series as would be possible with one uniform function. The influence of other corners is still contained in the

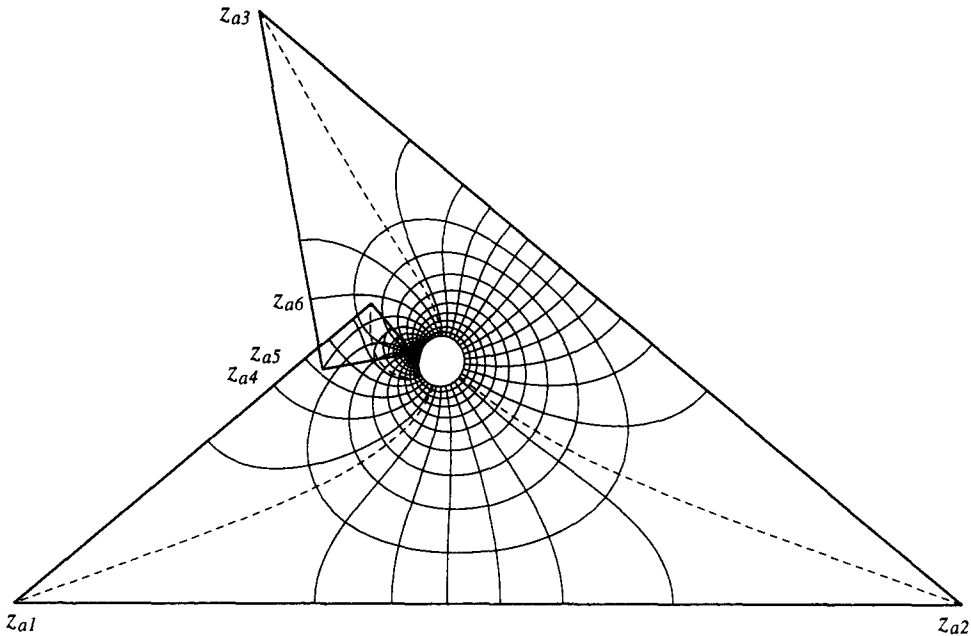
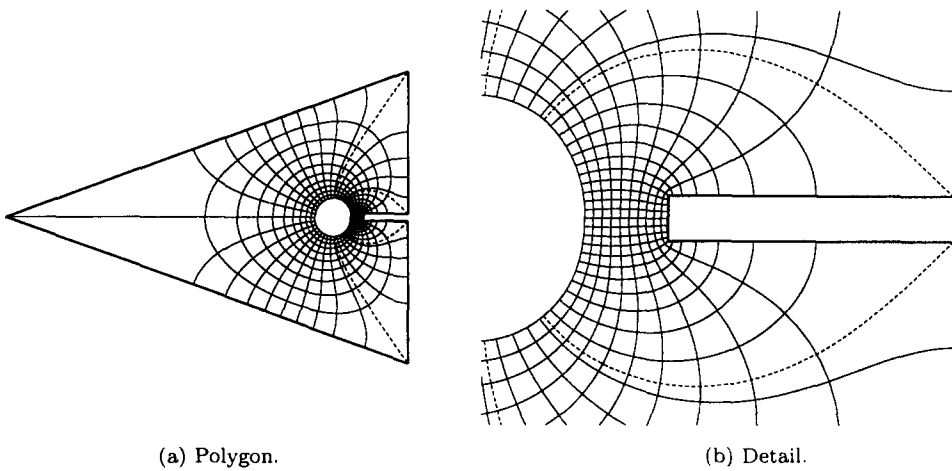


Figure 4.3. Mapped internal polygon.

local series, but less the further away they are. The series factor from a far corner converges very quickly to small coefficients, as can be seen from the binomial expansion formula. Because the radius of convergence is adjusted according to the closeness of corners, the details within each convergence disk are captured with the same relative accuracy for the constant series length. To demonstrate this property, another interior polygon is shown in Figure 4.4a with the mapped function $\log(s)$, and series length $n = 15$. Even with the large relatively uniform region at the sharp corner, the details in the slot are captured accurately, shown enlarged in Figure 4.4b.



(a) Polygon.

(b) Detail.

Figure 4.4. Mapped internal polygon.

Another point that is interesting to consider is whether a solution in this form is only possible with the aid of the modern computer, or whether it would have been treated in a different “analytical” way in the pre-computer era. From what was said before, each mapping is a new function which can be compared to the “special” functions of the past; this idea is conveyed by the function symbol of equation (4.8). In the past, the ordinary transcendental functions, and later the higher and special, were computed with whatever computational means were available at the time, and the numerical values printed in dedicated books, the existence of which was implicitly

an essential part of the use of any such function, even in analytic context. Therefore, the method here is the same, using the present available computational tool, only that it computes so much faster, and alleviates the necessity to print the numerical values in a book. It is the computational speed and storage facility that makes this method look like solving a problem rather than defining a new function. The convolution number method may then well be termed as: solving a problem by defining and evaluating a new function which is defined by the problem.

4.4. Programming Considerations

The solution of the Schwarz-Christoffel transformation can be divided into three parts. The first is the topological problem to determine convergence disks to cover the unit s -disk. This part of a program sets up a table of Frobenius, Laurent, and Taylor regions as shown in Table 4.1. The Frobenius table contains the center point s_0 of the disk, the numerical convergence radius r_F , the index α , the information about the direction of the branch in R_p , the logarithmic term position m , and the constant of integration f_{F0} . We have not allocated a position for the numbers α_i , m , f_{F0} in the Frobenius convolution number in Section 2.3, so that the table is a supplement of the actual Frobenius number. The table for the Laurent regions contains the same information, except that it contains two radii of convergence. The first two entries in the Laurent table are the first and last numbers of the enclosed singularities. The table for the Taylor regions contains the only information necessary for the Taylor disks, which are the center s_0 and the radius of convergence r_T . The integration constant is contained in the Taylor convolution number. All tables contain some frequently used redundant information.

Table 4.1. Tables of regions.

Frobenius Regions

c	s ₀ ()		r _F	α	φ	m	f _{F0}
	s _x	s _y					
1							
⋮							
N _c							

Laurent Regions

l	i ₁	i ₂	s ₀ ()		r _L		α	φ	m	f _{L0}
			s _x	s _y	r _i	r _o				
1										
⋮										
N _l										

Taylor Regions

t	s ₀ ()		r _T
	s _x	s _y	
1			
⋮			
N _t			

Match Table

r	j	k	s _m	
			s _x	s _y
1				
⋮				
N _r				

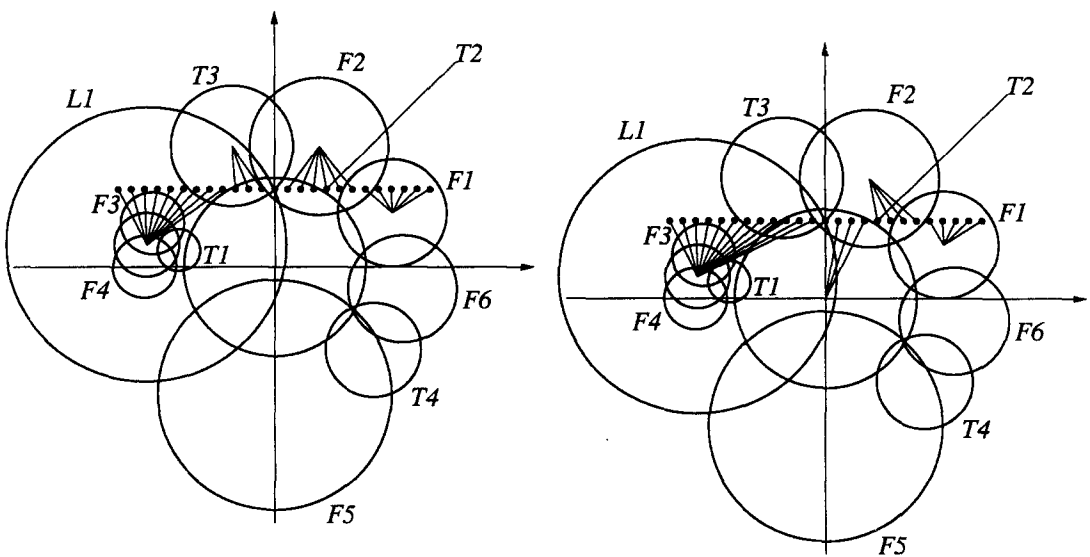
At the same time, a match table is set up, where the sequence of disks j is listed in which the constants of integration are determined by matching with other disks k , and the matching point s_m in the overlapping region. In the first part of the computation, the constants of integration are not yet known.

The second part of the program is the expansion and the integration of the Schwarz-Christoffel function in each disk, using the centers from the tables. The coefficients are entered in separate coefficient tables for Frobenius, Laurent, and Taylor expansions, according to one fixed length n that is chosen for the program. The Laurent tables contain double the amount of coefficients, due to the split into a Frobenius-Taylor and a Frobenius-Laurent part. The routine for evaluation then always uses these tables. The evaluation routine is used to determine the constants of integration in the sequence stored in the match table, and stores them in the regions tables and the Taylor convolution numbers, respectively. The completed tables and coefficients are stored in hard memory for further use of the SC-function.

The third part is the actual use of the expansions for evaluation of z of the SC-function at a chosen point s . This is a single function routine, using the stored tables and coefficients.

The first step in evaluation is to find in which convergence disk this point lies, by a search routine for this purpose. Several options can be used. The simplest is to scan the disks in the order of the tables until the first is found in which the distance from s to s_0 is less than the convergence radius. The corresponding coefficients are then picked up from the coefficient table, and the constants of integration from the regions tables if necessary. An improvement in efficiency can be achieved by searching always in the Taylor disks first, then the Frobenius disks, and last in the Laurent disks. The Frobenius series takes longer to evaluate, and the Laurent series takes two times as long as the Frobenius series.

An alternative method is to search through all disks to find the one where the distance relative to the convergence radius s/r is the smallest, although such a method is not consistent with the assumption that sufficient accuracy is achieved within the whole region of convergence. This search method is shown diagrammatically in Figure 4.5a. A number of consecutive points where the function has to be evaluated is shown along a straight line, and the lines connecting these with the centers indicate which region is used. When the SC-function has to be evaluated at a sequence of close points, which is the case for the plot of the lines in Figure 4.3, and when the number of disks is large, a more efficient method is to test first whether the point s still lies in the previously determined disk. In such a case, a further search is not necessary, and all the transfer of coefficients from the coefficients tables to a series evaluation routine does not have to be done over again. This alternative method is shown in Figure 4.5b for the same line of points to be evaluated, the sequence of points being from left to right.



(a) Nearest relative distance.

(b) Previous disk if possible.

Figure 4.5. Search for convergence disks.

When plotting on the computer screen, advantage can be taken of the extra dimension that color offers. The lines can be plotted in a different color for Frobenius, Laurent, and Taylor series, and another color for the perturbation forms that are described in the following sections.

The covering of the s -disk by convergence disks is quite similar to the Finite Element Method. The disks resemble analytical elements, although with overlapping boundaries, and each element carries its own set of instructions to compute the function $f(s)$.

4.5. Accuracy

With a 7-digit machine we can usually achieve 5- to 6-digit accuracy. It is often required to produce tables to 6- or 7-digit accuracy; then double precision tables can be used.

Certain arrangements of terms in analytical equations cause great loss of accuracy during computation, for example, small differences of large values. We call such posed equations *ill-determined*. We have derived the expression *ill-determined* or *well-determined* from the use of the word *undetermined* for the expression $0/0$. It refers to the arrangement of terms to overcome inaccuracy from decimal rounding of numbers. We distinguish this condition from *ill-conditioned* which is used for matrices, which also results in numerical inaccuracy, but is an inherent property of a matrix described by a condition number, independent of numerical accuracy.

If a computation contains ill-determined equations, accuracy may drop by orders of magnitude. In that case double precision calculations are often used to regain 5- to 6-digit accuracy. But any ill-determined system of equations can be transformed analytically to a well-determined system, therefore double precision is not necessary. We do not believe that double precision should be used to rescue an ill-determined system or a badly written program, to get single precision results, because this leaves no reserve, and merely postpones the real problem. Rather, double precision can be used to check single precision results. Except for the part in Section 3.3, all the computations in this treatise are made with single precision.

In SCT problems, it often occurs that some points are very closely spaced on the circle, which is called crowding. Crowding is not a problem reserved for the SCT, it is a common problem in conformal mapping generally. In fact, the very diversity of conformal mapping depends on this property. Double precision may then be justified to extend the range of problems by orders of magnitude to get single precision solutions.

A related problem comes from the method which we use to derive a potential function $w(z)$ implicitly, by first deriving the function $w(s)$ in the circle in the s -plane, and then using the transformation $z = f(s)$ as parametric equation to evaluate $w(z)$. Here it may occur that the values of $w(s)$ are crowded at a singular point s_k , such that $w(s) \xrightarrow{s/s_k} \infty$. In that case, we can develop a well-determined perturbation form by a local transformation of the boundary, several examples of which are in the following sections. But the perturbation form does not eliminate the crowding problem on the circle.

A general method to eliminate crowding is not available yet, but in several particular cases it has been done successfully. It consists of transforming the boundary region of crowded points to such a large boundary that points are placed well apart, and transforming the SC formula accordingly. An example is the transformation of the circular boundary of the s -plane on the real axis of the t -plane, which Floryan [38] has used to solve the periodic polygon problem. In another case [39], Floryan has transformed the boundary to two infinite lines, according to [40], to solve the problem of the periodic channel polygon. The same transformation method has been used in [9] with extreme success to treat elongated regions. It seems that this method can be extended to multiple crowded centers. It may be a future possibility to apply our method of covering the pre-mapping region with convergence disks to such transformed boundaries.

Even without any crowded points, a large distortion occurs at corners with small angle convex corners. At a corner, the differential becomes

$$dz = g_0 \left(\hat{i} e^{\hat{i}\phi} \right)^{1-\alpha_i} d\phi^{1-\alpha_i}. \tag{4.31}$$

If the included angle of the corner is 0.2π , then $1 - \alpha_i = 0.2$. Therefore an error in the last digit of s , $ds = 10^{-7}$, causes a change of $dz = 10^{-1.4}$, which is an error in the 2nd digit. The effect of this error is that sharply convex corners cannot be computed accurately.

Full machine accuracy of any well-determined system of equations can be achieved with analytical or numerical integration methods equally well. The convolution number method can be interpreted as a high order numerical integration, where the matching corresponds to a numerical integration step. Let the radius of a convergence disk be r , the length of convolution number n , the finite difference step ϵ of a k^{th} order numerical integration, then we can write the symbolic equation

$$\text{convolution number method} \xrightarrow[\epsilon, k]{r, n} \text{numerical integration}, \tag{4.32}$$

where accuracy is invariant.

5. SPECIAL INTERNAL POLYGONS

These are problems where infinities occur and the mapping of the s -plane on the polygon becomes ill-conditioned. Another mapping of the form $z(w, s)$ is then developed. Matching near infinity is dictated by the form of $w(s)$ near infinity.

5.1. Uniform Flow Along a Wall

A wall in the plane in this context consists of a half-infinite straight line on the left, joined by a perturbation, like a step or groove, consisting of straight line segments, to a straight half-infinite line on the right, in the same direction but possibly offset. The wall is considered as an interior polygon, with the turning angle at infinity 360° , and therefore the sum of the turning angles of the perturbation is 0. The problem is to analyze the flow along this wall which is uniform at infinity.

Analytic solutions in terms of elementary functions are available for the rectangular step in the wall [28,31], and for the angular step if the angles are in a rational ratio [28,41]. The solution of the rectangular groove or ridge is available in terms of elliptic integrals [36]. Solutions of many other configurations with right angles in terms of elementary functions are listed in [28,41,42]. In the manner described below, such special solutions are all expressed by their original series by one single method.

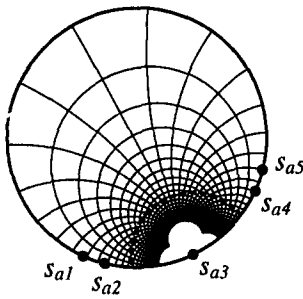
The mapped flow in the s -plane is the flow of a doublet situated at the cornerpoint s_u which maps to infinity in the z -plane, with the axis tangent to the circle,

$$w = c + \mu \frac{-\hat{i} s_u}{s - s_u}, \tag{5.1}$$

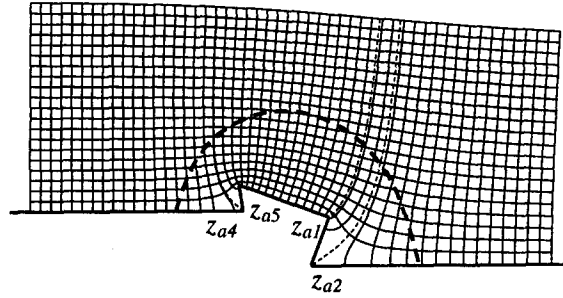
where μ is the strength of the doublet. This flow is shown in Figure 5.1a, where the point s_{a3} maps on infinity. An example of this wall flow in the z -plane is shown in Figure 5.1b. The numbers s_{ai} on the circle are specified with one real variable ϕ_i , which is the phase angle (argument in old terminology). The parameters for this example are

$$\begin{aligned} a_1 &= -90^\circ, & a_2 &= 110^\circ, & a_3 &= 360^\circ, & a_4 &= 100^\circ, & a_5 &= -120^\circ, \\ \phi_1 &= 245.27^\circ, & \phi_2 &= 255.27^\circ, & \phi_3 &= 295.27^\circ, & \phi_4 &= 335.27^\circ, & \phi_5 &= 345.27^\circ. \end{aligned}$$

The solution of $z = f(s)$ in terms of series for the appropriate convergence disks is carried out as in the example of Section 4.3. The parameters of the mapped flow in the circle in the s -plane are found by considering the uniform flow at infinity and the mapping at infinity.



(a) Wall-flow in circle.



(b) Wall-flow in physical plane.

Figure 5.1. Flow along a wall.

Let the point s_u be the point that maps to infinity, then the Frobenius series of the integrand around s_u becomes

$$g(s) = (s - s_u)^{-2} (a_0 + a_1(s - s_u) + a_2(s - s_u)^2 + a_3(s - s_u)^3 + \dots), \quad (5.2)$$

and the integral according to equation (2.27) can be written in the form

$$z = f(s) = z_0 + \frac{b_0}{s - s_u} + b_1 \log(s - s_u) + b_2(s - s_u) + b_3(s - s_u)^2 + \dots \quad (5.3)$$

$$\equiv z_0 + \frac{b_0}{s - s_u} + b_1 \log(s - s_u) + f_p(s), \quad (5.4)$$

where $f_p(s)$ is a perturbation term for small $s - s_u$. The numerical boundary of the Frobenius disk is shown by the thick dotted line (barely visible) in Figure 5.1a.

If the slope of the wall is described by a complex number \hat{u} of unit magnitude, then the flow at infinity must tend to the uniform flow at infinity which is parallel to the wall, given by the complex potential⁵

$$w_\infty \equiv P + \hat{i} \psi = \check{u} z, \quad (5.5)$$

where \check{u} is the complex conjugate of \hat{u} . Therefore to be compatible with equations (5.1) and (5.4), the complex potential of the flow in the s -plane is

$$w = \check{u} \left(z_0 + \frac{b_0}{s - s_u} \right). \quad (5.6)$$

Then it follows from equations (5.1) and (5.6) that

$$\check{u} = \frac{(-\hat{i} s_u)/(b_0)}{|s_u/b_0|} = \frac{-\hat{i} s_u}{b_0} |b_0|, \quad (5.7)$$

where b_0 is obtained from the series solution of equation (5.3).

To map w in the physical plane, the value of s for any given w is found from equation (5.6) and substituted into the appropriate series in all other convergence disks, to compute z as in Section 4.3.

The mapping around infinity may be treated differently to obtain a well-determined form for large w , i.e., small $s - s_u$. The flow along the wall consists actually of the mapping of the w -plane on the wall. For all values of s in the Frobenius convergence disk around s_u , the equation (5.4) is put into the form using equation (5.6),

$$z = \hat{u} w + b_1 \log \frac{b_0}{\hat{u} w - z_0} + f_p(s), \quad (5.8)$$

⁵We use the form where $\frac{dw}{dz} = u - \hat{i} v$ as in most engineering texts, not $-\frac{dw}{dz} = u - \hat{i} v$ as in most mathematical texts.

which is a well-determined perturbation form for large w and z . For a given value of w , the value of $s - s_u$ is found from equation (5.6) and substituted only into the perturbation term $f_p(s)$. The perturbation series also needs much less terms, typical $n = 5$ when in the other series $n = 20$ is required. In effect, $f_p(s)$ is a half-infinite Laurent series in the variable $\hat{u}w - z_0$, with an infinite outer radius of convergence in the w -plane.

The mapping of the convergence disk is shown in the z -plane in Figure 5.1b as the area bounded by the thick dotted line to infinity. The offset between the wall boundaries between $+\infty$ and $-\infty$ is given by the logarithmic term as $b_1\pi$.

Note that there were two steps to arrive at equation (5.8). The first was to relate a uniform z -plane to a potential w_∞ in equation (5.5), and the second to relate the complex potential w to the s -plane in equation (5.6), which is not the same as w_∞ in equation (5.5). We can consider the potential w_∞ in equation (5.5) as an auxiliary uniform plane, and the actual potential w in equation (5.6) as a flow inside this plane, while the two may be independent of each other. This means that the nearly uniform mapping towards infinity in equation (5.8) can be expressed independent of an actual flow w in it.

5.2. Half-Infinite Body in Uniform Flow

A half-infinite body in the plane consists of two half-infinite straight lines on the right a distance h apart, joined by straight line segments forming the nose of the body. The half-infinite body is considered as an interior polygon, with the turning angle at infinity 540° , and therefore the sum of the turning angles of the nose is -180° . The problem is to analyze the flow around this body in uniform flow. A well-known example is the half-infinite rectangular channel [31,41]. For many other shapes, solutions in terms of elementary functions are available, but only if the angles are right angles [28]. In the general case, the series expansion must be used, which may in some cases even be simpler than the combination of many elementary multivalued functions.

The complex potential of the flow within the unit circle in the s -plane can be shown to be, e.g., using Milne-Thomson's circle theorem,

$$w = \nu \left(\frac{-s_u^2}{(s - s_u)^2} + \frac{-s_u}{s - s_u} \right) + \mu \frac{-\hat{i} s_u}{s - s_u}, \tag{5.9}$$

where ν and μ are the strengths of the quadruplet and the doublet, respectively. The ratio of $\mu : \nu$ determines where the stagnation point on the circle is going to be. The mapped flow within the unit circle in the s -plane is shown in Figure 5.2a, which is the sum of a quadruplet and a doublet at the point s_{a5} , which maps on infinity in the z -plane. An example of the flow around a body is shown in Figure 5.2b, with a stagnation point on the foremost corner. The parameter values for this example are

$$\begin{aligned} a_1 = -20^\circ, & \quad a_2 = -140^\circ, & \quad a_3 = 30^\circ, & \quad a_4 = -50^\circ, & \quad a_5 = 540^\circ, \\ \phi_1 = 50^\circ, & \quad \phi_2 = 140^\circ, & \quad \phi_3 = 270^\circ, & \quad \phi_4 = 290^\circ, & \quad \phi_5 = 350^\circ. \end{aligned}$$

Let the point s_u be the point that maps to infinity, then the Frobenius series of the integrand around s_u becomes

$$g(s) = (s - s_u)^{-3}(a_0 + a_1(s - s_u) + a_2(s - s_u)^2 + a_3(s - s_u)^3 + a_4(s - s_u)^4 + \dots) \tag{5.10}$$

and the integral according to equation (2.27) can be written in the form

$$z = f(s) = z_0 + \frac{b_0}{(s - s_u)^2} + \frac{b_1}{s - s_u} + b_2 \log(s - s_u) + b_3(s - s_u) + b_4(s - s_u)^2 + \dots \tag{5.11}$$

$$= z_0 + \frac{b_0}{(s - s_u)^2} + \frac{b_1}{s - s_u} + b_2 \log(s - s_u) + f_p(s). \tag{5.12}$$

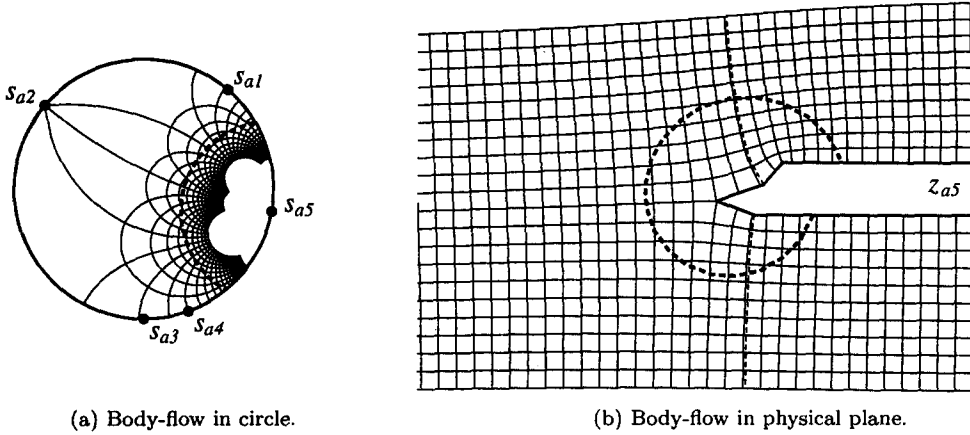


Figure 5.2. Flow along half-infinite body.

If the slope of the wall is described by a complex number \hat{u} of unit magnitude, the uniform flow at infinity parallel to the body is

$$w_\infty = \hat{u} z. \quad (5.13)$$

To be compatible with equations (5.9) and (5.12) when $s - s_u \rightarrow 0$, the largest terms must coincide, from which follows that

$$\hat{u} = \frac{(-s_u^2)/(b_0)}{|-s_u^2/b_0|} = \frac{-s_u^2}{b_0} |b_0|, \quad (5.14)$$

$$\nu = |b_0|. \quad (5.15)$$

To fix the stagnation point on a point s_0 on the circle, $\frac{dw}{ds}(s_0) = 0$ of equation (5.9) produces

$$\mu = \hat{i} \frac{s_0 + s_u}{s_0 - s_u}, \quad (5.16)$$

which is a real number. Alternatively, if for some physical reason μ is given, the stagnation point follows from equation (5.16).

To map w in the physical plane, the value of s for any given w is found by solving the quadratic equation equation (5.9) for s , and substituting into the appropriate series of the corresponding convergence disks, to compute z as in Section 4.3. The only difficulty is to determine the proper branch such that s falls inside the unit circle.

Also in this problem, the mapping at infinity is treated differently to obtain a well-determined form for large w , i.e., small $s - s_u$. From equations (5.9), (5.14), and (5.15)

$$\frac{b_0}{(s - s_u)^2} = \hat{u}w + \left(-\frac{b_0}{s_u} + \hat{i} \mu \hat{u} s_u \right) \frac{1}{s - s_u}, \quad (5.17)$$

$$\frac{1}{s - s_u} = \frac{1}{b_0} \left(\hat{u}w(s - s_u) - \frac{b_0}{s_u} + \hat{i} \mu \hat{u} s_u \right) \equiv q(w, s). \quad (5.18)$$

For any given large w in the Frobenius disk around s_u , s is found as before from equation (5.9). The term $s - s_u$ may now be inaccurate but is small, so that $q(w, s)$ is a well-determined form. Substituting equations (5.17) and (5.18) in equation (5.12) results in

$$z = z_0 + \hat{u}w + \left(-\frac{b_0}{s_u} + b_1 + \hat{i} \mu \hat{u} s_u \right) q + b_2 \log \left(\frac{1}{q} \right) + f_p(s), \quad (5.19)$$

which is the well-determined form near infinity, valid inside the Frobenius disk around s_u . The boundary of this disk, $s_u = s_{a5}$, is shown by the thick dotted lines in Figures 5.2a and 5.2b.

5.3. Nonuniform Flow

The body shape determined by the SCT and the flow impinging on it are of course independent. For example, the type of flow of Figure 5.2a could impinge on the wall of Figure 5.1b, as shown in Figure 5.3, and the type of flow of Figure 5.1a could go around the half-infinite body of Figure 5.2b, as shown in Figure 5.4. The flow in at infinity is then not uniform, and the physical existence of such a situation will have to be justified.

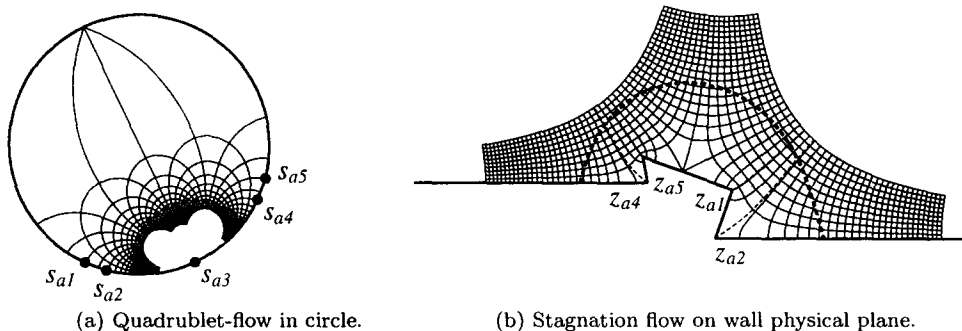


Figure 5.3. Nonuniform flow on wall.

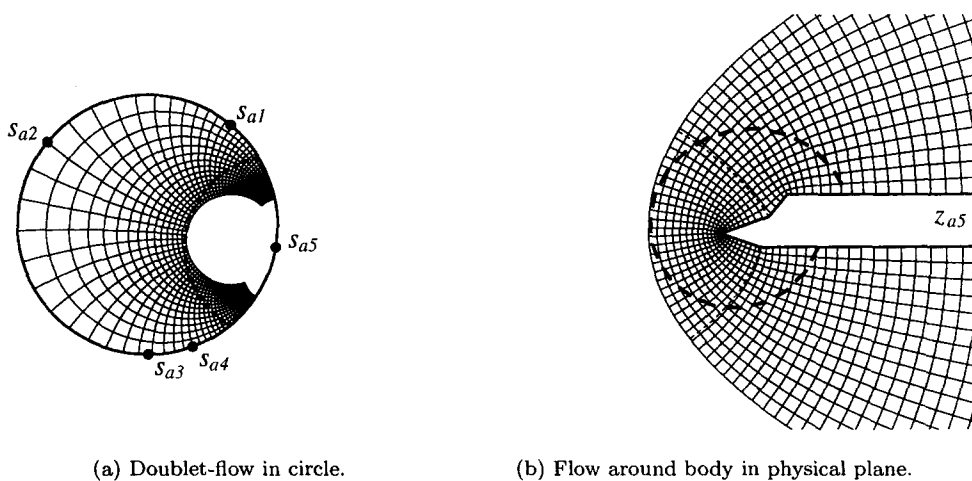


Figure 5.4. Nonuniform flow on body.

5.4. Channel Flow

Channel flow is characterized by a finite amount of fluid entering one or more channels and leaving another or other channels. Channel walls need not be parallel, and any of the entrance or exit channels can also occupy a sector of an infinite plane, like an opening in a flat wall, as in the examples given in [8], which can all be treated easily by the equations of this section. Channel branches can also overlap, strictly in the 2-dimensional case. Many analytic solutions are available for different channel configurations, also with step [28,41], but all solutions require special rational values of the angles, and become quite involved as rational ratios of angles consist of larger numbers, e.g., [15]. A branch in a canal with arbitrary branch angle is treated in [31], with an analytical solution for the integral properties of flow through each branch. But the details of the inner flow are still not known because the function obtained for $\frac{dz}{dq}$ cannot be integrated for arbitrary branch angle.

The general problem of arbitrary angles and not parallel walls cannot be solved in terms of any standard functions. Their solution in terms of series with convolution numbers are the same as

in the previous sections; the channel flows are only distinguished by a different flow in the unit circle which is mapped on the channel branches, and the peculiar perturbation forms at the far ends of the channels.

A typical flow in the s -plane is that of i sources and sinks, considered as sources with negative strength, on the circle, at the points which are mapped to the i infinite ends of the channel branches. The complex potential for this flow is

$$w = \sum \frac{m_i}{\pi} \log(s - s_{ai}), \quad (5.20)$$

where m_i is the amount of flow in channel i . From continuity, the sum of the source strengths must be zero, and it can be shown that then the circle is a streamline, consisting of all the mapped channel walls.

The mapped flow within the unit circle in the s -plane is shown in Figure 5.5a. It consists of four sources/sinks at the points s_{a1} , s_{a4} , s_{a6} , and s_{a8} , which are mapped on the channel with one inlet and three outlet branches shown in Figure 5.5b. The outlet at branch 6 has diverging walls.

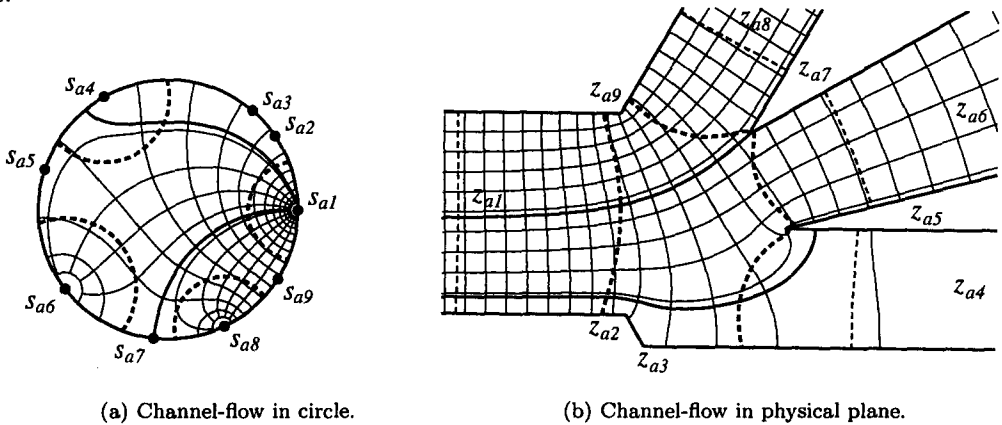


Figure 5.5. Flow in branched channel.

The strength m_1 of the inlet channel is chosen. The remaining three m_i are determined by the continuity equation, and two chosen points on the boundary as stagnation points. A stagnation point may be on a sharp corner, as at point z_{a7} , but it does not have to, as shown by the thick stagnation streamline which just misses the corner at z_{a5} . This arbitrary division of flow between the channels is physically determined by the pressures in the channel ends. For this example, the parameters are

$$\begin{array}{lll} a_1 = 180^\circ, & \phi_1 = 0.2^\circ, & m_1 = 1, \\ a_2 = -60^\circ, & \phi_2 = 35.2^\circ, & \\ a_3 = 60^\circ, & \phi_3 = 50.2^\circ, & \\ a_4 = 180^\circ, & \phi_4 = 120.2^\circ, & m_4 = -0.08173, \\ a_5 = -165^\circ, & \phi_5 = 162.2^\circ, & \\ a_6 = 195^\circ, & \phi_6 = 218.2^\circ, & m_6 = -0.38941, \\ a_7 = -150^\circ, & \phi_7 = 264.2^\circ, & \\ a_8 = 180^\circ, & \phi_8 = 296.2^\circ, & m_8 = -0.52886, \\ a_9 = -60^\circ, & \phi_9 = 328.2^\circ, & \end{array}$$

The series solution and the mapping is carried out as before for all points not near the infinity points.

Consider the Frobenius series equation (2.22) of the integrand $g(s)$, at any one of the infinity points s_u

$$g(s) = (s - s_u)^{-\alpha} (a_0 + a_1(s - s_u) + a_2(s - s_u)^2 + a_3(s - s_u)^3 + \dots). \quad (5.21)$$

The channel with parallel walls is characterized by

$$\alpha_u = 1; \quad (5.22)$$

therefore the integral will be of the simple form of equation (2.27),

$$z = z_0 + a_0 \log(s - s_u) + b_1(s - s_u) + b_2(s - s_u)^2 \dots \quad (5.23)$$

But from the flow in the s -plane, equation (5.20), the logarithmic term is

$$\log(s - s_u) = \frac{\pi w}{m_u} - \sum_{j \neq u} \frac{m_j}{m_u} \log(s - s_j); \quad (5.24)$$

therefore the well-determined form is

$$z = z_0 + a_0 \left(\frac{\pi w}{m_u} - \sum_{j \neq u} \frac{m_j}{m_u} \log(s - s_j) \right) + b_1(s - s_u) + b_2(s - s_u)^2 \dots \quad (5.25)$$

Noting further that in the channel of width h_u and slope \hat{u} ,

$$w \frac{s}{s_u} \rightarrow \frac{m_u}{h_u} \hat{u} z, \quad (5.26)$$

we find that the coefficient a_0 gives the channel geometry by

$$a_0 = \frac{\hat{u} h_u}{\pi}. \quad (5.27)$$

Note that equation (5.20) must be solved iteratively to find s for a given w at all ordinary points. The problem to find s from w near infinity by a well-determined form is solved by treating $\log(s - s_u)$ as a small single quantity in equation (5.20), and solving by the Newton-Raphson iteration. Convergence is fast, and in the example no problem occurred down to values of $|s - s_u| = 10^{-25}$, which is the value at the end of channel at z_{a4} in Figure 5.5b.

The channel with angular walls, which in the example is the diffusor at z_{a7} , is characterized by

$$\alpha_u > 1; \quad (5.28)$$

therefore the integral will be of the form of equation (2.23)

$$z = z_0 + (s - s_u)^{-\beta/\pi} (b_0 + b_1(s - s_u) + b_2(s - s_u)^2 \dots) \quad (5.29)$$

expressed for clarity in terms of the positive included angle

$$\beta = \pi(\alpha - 1). \quad (5.30)$$

To obtain a well-determined form at $s \rightarrow s_u$, the negative power must be replaced by w of equation (5.20), with the result

$$(s - s_u)^{-\beta/\pi} = e^{-(\beta/m_u)w} \prod_{j \neq u} (s - s_j)^{-m_j/m_u}, \quad (5.31)$$

and again the small values of $s - s_u$ for any given w are obtained by the iteration as described above. Equation (5.31) is equally valid for angles $\beta > \pi$. At an outlet $m_u > 0$, $\Re(w) \rightarrow +\infty$, and at an inlet $m_u < 0$, $\Re(w) \rightarrow -\infty$, while the angle α , or β , is the same positive number independent of the direction of the flow.

If α_u is an integer other than 1, e.g., a reversed parallel channel with $\beta = 2\pi$, then the integral contains both negative powers of $s - s_u$ and a logarithmic term. The negative powers are then replaced as in equation (5.31), while the logarithmic term is replaced as in equation (5.24).

The special case when α differs only slightly from a positive integer leads to the special form of the integral of equation (2.26),

$$z = z_0 + (s - s_u)^{1-\alpha} \sum_{i \neq k} b_i (s - s_j)^i + a_k \sum c_i (\log(s - s_u))^i. \tag{5.32}$$

Here again, to obtain a well-determined form $z(w, s)$, the leading negative power is replaced as in equation (5.31), and the logarithm is replaced as in equation (5.24). The resulting expression for z contains w now both in exponential form as well as in an infinite Taylor series.

In Figure 5.5, the Frobenius convergence radii around the four infinity points are shown by the thick dotted lines. The perturbation series form was used for 0.1 times the numerical Frobenius radius, and this boundary is shown by the thinner dotted lines in Figure 5.5b. The perturbation form could just as well have been used for the whole of the Frobenius convergence region, separate allowance having been made for the stagnation point near s_{a4} .

We note that while the mapping of the channels on the circle in the s -plane is fixed by the geometry of the cornerpoints s_{ai} , the mapping is also one of an infinite strip of the w -plane, but this mapping is dependent on how the flow distribution between the channels is chosen.

5.5. Elliptic Integral III

The elliptic integral of the third kind with real $\beta^2 > 0$

$$z = \int \frac{dt}{(1 - \beta^2 t^2) \sqrt{(1 - t^2)(1 - k^2 t^2)}} \tag{5.33}$$

is an SC mapping of the upper half of the t -plane on the interior of a polygon. Transforming to the interior of the unit disk in the s -plane with the bilinear transformation

$$s = \frac{1 + \hat{i} t}{1 - \hat{i} t}, \quad t = \hat{i} \frac{1 - s}{1 + s}, \tag{5.34}$$

we obtain

$$z = \hat{c}_2 \int \prod_{i=1}^7 (s - s_{ai})^{-\alpha_i}, \quad \sum_{i=1}^7 \alpha_i = 2, \tag{5.35}$$

which can be recognized as the standard form of the interior SCT according to Section 4.1. The points s_{ai} and turning exponents have the values

i	s_{ai}	α_i
1	\hat{i}	$\frac{1}{2}$
2	\hat{s}_k	$\frac{1}{2}$
3	\hat{s}_β	1
4	-1	-2
5	$\times \hat{s}_\beta$	1
6	$\times \hat{s}_k$	$\frac{1}{2}$
7	$-\hat{i}$	$\frac{1}{2}$

where the values on the circle are the mappings of the real parameters $t = \pm 1/\beta, \pm 1$, and $\pm 1/k$. The sequence of points corresponds to a particular value of β^2 . Point 4 is a winding point with a turning angle of -360° , which is at infinity in the t -plane. The turning angles at 3 and 5 are 180° and are therefore infinity points of half-infinite channels which overlap in two different planes. The two different planes of such a polygon with channel flow are shown in Figure 5.6. They join at the shown dotted lines.

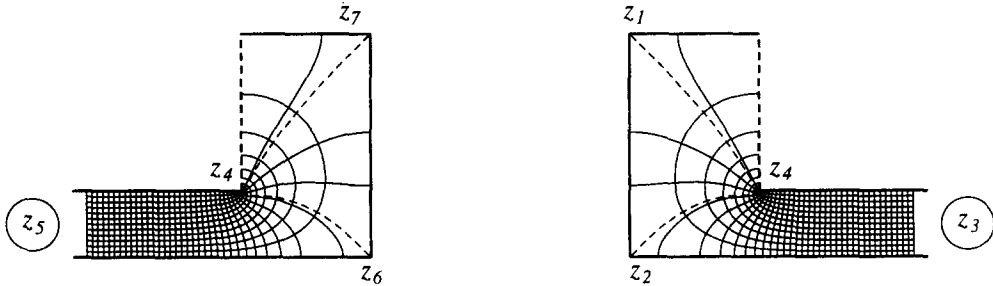


Figure 5.6. Elliptic integral III, $\beta^2 > 0$, as SC mapping.

5.6. Comparison with Published Numerical Integration Cases

The first examples for comparison were taken from Trefethen [3]. In Figures 5.7a–d, we show the streamlines from the SCT solution in channels with dimensions scaled from [3]. The results show exact agreement within plotted line width. We have plotted double the amount of streamlines for future reference.

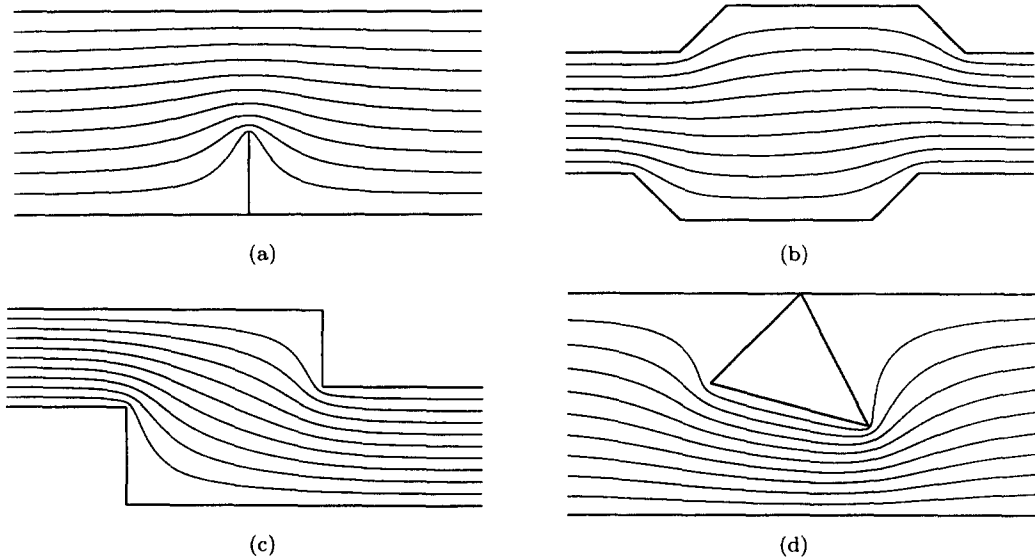


Figure 5.7. Channels 10(a)–10(d) of [3].

It is all the more surprising that our results do not agree well with other publications from workers that used Trefethen’s SCPACK, for example, the streamlines in the channel shown in Figure 2 of [11]. Another example are the two channel flows in Figures 5.8a and 5.8b. The dimensions were taken from Chuang *et al.* [8], who used another numerical integration. The same number of streamlines as in [8] is plotted. Comparing results, we find that in the regions of nonuniform flow there are serious discrepancies.

In [12], an electrostatic field is shown, which we have reproduced with our analytic method in Figure 5.9a, with the apparent boundaries from [12]. However, according to the stated boundary conditions in [12], the field should actually have infinite boundaries, resulting in a field as shown in Figure 5.9b.

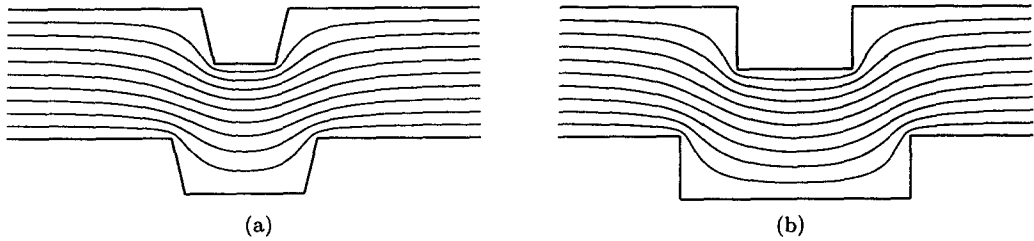


Figure 5.8. Streamlines in channel [8, Figure 6].

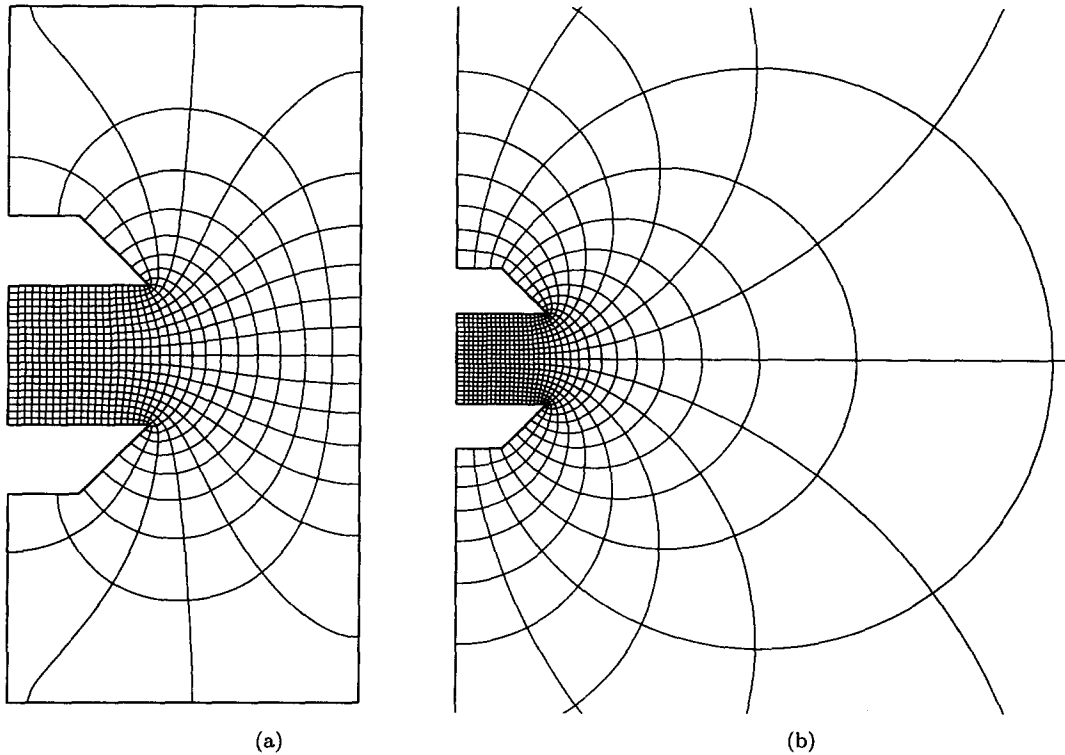


Figure 5.9. Electrostatic field [12, Figure 3].

6. REVERSION

6.1. Introduction

The terms *inversion* and *reversion* have often been used interchangeably, so that to avoid any confusion we define these terms as used in this section.

We use *inversion* as the term for the algebraic operation $1/x$ on a variable x , in the current algebra, and we also use the exponent symbol x^{-1} for this operation. Inversion of a function $f(x)$ is the inversion of the variable $y = f(x)$ for all values of x , $1/y = 1/f(x)$. This inversion is transformed in convolution algebra by the Taylor transform, see [20], into the operation

$$\frac{1}{(X \cdot \bar{f})} = X \cdot \bar{f}^{*-1}.$$

We use *reversion* as the customary term for the operation of creating the function $x = g(y)$ out of the function $y = f(x)$, an operation that has no algebra and cannot be transformed into an equivalent convolution algebra operation. The corresponding operation in convolution algebra is a process rather than a single algebraic operation. If the customary symbol -1 be used for this process, then we indicate it by the symbol used in [35], $x = f^{[-1]}(y)$.

Particularly referring now to the SCT, the forward form is the nonhomogeneous linear differential equation (4.1), with the scaling constant from equation (4.9),

$$\frac{dz(s)}{ds} = c_2 \prod (s - s_k)^{-\alpha_k} \equiv f(s_k, s), \quad (6.1)$$

which we will call the forward transformation, and the series solution $z(s)$, consisting of the set of expansions in the different convergence disks, is called the forward solution.

The *reversion* of the Schwarz-Christoffel transformation is the homogeneous nonlinear differential equation

$$\frac{ds(z)}{dz} = \frac{1}{c_2} \prod (s(z) - s_k)^{\alpha_k} \equiv \frac{1}{f(s_k, s(z))}, \quad (6.2)$$

where the parameters s_k remain the same. This corresponds to the form as posed by Trefethen [3] to be solved by an ODE solver “. . . to invert the Schwarz-Christoffel formula” in his terminology.

The iterative solution of s for a given value of z from the solution of equation (6.1) is not termed by us a reversion, but rather a *reverse* or *inverse solution* or *computation*. As example, the inverse SCT by Costamagna [5] is merely the inverse computation of the forward SCT-solution.

In this section, we present certain solutions of the reverse transformation that can be found by convolution algebra.

6.2. Parameters

The parameters s_k are as unknown in the reverse solution as in the forward SCT solution, and must be found by an iterative process if the problem is posed as a polygon in the z -plane. Therefore the known iteration method of the forward SCT may be used, which means the problem must be solved in the forward method first. Exceptions are the triangle, where the s_k are arbitrary, and the rectangle, where the s_k can be found by known explicit methods. It will be clear at the end of this section why we will not attempt to solve the parameter problem using the reverse SCT.

The reverse solution starts then with known parameters in equation (6.2) and its forward solution. From the same solution, the constants c_1 and c_2 will be known.

6.3. Taylor Series

Since the forward solution $z(s)$ is assumed to be known, the point on the z -plane corresponding to the origin of the s -plane is known. Choosing a center z_0 for the reverse expansion, the corresponding point s_0 must be found iteratively from the forward solution. This is effectively the constant of integration, and the iteration complies with the fact that the initial value of a first-order differential equation must be found algebraically, see [20]. Using the transformed variables

$$u = s - s_0, \quad v = z - z_0, \quad u_k = s_k - s_0, \quad (6.3)$$

equation (6.2) becomes

$$\frac{du(v)}{dv} = \frac{1}{c_2} \prod (u(v) - u_k)^{\alpha_k} \equiv \frac{1}{f(u_k, u(v))}. \quad (6.4)$$

The solution of equation (6.4) in the regular region of the z -plane is the nonunit Taylor series

$$\begin{aligned} u &= u_1 v + u_2 v^2 + u_3 v^3 + \dots \\ &\equiv \underline{V} \cdot \bar{u}, \end{aligned} \quad (6.5)$$

and the Taylor transform of equation (6.4) is

$$\bar{u}' = \frac{1}{c_2} \prod (\bar{u} - u_k \bar{\delta}_0)^{\alpha_k}, \quad (6.6)$$

which is solved by pointer convolution numbers [20] in each Taylor convergence disk.

The origin in the z -plane is arbitrary within the polygon, but the region of convergence is now a disk in the z -plane within all singular points. This disk has no resemblance to the Taylor disks of the forward SCT. The singular points are all corners that do not have a turning angle of π/n . But there are also many points outside the polygon where z maps on $s = \infty$, and are therefore singular points of $s(z)$, which limit the radius of the Taylor disk. We will demonstrate the Taylor solution in the following examples of special triangles and general rectangles.

6.4. Triangles

There are three and only three special triangles where there are no singularities of the reverse function $s(z)$ on the boundary. These are the three triangles shown in Figure 6.1. Let us now attempt to obtain the reverse solution of the equilateral triangle.

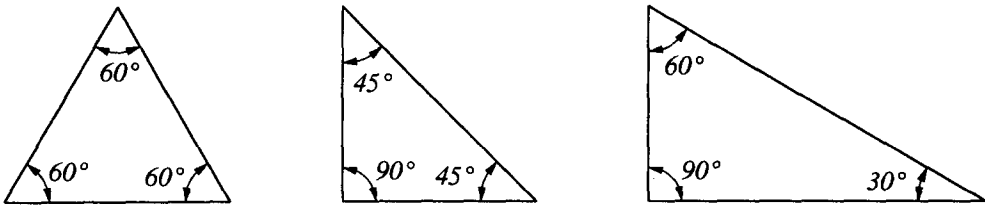


Figure 6.1. Three special triangles.

Choosing symmetrical parameters in the s -plane, the values for the triangle are according to Table 6.1.

Table 6.1.

Corner	a	ϕ	z
1	120°	0°	.8833216 + \hat{i} 1.529958
2	120°	120°	.8833216 + \hat{i} 1.529958
3	120°	240°	1.766643 + \hat{i} 0

Since no parameter iteration is necessary, we choose $s_0 = 0$ and $z_0 = 0$, and see where the triangle is going to be relative to the origin in the z -plane. Choosing the constant $c_2 = 1$, the differential equation to be solved is the convolution equation

$$\bar{s}' = (\bar{s} - s_1 \bar{\delta}_0)^{*2/3} * (\bar{s} - s_2 \bar{\delta}_0)^{*2/3} * (\bar{s} - s_3 \bar{\delta}_0)^{*2/3}. \quad (6.7)$$

The Taylor series is obtained as described above, and the result is shown in Figure 6.2a. The internal lines shown are mapped concentric circles in the s -plane, plotted by iterative solution of the Taylor series $s(z)$, using convolution number length $n = 20$. The reflection of the center z_0 about each of the sides is shown by a \bullet . These are the points where $s = \infty$ is mapped, therefore singularities of the function $s(z)$. The distance of these points happen to be the same as the distance of the corners, which then determine the radius of convergence of the Taylor series. The numerical radius, using the factor 0.7, is shown by the dotted circle. The corners of the triangle are therefore not included in the central Taylor series, and can therefore not be computed directly from the Taylor series. But the midpoints of the sides are well within the numerical Taylor disk. Furthermore, from the differentials in equation (6.1) at the singular points, the orientation of each side of the triangle is known, depending on the branch of the fractional power. From this information we arrive indirectly, but with great accuracy, at the dimensions of the triangle.

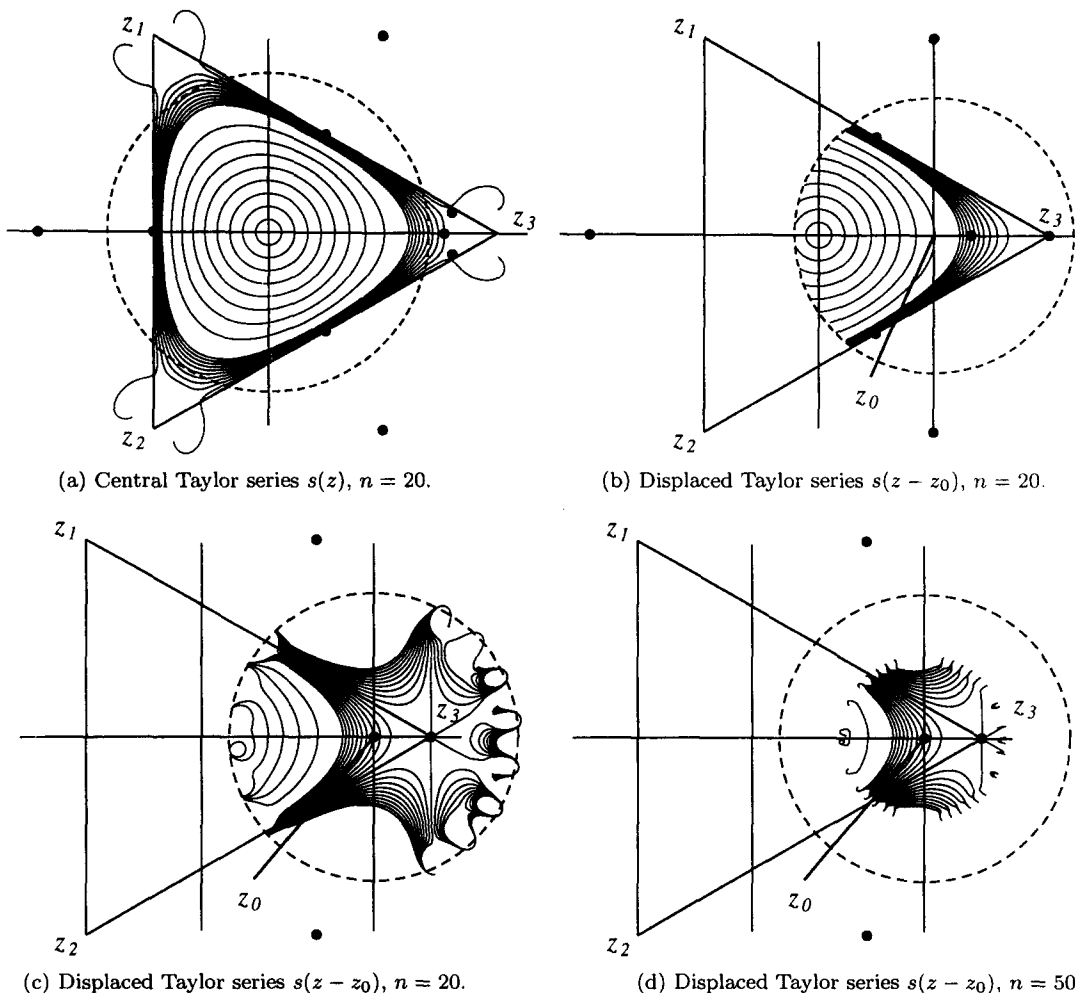


Figure 6.2. Reverse Taylor series of equilateral triangle.

The distorted shape of the mapped lines in Figure 6.2a verify clearly that there is no convergence near the corners. Also, that the zeros of the first and second derivatives, $s'(z)$ and $s''(z)$, should both lie on the corners. But they are actually found at the points shown by a \bullet , the zero of the first derivative in the center and two zeros of the second derivative straddling the symmetry line. Therefore, while the dimensions of the triangle can be determined from the reverse Taylor series, the actual function $s(z)$ near the corner must be determined with a second series.

As the next series we chose the center $z_0 = z_3/2$ for a Taylor disk. With the usual transformations, equation (6.7) becomes

$$\bar{u}' = (\bar{u} - u_1 \bar{\delta}_0)^{*2/3} * (\bar{u} - u_2 \bar{\delta}_0)^{*2/3} * (\bar{u} - u_3 \bar{\delta}_0)^{*2/3}. \tag{6.8}$$

The apparent numerical radius, determined again by the mapping of $s = \infty$, includes now the center of the triangle as well as the midpoints of the sides, so that we might still have one single Taylor series for all points within the triangle, using the symmetry. The accuracy of the mapping seemed quite satisfactory at $n = 20$, shown in Figure 6.2b. Yet we found the value of $|s''(z)| = 1$ at z_3 , instead of zero. We can therefore not claim an analytic result, within machine accuracy, which is the purpose of the convolution number algebra. Even when we increased n , we could not get better accuracy.

To show why this happens, we choose another point $z_0 = 0.75 z_3$ and use the previously determined values of the corners z_i , and the central series to determine s_0 iteratively.

The solution is shown by the same mapping of circles in Figure 6.2c with $n = 20$, and Figure 6.2d with $n = 50$. The reflected lines about the corner z_3 are also plotted, representing the analytic continuation of $s(z)$ outside the triangle. Instead of increasing the accuracy, the figures show clearly the the radius of convergence becomes smaller with increasing n . In fact, the results display a property similar as in asymptotic series, where the accuracy for a particular value of z increases first and then diverges with increasing n .

Inspection of Figure 6.2d reveals a convergence radius just beyond the corner z_3 . On examination we find the reason in the differential equation (6.8). In the computation of the term $(\bar{u} - u_3 \bar{\delta}_0)^{*2/3}$, our numerical convolution algebra cannot distinguish between an exact power of $2/3$ of an exact root, and a numerical approximation by digital computer. This particular factor is therefore divergent for all $|z - z_0| > |z - z_3|$, even if z_3 is a zero of the function $s(z) - s_3$, where theoretically a convergent series exists.

This is what causes the divergence shown so clearly in Figure 6.2d. Expressed differently, the method of computation of the convolution the factor is *unstable*, and due to the recursion affects the whole convolution number \bar{u} .

That the radius is apparently a little larger than $|z_3 - z_0|$ is due to the fact that the divergence is rather small near the theoretical Taylor expansion. The Taylor series including the corner z_3 still exists, but we cannot find a stable method to determine it.

The reversion of the SCT for the three special triangles must therefore be carried out as for a general triangle, assuming singularities at the corners. A central Taylor series is obtained first, then the reverse solution at the corners is obtained by the reversion of the Frobenius series, as presented further below.

6.5. The Rectangle

The rectangle as boundary occurs quite frequently, either in mechanics because of the simple engineering shape, or in potential problems as region in the complex potential plane, e.g., [12]. The mapping of the rectangle is an exceptional problem for the SCT in as much only one unknown parameter has to be determined, allowing series expansions in a single variable, the known parameter. These have been extensively developed in connection with the elliptic integral of the first kind.

In the forward SCT, the parameter is the modulus k in the standard Jacobi form of equation (3.1)

$$\zeta = F(t, k) = \int_0^t \frac{dt}{\sqrt{(1-t^2)(1-k^2t^2)}}.$$

The corresponding rectangle has the dimensions $2K \times K'$ in the ζ -plane, where K and K' are the complete elliptic integral and the associated complete elliptic integrals of the first kind. Here we use the notation ζ instead of the classic notation u .

The customary reversion is the mapping of the rectangle on the upper half of the t -plane by the Jacobian elliptic function $t = \text{sn}(\zeta)$. Our reversion is slightly different because we map on a circle in the s -plane, which avoids the infinity which is present in $\text{sn}(\zeta)$. The differential equation to be solved for $s(z)$ is

$$\frac{ds}{dz} = \frac{1}{c_2} (s - s_1)^{1/2} (s - s_2)^{1/2} (s - s_3)^{1/2} (s - s_4)^{1/2}. \quad (6.9)$$

If we choose four symmetric singular points on the circle, the relation between s and t of equation (5.34) is

$$s = \frac{\hat{i} - \sqrt{k}t}{\hat{i} + \sqrt{k}t}, \quad t = \frac{\hat{i} - 1 - s}{\sqrt{k} - 1 + s},$$

$$\phi_1 = 2 \arctan \sqrt{k}, \quad \phi_2 = \pi - \phi_1, \quad \phi_3 = \pi + \phi_1, \quad \phi_4 = 2\pi - \phi_1, \quad (6.10)$$

where ϕ_i is the phase of s_i . The integration constant c_2 corresponds to the chosen branches of the power functions in equation (6.9). The rectangle in the z -plane becomes a turned and scaled rectangle in the ζ -plane, by the ratio

$$z = \hat{i} c_2 \frac{1+k}{2} \zeta.$$

If the rectangle in the z -plane has base b and height h , the constant becomes

$$c_2 = \frac{h}{(1+k)K} = \frac{2b}{(1+k)K'}, \quad (6.11)$$

and the constant s_0 of the integral of equation (6.9) is determined by the position of the rectangle relative to the z -axes.

For a given rectangle, we determine the parameters k and K by using the following known relations and expansions, see [21,43],

$$\text{ratio} \quad \kappa = \frac{K'}{K} = \frac{2b}{h}, \quad (6.12a)$$

$$\text{nome} \quad q = e^{-\pi\kappa}, \quad (6.12b)$$

$$\text{theta function} \quad \vartheta_2 = 2q^{1/4} \left(1 + \sum_{n=1}^{\infty} q^{n^2+n} \right), \quad (6.12c)$$

$$\text{theta function} \quad \vartheta_3 = 1 + 2 \sum_{n=1}^{\infty} q^{n^2}, \quad (6.12d)$$

$$\text{modulus} \quad k = \frac{\vartheta_2^2}{\vartheta_3^2}, \quad (6.12e)$$

$$\text{complimentary modulus} \quad k' = \sqrt{1-k^2}. \quad (6.12f)$$

For the complete elliptic integrals we use the well-known series

$$\begin{aligned} K &= \frac{\pi}{2} \left(1 + \frac{1}{4}k^2 + \frac{9}{64} + \frac{25}{256}k^6 + \frac{1225}{16384}k^8 + \frac{3969}{65536}k^{10} + \dots \right) \\ &\equiv f_K(k), \end{aligned} \quad (6.13a)$$

$$\begin{aligned} K' &= \log \frac{4}{k} \left(1 + \frac{1}{4}k^2 + \frac{9}{64}k^4 + \frac{25}{256}k^6 + \dots \right) - \left(\frac{1}{4}k^2 + \frac{21}{128}k^4 + \frac{185}{1536}k^6 + \dots \right) \\ &\equiv f_L(k). \end{aligned} \quad (6.13b)$$

With the function notation defined by equations (6.13a) and (6.13b), we determine

$$\begin{aligned} K &= f_K(k) \text{ for } k^2 < 0.5, & &= f_L(k') \text{ for } k'^2 < 0.5, \\ K' &= f_L(k) \text{ for } k^2 < 0.5, & &= f_K(k') \text{ for } k'^2 < 0.5. \end{aligned}$$

With this information, c_2 is determined from equation (6.11). Note that in equation (6.12), the symbol for theta functions corresponds with that used in [21,22,43], while Lemczyk and Yovanovich [27] have used the symbol as in other texts, e.g., [44].

With all the parameters in the differential equation (6.9) known, we can proceed with the reverse solution of the SCT without need to perform the forward parameter iteration.

In the following example, we determine the reverse mapping $s(z)$ of the rectangle in the z -plane, with base $b = 3$ and height $h = 1$. The rectangle is shown in Figure 6.3a, with lines of $\log(s)$ to show the mapping visually.

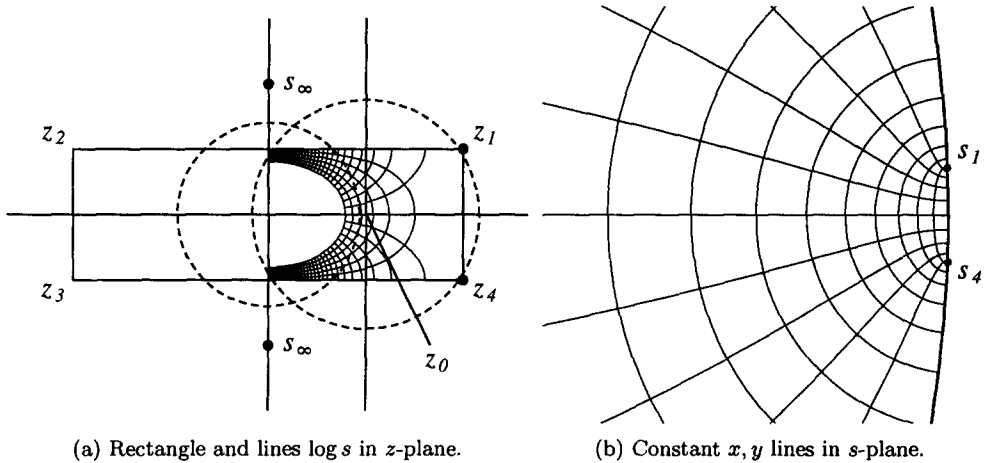


Figure 6.3. Mapping of rectangle by reverse Taylor series.

The corresponding constants as determined from equations (6.10)–(6.12) are

$$\begin{aligned} k &= .3227981 \times 10^{-3}, \\ \phi_1 &= 2.058597^\circ, \\ c_2 &= .6364143. \end{aligned}$$

Equation (6.9) is transformed to convolution numbers and solved by pointer numbers as an initial value problem. The initial value $s(z = 0) = 0$ is evident from symmetry, therefore we start with a central Taylor series. The infinity points of s are mapped on the reflections of the origin about the sides, the nearest ones shown as s_∞ in Figure 6.3a. These are the only singularities of $s(z)$, which limit the numerical convergence radius as shown by the central dotted circle, using the empirical ratio of 0.7. To cover the remaining region on the right, we put another Taylor series at the center z_0 halfway between the center and the right edge, which is just outside the inner Taylor disk. The second Taylor disk is again limited only by the two singularities shown, and passes just inside the corner points. In this case, we simply extend the numerical radius somewhat, using a larger length n for the expansions. For the central circle it becomes 0.75, and for the outer circle 0.721. Using the first Taylor series, the value $s_0 = s(z = z_0)$ is determined for the initial value of the second Taylor series, and the variables are transformed as in equation (6.3) to the new center.

The resulting two Taylor series are then used to cover the right half of the rectangle, and the left by using symmetry. The function $s(z)$ is displayed by means of constant x, y lines, enlarged near the boundary between s_1 and s_4 , in Figure 6.3b.

To test the accuracy at the corners z_1 and z_4 , we have computed the first derivative $\frac{ds}{dz}$, which should be zero. Within machine accuracy, this is only achieved at $n = 50$. The second derivative, $\frac{d^2s}{dz^2}$, is not zero as for the equilateral triangle. We have computed its value by means of the Frobenius expansion of the forward SCT as $-.0127354 + \hat{i}.3543014$ at the corner z_1 . This was verified by means of the reverse Frobenius series, as described later below, by the value of $-.0127356 + \hat{i}.3543029$, therefore accurate to ≈ 6 digits. The values obtained from the reverse Taylor series are given in Table 6.2.

Therefore, the reverse Taylor series has converged well at the corners, contrary to the expectation that it would diverge there due to the destabilizing square root factor in the differential equation. Apparently that divergence is much less pronounced than was the case for the triangle. On the other hand, the large value of n required for good accuracy may just be due to this divergent contribution. We note also a slight unsymmetry in the values. This is probably due to the rather small angle difference $\phi_1 - \phi_4$, typical of the large distortions in the SCT. Apparently this

Table 6.2.

n	$\frac{d^2s}{dz^2}$	
	at z_1	at z_4
20	.0334748 + \hat{i} .1950647	.0334896 - \hat{i} .1950764
30	-.0104412 + \hat{i} .3630329	-.0104454 + \hat{i} .3630360
40	-.0130508 + \hat{i} .3540384	-.0130544 + \hat{i} .3540325
50	-.0127189 + \hat{i} .3543001	-.0127227 + \hat{i} .3543057
60	-.0127367 + \hat{i} .3543040	-.0127329 + \hat{i} .3542970
70	-.0127369 + \hat{i} .3543036	-.0127324 + \hat{i} .3542953
80	-.0127373 + \hat{i} .3543042	-.0127316 + \hat{i} .3542948
90	-.0127376 + \hat{i} .3543045	-.0127306 + \hat{i} .3542936
100	-.0127376 + \hat{i} .3543050	-.0127300 + \hat{i} .3542927

tends to make the differential equation (6.9) ill-conditioned. Even when we took the precaution of making the four points s_k exactly symmetric, an unsymmetry in the results remained.

Similarly, the reverse expansion for a rectangle of any ratio h/b can be found, but the number of series will depend on the ratio. Generally a single Taylor series is not possible. But for very flat rectangles, the mapping on the circle becomes a problem as the angle ϕ_1 becomes rapidly very small.

While the reverse mapping function over the whole rectangle by a set of Taylor series has been shown above, this method should be compared to other expansions. Such are obtained by posing the equation

$$w = \log s = \log z + f(z),$$

and solving $f(z)$ by the real boundary value problem

$$u(x, y) = \log r + g(x, y),$$

where $w = u + \hat{i}v$, $\log z = \log r + \hat{i}\phi$, $f(z) = g(x, y) + \hat{i}h(x, y)$. We would like to point out here that the method of polynomials, orthogonalized on the boundary, does not work, because of the ill-conditioned matrices that occur, see [4]. We have solved a similar problem with a mere ratio of $b/h = 2$ on an Olivetti Programma with 22 digits. Using powers up to z^{10} , we obtained an accuracy of 3 decimals. But an attempt do do the mapping problem on a modern PC with 7 digits, for the same ratio of b/h , failed completely, as it must when one attempts to represent a diverging Taylor series by a polynomial. In some classic examples, see [45,46], not very elongated shapes were used, 10 to 12 decimals were employed, and accuracy of 3 decimals was obtained. Convergence with orthogonal polynomials is proved, see also [4], but the divergence problem lies in the expression of orthogonal polynomials by Taylor polynomials. For example, the computation of the values of Tchebychef polynomials $T_n(z)$, expressed as Taylor polynomials, fails on a 7-digit computer already at $n > 20$, near $|z| = 1$. But using the recursion formula for the values of T_n , starting with $T_0 = 1$, $T_1 = z$, no such problem occurs even for n well over 100.

A satisfactory method is expansion in Fourier series, a method that is used for the classic rectangle torsion problem, see [47], with the result of the form

$$\log s = \log z + c + \sum_{n=1}^{\infty} a_n \sin \frac{2\pi n}{b} z + \sum_{n=1}^{\infty} b_n \text{Sinh} \frac{2\pi n}{h} z, \tag{6.14}$$

where the coefficients are transcendental numbers. This series converges over the whole rectangle; it differs from the Fourier series given in [21] for $\text{sn}(\zeta)$, which maps the rectangle on the upper half on the t -plane, and which does not converge over the whole rectangle because of the singularity $\zeta = \hat{i}K'$.

The reverse solution can be obtained also if a polygon consists of rectangular subregions, joined at one rectangle side. The required function, either $s(z)$ or $w(z)$, can be expressed as Fourier series similar to equation (8.14), and matched at the joints to get an analytically continuous solution. This approach has been applied by Kim and Eom [48]. From their Figure 2, however, it is obvious that their functions do not match. The Fourier series will converge badly if singularities appear at the corners, and the derivative then becomes useless, especially if the derivative is theoretically infinite.

6.6. Frobenius Series

The half-infinite strip in Figure 6.4 is used as an example of the different kinds of reverse series at singularities. The data for the z - and s -planes are: As far as the SCT is concerned, the strip

Corner	z	a	ϕ
1	1	110°	0°
2	0	70°	20°
3	∞	180°	100°

is a generalized triangle.

The function $\log s$ is plotted inside the strip, and in Figure 6.5, the same lines are shown in the s -plane for the purpose of visually tracing the mapping of any particular point.

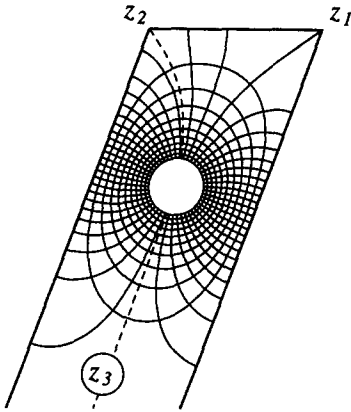


Figure 6.4. $\log s$ in strip in z -plane.

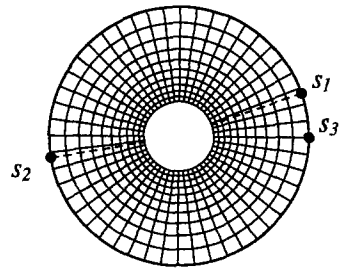


Figure 6.5. $\log s$ in s -plane.

Rather than using the general notation, we choose a problem-specific notation, for simplicity, in this example. Let a , b , and c be the notation of successive corners, with turning angles α , β , and γ in multiples of π , where a is the corner about which the reverse expansion is developed. Including the constant factor, the SCT of equation (6.1) becomes

$$\frac{dz}{ds} = c_2 (s - s_a)^{-\alpha} (s - s_b)^{-\beta} (s - s_c)^{-\gamma}. \quad (6.15)$$

Transforming the variable and constants

$$u = \frac{s - s_a}{\rho}, \quad u_b = \frac{s_b - s_a}{\rho}, \quad u_c = \frac{s_c - s_a}{\rho}, \quad (6.16)$$

equation (6.15) is transformed to

$$\frac{dz}{du} = c_2 \frac{1}{\rho} u^{-\alpha} (u - u_b)^{-\beta} (u - u_c)^{-\gamma}, \quad (6.17)$$

where the condition $\alpha + \beta + \gamma = 2$ has been used. The scaling constant ρ is equal to the numerical radius of convergence about s_a .

ORDINARY FROBENIUS SERIES. The forward Frobenius expansion about corners 1 and 2 has the form, according to equation (2.23), and including the integration constant c_1 and scaling constant c_2 ,

$$z = c_1 + c_2 (z_0 + u^{1-\alpha}(z_{F0} + z_{F1}u + \dots)). \quad (6.18)$$

The point s_a is mapped on the cornerpoint z_a such that

$$z_a = c_1 + c_2 z_0, \quad (6.19)$$

and we write equation (6.18) as

$$\begin{aligned} \frac{z - z_a}{c_2} &= u^{1-\alpha}(z_{F0} + z_{F1}u + \dots) \\ &= u^{1-\alpha} \times \underline{U} \cdot \overline{z}_F. \end{aligned} \quad (6.20)$$

We define the variable

$$v = \left(\frac{z - z_a}{c_2} \right)^{1/(1-\alpha)}, \quad (6.21)$$

so that equation (6.20) is transformed to

$$\begin{aligned} v &= u \times \underline{U} \cdot \overline{z}_F^{*1/(1-\alpha)} \\ &= u \times \left(z_{F0}^{1/(1-\alpha)} + \dots u + \dots u^2 + \dots \right). \end{aligned} \quad (6.22)$$

Equation (6.22) is regular in both variables u and v and is therefore suitable for reversion. Obviously the leading part of the expansion in equation (6.18), $c_1 + c_2(z_0 + u^{1-\alpha}z_{F0})$, plays a major role, and we call it the principal part (PP).

Equation (6.21) defines a mapping from the z -plane on a v -plane, different for each corner. The mapping at corner 1 is shown in Figure 6.6a, and at corner 2 in Figure 6.6b. The mapped center of the s -plane is shown by a \bullet inside the boundary. The reflection of this point by the straight line is shown by a \bullet outside the boundary. As this latter point is the mapping of the reflection of $s = 0$ in the s -plane by the unit circle, which is ∞ , it is a singularity of the mapping function $s(v)$. The mapped lines of the function $\log s$ show clearly that $s(v)$ is a regular function within the boundaries, and is continued regularly in the reflection about the straight line boundary. The mapped corner 2 in Figure 6.6a, the mapped corner 1 in Figure 6.6b, and the mapped infinity point are singularities which limit the radius of convergence.

The numerical radius of convergence about each center is shown as determined in the v -plane. In Figure 6.6a, the radius is limited by the corner 2, but in Figure 6.6b, the infinity point is the one that limits the radius of convergence.

The purpose of equation (6.22) is only to arrive at suitably transformed variables. The reversion of a truncated Taylor series is not exact, and needs as at least twice as many convolution variables as there are forward coefficients, see [20]. The actual reversion is carried out by solving the differential equation derived from equations (6.17) and (6.21),

$$\frac{du}{dv} = (1 - \alpha)\rho \left(\frac{u}{v} \right)^\alpha (u - u_b)^\beta (u - u_c)^\gamma. \quad (6.23)$$

In the reverse expansion, u is considered as function of v ,

$$u = \underline{V} \cdot \overline{u}; \quad (6.24)$$

therefore the Taylor transform of equation (6.23) is

$$\overline{u}' = (1 - \alpha)\rho \times \left(\frac{\overline{u}}{\delta_1} \right)^{* \alpha} * \left(\overline{u} - \overline{u}_b \right)^{* \beta} * \left(\overline{u} - \overline{u}_c \right)^{* \gamma}, \quad (6.25)$$

which has to be solved for the convolution number \overline{u} .

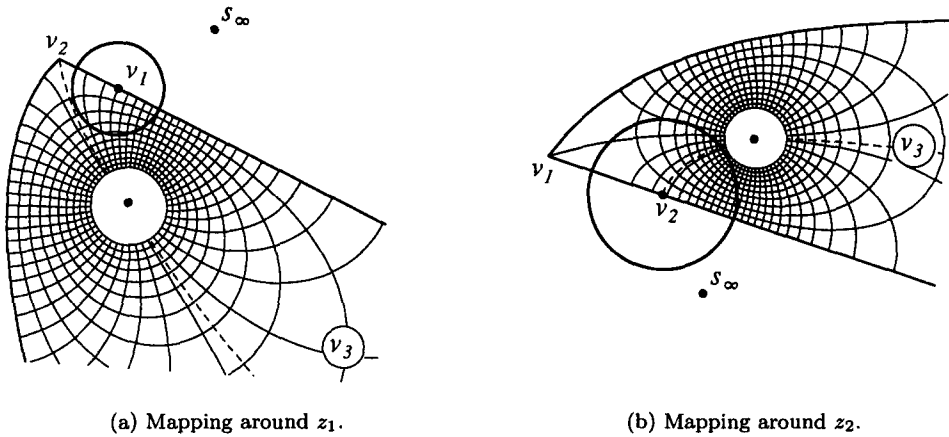


Figure 6.6. $\log s$ in v -planes.

Equation (6.25) is free of the constants c_1 and c_2 , but they are still necessary for the relation between z and v in equation (6.21). Therefore, the forward SCT solution must be obtained first. Only in this example of a triangle, no iteration is required.

To solve equation (6.25), we define intermediate variables shown graphically in equation (6.26) below:

$$\overline{u}' = (1 - \alpha)\rho \times \underbrace{\left(\frac{\overline{u}}{\overline{\delta}_1}\right)^{\alpha}}_{\overline{r}_a} * \underbrace{\left(\overline{u} - \overline{u}_b\right)^{\beta}}_{\overline{r}_b} * \underbrace{\left(\overline{u} - \overline{u}_c\right)^{\gamma}}_{\overline{r}_c} \tag{6.26}$$

$\underbrace{\qquad\qquad\qquad}_{\overline{u}_a}$
 $\underbrace{\qquad\qquad\qquad}_{\overline{q}_1}$
 $\underbrace{\qquad\qquad\qquad}_{\overline{q}_2}$
 $\underbrace{\qquad\qquad\qquad}_{\overline{p}}$

From equation (6.22), it is clear that the reversed series in equation (6.24) is a nonunit,

$$u_0 = 0, \tag{6.27}$$

so that equation (6.24) is in detail

$$u = u_1v + u_2v^2 + u_3v^3 + \dots \tag{6.28}$$

From this property, it follows that the division $\overline{u}/\overline{\delta}_1$ in equation (6.26) is compatible. But it also implies that the shift of elements of convolution numbers on both sides of equation (6.26) is the same, on the left due to the differentiation, on the right due to the division. We cannot employ directly the pointer number method, because the unknown element of \overline{u} is the same in \overline{u}' and in \overline{p} . Therefore we use the advance pointer method, see [20]. We define a function

$$\overline{f} = \overline{p} - \overline{u}' \tag{6.29}$$

which must be zero. To follow the theory clearly, a few algebraic steps are shown in detail. Let

$$(1 - \alpha)\rho(u - u_b)^\beta(u - u_c)^\gamma = a_0 + a_1u + a_2u^2 + \dots \tag{6.30}$$

Substituting equation (6.28) and (6.30) into equation (6.23) produces the first elements

$$f_0 = a_0 u_1^\alpha - u_1, \tag{6.31a}$$

$$f_1 = a_1 u_1^{\alpha+1} + a_0 \alpha u_1^{\alpha-1} u_2 - 2u_2, \tag{6.31b}$$

$$f_2 = a_2 u_1^{\alpha+2} + a_1 u_2 u_1^\alpha + \alpha a_1 u_1^\alpha u_2 + a_0 \frac{\alpha(\alpha-1)}{2} u_1^{\alpha-2} u_2^2 + a_0 \alpha u_1^{\alpha-1} u_3 - 3u_3, \tag{6.31c}$$

⋮

Consider equation (6.29) as implicit first-order differential equation $\overline{f}(\overline{u}, \overline{u}') = 0$. Equation (6.27) constitutes the necessary initial condition for a first-order differential equation. From the theory of [20, Section 13], we use the following results.

The first unknown element of \overline{u} is solved from the element f_0 , with the solution

$$u_1 = a_0^{1/(1-\alpha)}. \tag{6.32}$$

The element f_k does not contain elements $u_{i>k+1}$.

The element f_k contains element u_{k+1} linearly. Therefore we can express

$$f_k = f_k(u_0, u_1, u_2, \dots, u_k, 0) + \frac{\partial f_k}{\partial u_{k+1}} u_{k+1}. \tag{6.33}$$

From equation (6.31),

$$\frac{\partial f_k}{\partial u_{k+1}} = \frac{\partial p_k}{\partial u_{k+1}} - (k+1). \tag{6.34}$$

From the theory in [20, Section 10], applied to equation (6.29), and using the solution equation (6.31a),

$$\frac{\partial p_k}{\partial u_{k+1}} = \frac{\partial p_0}{\partial u_1} = \alpha. \tag{6.35}$$

From equation (6.29) it is clear that f_k on the r.h.s. of equation (6.33) can be replaced by p_k as defined in equation (6.26). The formula for the new element in the recursion routine is therefore

$$u_{k+1} = -\frac{p_k(u_0, u_1, \dots, u_k, 0)}{\alpha - (k+1)}. \tag{6.36}$$

Equations (6.34)–(6.36) can be verified from equations (6.31a)–(6.31c).

From equation (6.30) we find

$$a_0 = (1 - \alpha) \rho u_1^\alpha (-u_b)^\beta (-u_c)^\gamma, \tag{6.37}$$

and it can be verified numerically by using equations (6.20), (6.21), (6.30), and (6.23) that this is the same as

$$a_0 = \frac{1}{z_{F0}}.$$

Pointer convolution number algebra is used to determine the value of $p_k(u_0, u_1, \dots, u_k, 0)$ in a computation loop, using all the intermediate variables indicated in equation (6.26). Initial values are set for u_1 , $u_{a0} = u_1^\alpha$, $u_{b0} = (-u_b)^\beta$, $u_{c0} = (-u_c)^\gamma$, which sets the proper pointer to $p = 0$. The advance number is $a = 1$, and the pointer in \overline{u} is set to $p + 1$ at the beginning of each loop. This allows p_k to be computed without element u_{k+1} with the standard pointer routines. At the end of the loop, the element p_k is recalled, element u_{k+1} computed according to equation (6.36)

and inserted in \bar{u} . The pointer of all dependent variables is now reset to p by subtracting 1 from the current value of p .

Care must be taken to choose the branch in the solution of the multivalued function in equation (6.32) so that the result satisfies equation (6.31a) with the branch chosen there for u_1^α .

Each exponent in the loop is computed by an functional routine. Generally for $\bar{f} = \bar{u}^{*e}$, a pointer routine is written to solve the differential equation

$$\bar{f}' = e \times \bar{f} * \frac{\bar{u}'}{\bar{u}}.$$

This routine is used as a subroutine for two reasons. First, it needs only to be written once for the three exponents in the main routine. But second, for each main loop the subroutine needs two loops, which would hold up the main routine if it were directly included.

The solution of equation (6.25) is carried out for cornerpoint 1, with the indices a , b , and c , and the values of the exponents α , β , and γ referring to corners 1, 2, and 3, respectively. Since the constants c_1 , c_2 and cornerpoints in all planes are assumed to be known from the forward solution, no matching is required.

The same equations apply to every corner which has a forward Frobenius series of the form of equation (6.18). Therefore, for cornerpoint 2, the indices a , b , and c , and the values of the exponents α , β , and γ refer to corners 2, 3, and 1, respectively.

FROBENIUS SERIES WITH LEADING LOGARITHMIC TERM. The forward Frobenius expansion from equation (6.23) about corner 3 has a logarithmic term according to equation (2.27),

$$z = c_1 + c_2 \left(z_0 + g_{0F} \log u + \underline{U} \cdot \bar{z}_F \right). \quad (6.38)$$

Defining z_a as in equation (6.19), it follows that

$$\frac{z - z_a}{c_2 g_{0F}} = \log u + \underline{U} \cdot \frac{\bar{z}_F}{g_{0F}} \equiv \underline{U} \cdot \bar{a}. \quad (6.39)$$

Define now the variable

$$v = e^{(z - z_a)/(c_2 g_{0F})}, \quad (6.40)$$

then

$$\begin{aligned} v &= u \times \underline{U} \cdot e^{\bar{a}} \equiv \underline{U} \cdot \bar{b} \\ &= b_1 u + b_2 u^2 + \dots, \end{aligned} \quad (6.41)$$

which is a regular nonunit Taylor series. The reverse has therefore the same form as equations (6.24) and (6.28). Equation (6.40) represents a mapping of the z -plane on a v -plane shown in Figure 6.7a. At the corners 1 and 2, $u(v)$ has singularities. The central part is shown enlarged in Figure 6.7b, with the center $s = 0$ and its reflection on the straight line, representing $s = \infty$. This latter point is the singularity nearest to the origin and therefore determines the numerical radius of convergence, shown by the circle in Figure 6.7b.

Substitute now a , b , and c as indices and α , β , and γ as exponents at corners 3, 2, and 1, respectively, then from equation (6.17), and using the derivative of equation (6.40), we obtain the differential equation

$$\frac{du}{dv} = g_{0F} \rho \frac{u}{v} (u - u_b)^\beta (u - u_c)^\gamma \quad (6.42)$$

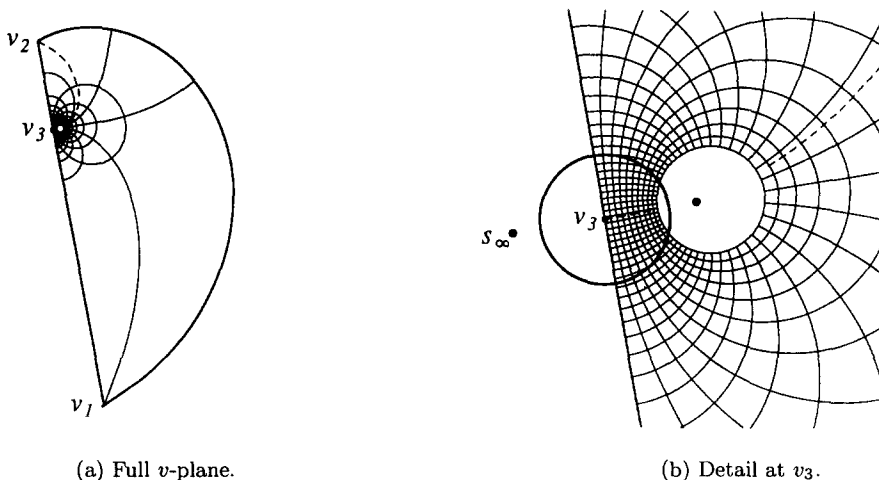


Figure 6.7. $\log s$ in v -plane at z_3 .

and the Taylor transform

$$\bar{u}' = g_{0F\rho} \times \left(\frac{\bar{u}}{\delta_1} \right) * (\bar{u} - \bar{u}_b)^{* \beta} * (\bar{u} - \bar{u}_c)^{* \gamma}. \tag{6.43}$$

Equations (6.42) and (6.43) have the same form as equations (6.23) and (6.25), considering that $\alpha = 1$, and are therefore solved with the same advance pointer convolution number technique. The constant $a_0 = 1$, and $u_1 = 1$, so that equation (6.31a) is again satisfied.

REVERSION OF THE WHOLE POLYGON. The mapped regions of convergence about the corners in the z -plane are shown in Figure 6.8. The circles of the v -plane of corners 1 and 2 become circular segments, and the circle of the v -plane of corner 3 becomes the straight line. There is yet an uncovered region in the middle. This can be covered by a Taylor series in the z -plane. Choosing the center at a point z_k , the radius of convergence is limited in the z -plane by the reflection of $s = 0$ on both straight sides of the strip, so that the Taylor series is valid in the circle as shown in Figure 6.8.

The forward transformation is

$$z = c_1 + c_2 (z_0 + z_1 u + z_2 u^2 + \dots). \tag{6.44}$$

Let $z_k = c_1 + c_2 z_0$ and transform again to the new variable

$$v = \frac{z - z_k}{c_2}, \tag{6.45}$$

then the reverse expansion $u = \underline{V} \cdot \bar{u}$ is obtained from the differential equation

$$\bar{u}' = \rho (\bar{u} - \bar{u}_a)^{* \alpha} (\bar{u} - \bar{u}_a)^{* \beta} (\bar{u} - \bar{u}_a)^{* \gamma}, \tag{6.46}$$

which is solved by normal pointer convolution number algebra. We can assume that the forward expansion around z_k is not available because the point z_k was chosen in the z -plane. Therefore, we find the corresponding point s_k by iteration from the other available forward expansions, assuming that the whole unit disk in the s -plane was covered. With this information, we determine ρ as the numerical radius of convergence in the s -plane, to transform to the variable

$$u = \frac{s - s_k}{\rho}. \tag{6.47}$$

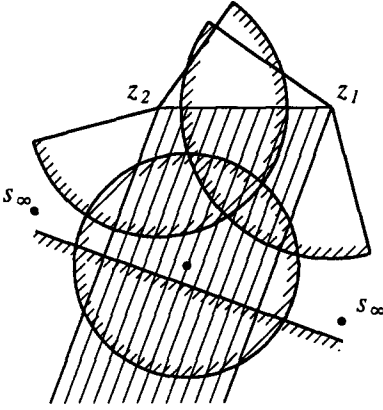


Figure 6.8. Convergence regions in z-plane.

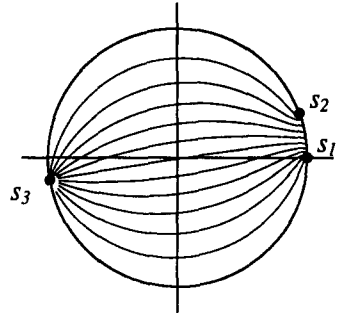


Figure 6.9. z-lines mapped on s-plane.

In Figure 6.8 we have also shown a set of parallel straight lines to be used as visual display for the reverse mapping $s(z)$. These mapped lines are shown in the s -plane in Figure 6.9, using the solutions in the appropriate convergence disks, using convolution number length $n = 20$.

As a check, we also reversed the Taylor series of equation (6.44) directly according to the method in [20, Section 20.2], using only the first five coefficients of \bar{z}_F . The result was that the first five coefficients of \bar{u} by both methods agreed quite well, the first coefficient being the same. Note that the reversion of a truncated Taylor series only approximates each coefficient, while the reverse solution form the differential equation gives a machine-exact result of each coefficient.

In this example, we have not considered the reflection of the center $s = 0$ on the curved boundaries in the different v -planes, nor on the straight line 1-2 in the z -plane, because they are too far away to limit the radius of convergence. But with other geometries this may not be the case. Generally in every reverse problem all reflections may have to be considered.

FROBENIUS SERIES WITH FIRST TERM A LOGARITHMIC SERIES. The first term of the Frobenius series will be a logarithmic series when the turning angle at infinity is near π , according to equation (2.26). Let the cornerpoint be z_1 and the turning angle $a_1 = 1 + \delta$, as shown in Figure 6.10a. The data for the SCT are:

Corner	z	a	ϕ
1	∞	190°	0°
2	$\approx \hat{i} \pi$	80°	120°
3	0	90°	240°

The slope of the wedge shape is 10° for this demonstration example. A logarithmic series will actually be used only for much smaller angles, typically $< 1^\circ$. The mapped lines of concentric circles in the s -plane are plotted to convey the mapping visually, the mapped position of the center of the circle, $s = 0$, is shown by a \bullet .

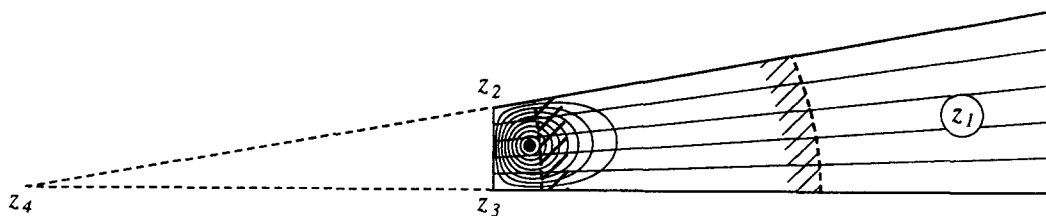
The point 4 is chosen as $z_4 = 1/\delta$. The point z_2 becomes then $z_2 = \hat{i}(1/\delta) \tan(\delta\pi) \approx \hat{i} \pi$. The SCT is

$$\frac{dz}{du} = c_2 u^{-(1+\delta)} (u - u_2)^{-\beta} (u - u_3)^{-\gamma}, \tag{6.48}$$

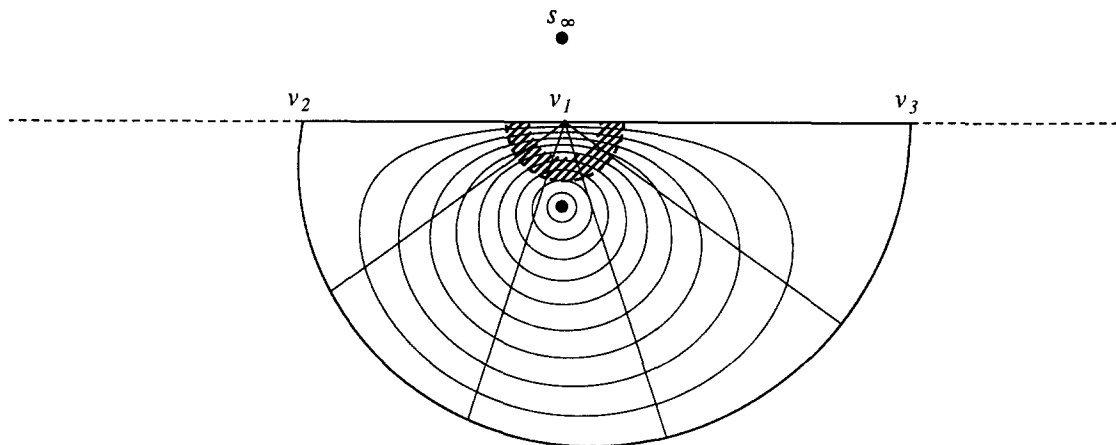
and the integral has the form

$$z = a_1 \log u + a_2 \log^2 u + a_3 \log^3 u + \dots + \underline{U} \cdot \bar{f}. \tag{6.49}$$

The PP is the logarithmic series, which maps the circle boundary through s_1 into the two half-infinite straight lines at z_1 . Therefore, the transformation of the z -region near z_1 on the lower half v -plane is will be the reverse of the logarithmic series, which is a Taylor series in the variable



(a) Narrow-angle polygon in the z -plane.



(b) Narrow-angle polygon mapped on the v -plane.

Figure 6.10.

$\log u$, of which the reverse exists. The reverse is obtained directly by mapping of the region between the straight lines on the lower half of the v -plane by

$$v = (1 + \delta z)^{-1/\delta}, \tag{6.50}$$

which has the derivative

$$\frac{dv}{dz} = -v^{1+\delta}. \tag{6.51}$$

The straight lines shown in Figure 6.10a are mapped on straight lines in the v -plane by this transformation.

Equation (6.50) is ill-determined for small δ , and therefore expanded into the well-determined form, similar to equation (2.26),

$$v = e^{-z + (1/2)\delta z^2 - (1/3)\delta^2 z^3 + \dots} \tag{6.52}$$

which is valid for small $\delta \rightarrow 0$, and becomes equation (6.40) for $\delta = 0$. The mapped region in the v -plane is shown in Figure 6.10b. The reverse SCT for $u(v)$ is obtained from equation (6.48) and the analytical closed form derivative in equation (6.51),

$$\frac{du}{dv} = \frac{-1}{c_2} \left(\frac{u}{v}\right)^{1+\delta} (u - u_2)^\beta (u - u_3)^\gamma. \tag{6.53}$$

This is of the same form as equation (6.25), and the solution is obtained by the same convolution number method in equations (6.26)–(6.36).

The radius of convergence of the reverse series is determined entirely by the singularities of $u(v)$ in the v -plane. The smallest radius in this example is determined by s_∞ , which is the reflection of the mapping of point $s = 0$ in the v -axis. The corresponding convergence region is shown by the hatched side of the dotted line in the v -plane, and its mapped region in the z -plane, the hatched

side (to the right) of the left dotted line in Figure 6.10a. However, the numerical convergence of the series in equation (6.52) is limited to $z < 0.7|z_4| = 0.7/\delta$, which affects the computation of $v(z)$ in the reverse calculation. This region is shown by the hatched side (to the left) of the right dotted line in the z -plane in Figure 6.10a. For small δ , this is a large number, which may be sufficient for practical purposes in view of the transformed value of v , and u being close to 0. But this is still an unsatisfactory situation in as much values of z as large as a computer allows, should be able to be transformed. We conclude that this is not possible by an explicit method. The only method we can find to transform values of $z > 0.7/\delta$ is to use the PP as a function $z(v)$ and then solve $v(z)$ iteratively. In this example the expansion is given by

$$\begin{aligned} z &= \frac{e^{-\delta \log v} - 1}{\delta} \\ &= -\log v + \frac{1}{2}\delta \log^2 v - \frac{1}{3!}\delta^2 \log^3 v + \dots, \end{aligned} \quad (6.54)$$

which has unlimited radius of convergence in the v -plane.

FROBENIUS SERIES WITH SECOND TERM LOGARITHMIC. As example, we use the flow along a step in a wall shown in Figure 6.11a. The data for the z - and s -planes are:

Corner	z	a	ϕ
1	∞	360°	0°
2	$\hat{i}\pi$	-90°	120°
3	0	90°	240°

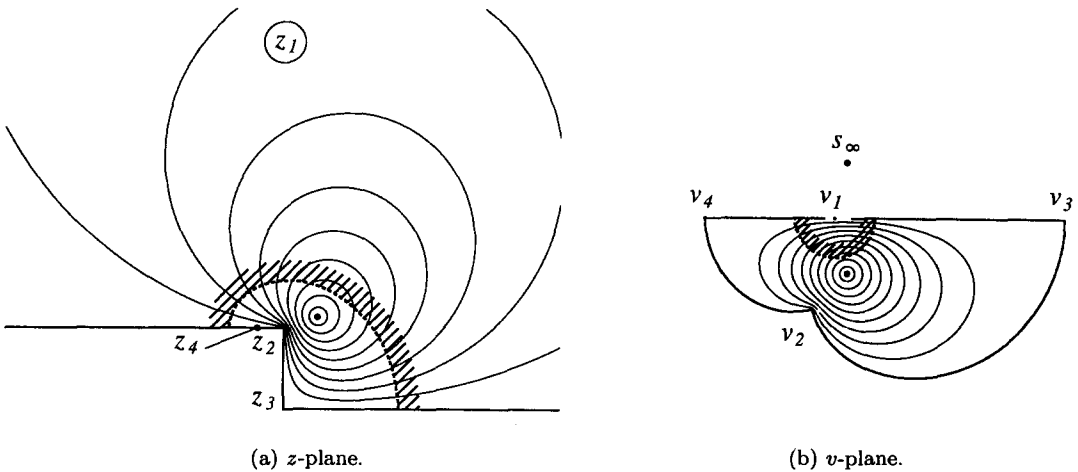


Figure 6.11. Mapping of step in wall.

The corner at infinity is the point z_1 . The SCT according to equation (6.1) becomes for this case

$$\frac{dz}{du} = c_2 u^{-2} (u - u_2)^{1/2} (u - u_3)^{-1/2} \quad (6.55)$$

with the usual transformed variable u according to equation (6.3). The Frobenius expansion around point 1 is, according to equation (2.27),

$$z = c_1 + c_2 (z_0 + z_{F0} u^{-1} + z_{F1} \log u + z_{F2} u + z_{F3} u^2 + \dots). \quad (6.56)$$

The PP of the series in equation (6.56) is $z_{F0} u^{-1} + z_{F1} \log u$, which is the part that transforms the regular circle boundary through point s_1 into the two half-infinite straight lines in the z -plane,

where the logarithmic term corresponds to the parallel offset of the straight lines. Unlike the ordinary case, we do not have a simple explicit reversion of the PP to transform the boundary near point z_1 of the z -plane into a straight line of the v -plane similar to Figure 6.7a. The best we can do is to use the PP as implicit function to transform the z -plane into the v -plane by

$$z = \frac{1}{v} - \log v. \tag{6.57}$$

The mapped flow in the v -plane is shown in Figure 6.11b. The corners z_2 and z_3 are mapped conformally into corners v_2 and v_3 , but the transformation has a singularity at a point z_4 , $z = -1 + \hat{i}\pi$, causing the corner at v_4 , $v = -1$.

Using equations (6.55) and (6.57), the reverse SCT becomes

$$\frac{dv}{du} = -c_2 \left(\frac{u}{v}\right)^2 \frac{(u - u_2)^{-1/2}(u - u_3)^{1/2}}{(1 + v)}. \tag{6.58}$$

Near $v = 0$ the reverse function $u(v)$ is regular and can be expanded in a nonunit Taylor series as in equation (6.5). The Taylor transform of equation (6.58) is then

$$\overline{u}' = -c_2 \left(\frac{\overline{u}}{\overline{\delta}_1}\right)^{*2} * (\overline{u} - u_2)^{* -1/2} * \frac{(\overline{u} - u_3)^{*1/2}}{(1 + \overline{\delta}_1)}. \tag{6.59}$$

The convolution division inside the term $(\overline{u}/\overline{\delta}_1)^{*2}$ is again compatible. The division by $1 + \overline{\delta}_1$ causes the limit $|v| < 1$ of the Taylor series, corresponding to the contraformal point v_4 . The mapping of the center of the circle, $s = 0$, is shown by a \bullet in the z -plane in Figure 6.11a and in the s -plane in Figure 6.11b. The reflection of this point in the real v -axis, marked s_∞ , is the singularity of the function $u(v)$ where $s = \infty$ and therefore $u = \infty$. Therefore, the numerical radius of convergence in the v -plane is determined by the lesser of distances of -1 and s_∞ in the v -plane, from which the radius of the Taylor disk is determined as indicated by the dotted line in Figure 6.11b. The corresponding region that is covered in the z -plane is shown in Figure 6.11a as the hatched side of the dotted line.

The convolution number solution of equation (6.59) proceeds as in the previous example, by the sequence of equations (6.26)–(6.36).

The result is that the complete reversion $s(z)$ includes the iterative solution of $v(z)$ from equation (6.57), and therefore the purpose of reversion, to obtain an explicit function $s(z)$, is in this case only partially achieved.

CONCLUSION. The reverse of a Frobenius series is an ordinary Taylor series in a transformed variable. The Principal Part, PP, of the Frobenius series is the term that transforms the regular circle boundary through the cornerpoint point s_a into the two straight lines from the corner z_a in the z -plane. The reverse of the PP transforms this corner in the z -plane into a straight line in the v -plane, which has then a suitable region around the transformed point v_a for the reverse Taylor series. The PP can be reversed explicitly in the ordinary case, or iteratively in cases containing the logarithm or a logarithmic series after the first term.

The reverse of a Frobenius series is not a Frobenius series. If there was only one term in the SCT, the forward and the reverse would be of the same form. But the forward expression has a “tail” after the first term, which makes the forward and reverse forms different.

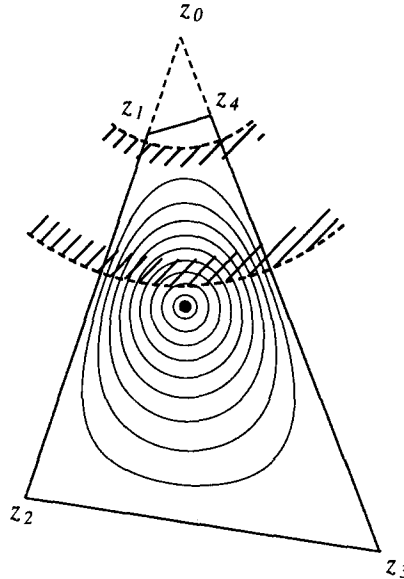
6.7. Laurent Series

For the reverse series solution, the Laurent expansion is just as important as in the forward series, i.e., it would need in some cases too many small Taylor disks to cover the region in the z -plane.

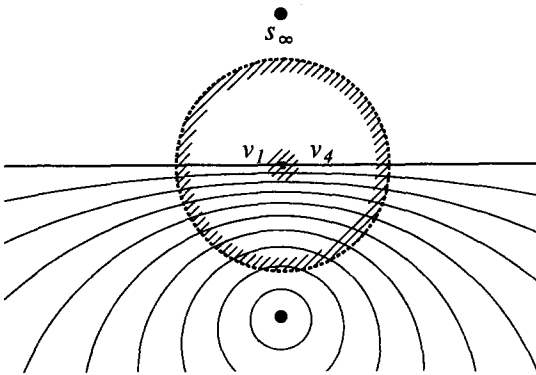
An example is shown in Figure 6.12a with the following data:

Corner	z	a	ϕ
1	$-.1338645 - \hat{i}.3688462$	55°	1.667607°
2	$-.6395838 - \hat{i}1.762290$	100°	165.0755°
3	$.7258552 - \hat{i}2.000000$	120°	194.9246°
4	$.1100924 - \hat{i}.3033454$	85°	358.3324°

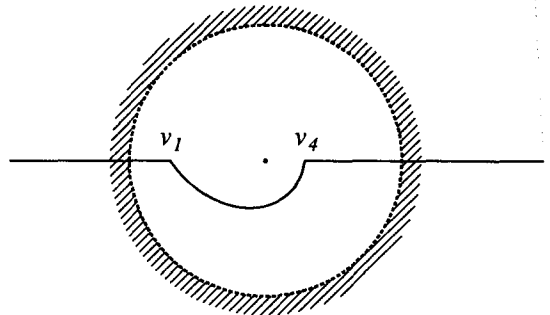
Two straight line segments of the polygon are to be mapped on a single straight line in the v -plane, shown in Figure 6.12b. The transformation $v(z)$ may be explicit or implicit by the same method as described for the reverse of Frobenius series before. In this case, the straight lines meet in a point $z_0 = 0$, and the transformation is explicit, $v = (.720 - \hat{i}.694)z^{4.5}$. The mapped concentric circles of the s -plane are shown in Figure 6.12a to visualize the mapping.



(a) Quadrilateral in z -plane.



(b) Laurent annulus in v -plane.



(c) Inner Laurent circle in v -plane.

Figure 6.12. Quadrilateral for reverse Laurent series.

The part of the v -plane that includes the s_∞ point is shown in Figure 6.12b, with the Laurent outer radius limited by the point s_∞ , which is the reflection of the center $s = 0$, as shown. Figure 6.12c is enlarged by a factor of 50 to show how the inner Laurent radius is limited by the included corners at v_1 and v_4 . The full annulus of the v -plane is shown as the sector in the z -plane Figure 6.12a.

The function $s(v)$ is analytic in the annulus, and therefore a regular Laurent series of the reverse $s(v)$ exists.

However, we have no Laurent convolution number algebra available to solve the differential equation of the reverse SCT. The only method we can suggest is to calculate the values of $z(v)$ at a number of points on the two circles, iteratively from the forward solution, and then to calculate the Laurent coefficients by a discrete Fourier analysis on both circles. A large number of points must be used to minimize aliasing.

6.8. Conclusion

We have described how the reverse SCT of any polygon can be solved by Taylor series analytically and Laurent series numerically. As in the forward transformation, a separate series for each corner is required, but a transformation to a new variable $v(z)$ must be made first. The reverse series at the corners are regular series of the transformed variable, not Frobenius series as in the forward solution. Additional Taylor series may be necessary to cover the complete polygon. The reverse of the rectangle can be covered by Taylor series only.

Except for the rectangle, the reverse solution is much more complicated than the forward for several reasons. First, the forward solution must in any case be obtained first to get the parameters. Second, the distribution of singular points that limit the convergence disks is more complicated. Third, at the corners a transformation of variable $v(z)$ must be made, for which in some cases we could not find an explicit form. Finally, a differential equation must be solved, which at the corners require a special pointer method. For the Laurent series only a discrete numerical solution could be found.

If one would attempt the solution of the parameter problem by the inverse SCT, the additional problem is that the position of the singularity $s(v) = \infty$ is not known, and therefore convergence disks are not known at the start of the problem. The solution of the forward SCT to find the parameters is therefore much simpler even if the reverse solution is actually sought.

The only remaining advantage of any reverse solution is that points $s(z)$ can be computed explicitly faster than from iteration of $z(s)$ by a factor of between 2 and 6. In any particular application, this advantage will have to be warranted compared to the large programming effort.

7. EXTERNAL POLYGON

7.1. General Solution

The SCT according to equations (4.1) and (4.3) maps the interior of the unit disk in the s -plane on the exterior region of a polygon, which we call the external polygon. It seems natural to rather map the exterior of a unit disk on the exterior of the polygon, and substitute the negative turning angles in Figure 5.1d by positive turning angles $\beta_i = -\alpha_i$. With the transformation

$$\zeta = \frac{1}{s} \quad (7.1)$$

we obtain a formula for the exterior mapping

$$z = \int \left(\frac{1}{\zeta} - \frac{1}{\zeta_{a1}} \right)^{\beta_1} \left(\frac{1}{\zeta} - \frac{1}{\zeta_{a2}} \right)^{\beta_2} \cdots \left(\frac{1}{\zeta} - \frac{1}{\zeta_{an}} \right)^{\beta_n} d\zeta. \quad (7.2)$$

The far exterior region is then mapped in a natural way by a half infinite Laurent series

$$z = \zeta + \frac{c_1}{\zeta} + \frac{c_2}{\zeta^2} + \cdots \quad (7.3)$$

of which the simplest example is the Joukowski transformation. If one deals only with exterior polygons, then the mapping of the exterior on the exterior according to the SCT of equation (7.2) is appropriate. Yet the Frobenius series about the singularities are still of the Taylor form, as well as any series of the filling disks. The Frobenius disks of the exterior SCT are not the same

as the Frobenius disks of the interior SCT, because although circles transform to circles by the inversion of equation (7.1), their centers do not transform to centers.

For the sake of uniformity of this treatise, we use the mapping of the interior disk in the s -plane also for the exterior polygon, and negative exterior angles as in Figure 5.1b. We also keep in mind that an exterior region is topologically still an interior region, with the result that the direction of the boundary of the exterior polygon is clockwise.

It has often been assumed that the center of the disk, $s = 0$, should be transformed to the infinity point in the z -plane, $z = \infty$, as in equation (4.1); see [34,35]. But this often leads to an undesirable distribution of points on the circle. Therefore, a more general form of equation (4.1) will be used, where the interior point $s = \hat{b}$ is mapped on $z = \infty$,

$$z = \int \left((s - \hat{b}) \left(1 - \frac{\hat{b}}{s} \right) \right)^{(1-m)/m} \prod (s - s_{ai})^{-\alpha_i} ds. \quad (7.4)$$

Equation (7.4) is obtained by a Möbius transformation of equation (4.1), and this form is invariant under Möbius transformation. Particularly for the external polygon, $n = -1$, equation (7.4) becomes

$$z = \int (s - \hat{b})^{-2} \left(1 - \frac{\hat{b}}{s} \right)^{-2} (s - s_{a1})^{-\alpha_1} (s - s_{a2})^{-\alpha_2} \cdots (s - s_{an})^{-\alpha_n} ds \quad (7.5)$$

$$\equiv \int g(s) ds, \quad (7.6)$$

which transforms the point \hat{b} inside the s -disk to $z = \infty$. Equations (7.4) and (7.5) are cast in a form that is suitable to include the case $\hat{b} = 0$. The natural form of the mapping as $z \rightarrow \infty$ is then done indirectly by a complex potential w according to the case of the problem, as in the two examples in this section. The form of equation (7.5) corresponds to the form given for the mapping of the half-plane on the exterior region in [28,35].

To obtain a mapping which is continuous at $z = \infty$, the residue of the expansion of $g(s)$ in equation (7.6) about \hat{b} must be zero, see [28], which is found to be

$$\sum \frac{\alpha_i}{s_{ai} - \hat{b}} + 2 \frac{\hat{b}}{1 - \hat{b}^2} \equiv r(\hat{b}) = 0, \quad (7.7)$$

where $b^2 = |\hat{b}|^2 = \hat{b} \hat{b}$. For any distribution of points on the circle, $s_{ai} = e^{\phi_i}$, which we call a constellation, let us denote the array of angles ϕ_i , arranged as $\phi_i < \phi_{i+1}$, by a vector $\overline{\phi}^n$. For any chosen constellation $\overline{\phi}^n$ of an exterior problem, we must solve equation (7.7) for \hat{b} . The condition equation (7.7), for the central form as in equation (4.1), is given by [28], but we could find no proof of the following hypothesis.

For every given constellation of $\overline{\phi}^n$, $n > 2$, and the condition $\sum \alpha_i = -2$, there is one and only one solution $s = \hat{b}$ of $r(\hat{b}) = 0$ in the disk, $|\hat{b}| < 1$.

The problem is that equation (7.7) is not an analytical function of the complex variable \hat{b} , and therefore the Shur-Cohn algorithm [35] cannot be applied directly.

The solution of equation (7.7) is done by the Newton-Raphson method, but is not always easy because of large variations of $|r(s)|$ for extreme polygons.

Since the inner point \hat{b} is mapped on $z = \infty$, it is also clear that an exterior polygon can have no positive corners ($\alpha_i > 0$) at infinity. Therefore *all polygons with positive infinity corners are interior polygons*. In view of this fact, it is interesting to note that *the only external SCT with 2 corners is the Joukowski transformation*. Negative infinity corners may appear, but these would be sheets that run through the enclosed interior region to overlap with the continuous exterior region.

There are now altogether $n + 2$ singular points, of which n are on the circle, one is the internal point \hat{b} , and one is its external reflection at $s = 1/\hat{b}$. On the boundary we need n Frobenius expansions, and another one Frobenius expansion in the interior of the s -disk. The external Frobenius series at $1/\hat{b}$ is never required, but the point has to be considered in limiting the radii of the other disks. Compared to the internal polygon, we have the additional factors, transforming to the scaled variable $u = (s - \hat{b})/\rho$, where ρ is taken as the radius of the disk,

$$(s - \hat{b})^{-2} \left(1 - \frac{\hat{x}}{\hat{b}} s\right)^{-2} = \underline{U} * \bar{g}_{n1} * \bar{g}_{n2} \tag{7.8}$$

in the Taylor series of $g(s)$ in equation (7.6). The one additional Frobenius series at point \hat{b} is

$$(s - \hat{b})^{-2} \left(1 - \frac{\hat{x}}{\hat{b}} s\right)^{-2} \prod (s - s_{ai})^{-\alpha_i} = u^{-2} \times \underline{U} * \bar{g}. \tag{7.9}$$

Due to the integral power, there is no discontinuity branchline out of this disk, subject to equation (7.7).

To demonstrate the effect of the eccentric point \hat{b} , an initial uniform constellation $\bar{\phi}^n$ of a typical 10-cornered external polygon is shown in Figure 7.1a. The internal Frobenius disk at \hat{b} and its external counterpart at $1/\hat{b}$ are shown. If the mapping of $s = 0$ on $z = \infty$ is used, the balanced constellation with \hat{b} is as shown in Figure 7.1b. Clearly this is an unfavorable distribution of points on the circle.

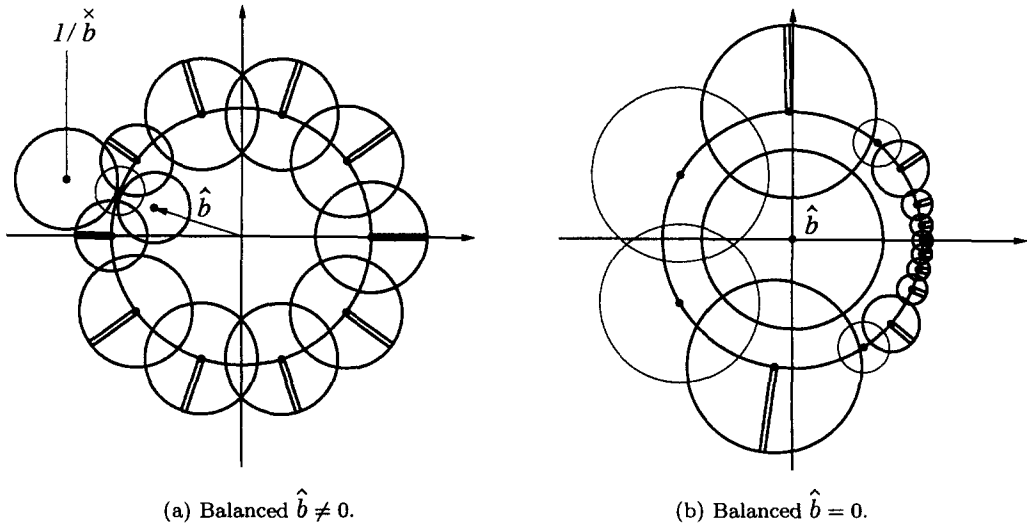


Figure 7.1. Boundary disks for the same external polygon.

The programming of the external polygon solution follows the same sequence as the internal solution. The tables of regions contain information of all $n + 2$ disks. The last row of the table is not complete because the expansion of the external series is not used.

7.2. Source and Uniform Flow

The complex potential w of the flow of a source or vortex in the z -plane is mapped on the s -plane by

$$w = h \log (s - \hat{b}) - h \log \left(\frac{\hat{x}}{\hat{b}} s - 1\right), \tag{7.10}$$

$$h = \frac{m}{2\pi} = \text{real for a source,}$$

$$h = \frac{-i\Gamma}{2\pi} = \text{imaginary for a vortex,}$$

of which an example is shown in Figure 7.2a.

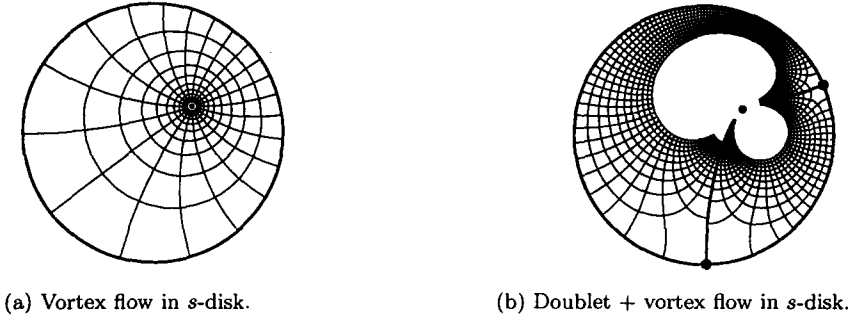


Figure 7.2

The complex potential w of the uniform flow with circulation in the z -plane is mapped on the s -plane as the sum of a doublet and a vortex,

$$w = \frac{-\hat{\mu}}{s - \hat{b}} - \frac{\check{\mu}}{1 - \frac{\check{x}}{b} s} + h \log(s - \hat{b}) - h \log\left(\frac{\check{x}}{b} s - 1\right), \quad (7.11)$$

of which an example is shown in Figure 7.2b.

Write equation (7.6) for a particular polygon formally as

$$z = f(s). \quad (7.12)$$

The central Frobenius expansion is, in terms of the variable u in the central disk,

$$f(u) = u^{-1} (f_0 + f_2 u^2 + f_3 u^3 + \dots) \quad (7.13)$$

$$= \frac{f_0}{u} + p(u), \quad (7.14)$$

where $p(u)$ is a perturbation series. The coefficient f_1 has been eliminated by the balancing equation (7.7).

The functions $w(z)$ and its inverse, $z(w)$, are given by equations (7.10)–(7.12), where the variable s actually performs only the role of a parameter.

SOURCE FLOW. To compute $z(w)$, equation (7.10) is solved explicitly for s , which is then substituted in equation (7.12) to obtain z . To compute $w(z)$, equation (7.12) is solved iteratively for s , in the appropriate convergence disk, then w is computed explicitly from equation (7.10). But the use of the internal region of the s -plane in the SCT causes this method of solution to be not well-determined at large z . As $z \rightarrow \infty$, $s \rightarrow \hat{b}$, and the value u is not very accurate, causing a large error in the leading term in equation (7.14). Let

$$q(w, s) \equiv \frac{w}{h} + \log\left(\frac{\check{x}}{b} s - 1\right), \quad (7.15)$$

then from equation (7.10)

$$\frac{1}{u} = \rho e^{-q}, \quad (7.16)$$

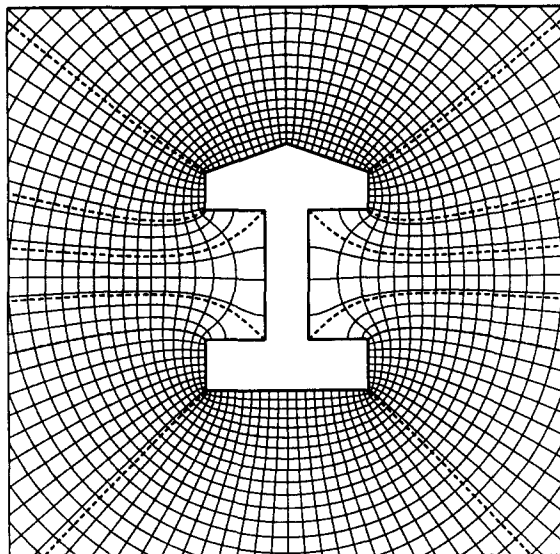
which we substitute in equation (7.14) to obtain

$$z = f(u) = \rho f_0 e^{-q} + p(u), \quad (7.17)$$

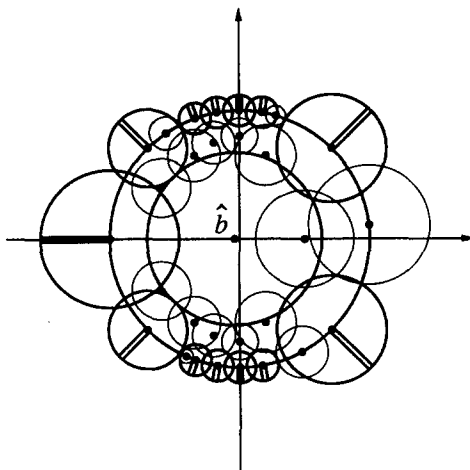
which is a well-determined form for the solution of $z(w)$ for large z , suitable in the whole central Frobenius disk. For the inverse solution $w(z)$, we substitute from equation (7.14) in equation (7.10) to obtain the well-determined form

$$w = h \log \frac{f_0}{z - p(u)} - h \log\left(\frac{\check{x}}{b} s - 1\right). \quad (7.18)$$

The source or vortex potential of an external polygon is shown in Figure 7.3a. This could be an electrostatic or magnetic field, or a coordinate grid for another problem. The convergence disks are shown in Figure 7.3b. Frobenius disks are shown in thick lines and Taylor disks in thin lines; there is no Laurent disk in this example. The external Frobenius disk is too far away to be shown.



(a) Source flow of external polygon.



(b) Convergence disks for (a).

Figure 7.3.

UNIFORM FLOW WITH CIRCULATION. For the computation of $z(w)$, we must solve equation (7.11) iteratively for s , which is the normal procedure in flow inside or outside a circle. Then s is substituted in equation (7.12). The inverse solution $z(w)$ starts again with the iterative solution of s from equation (7.12), then w is computed explicitly from equation (7.11). For large z , we substitute $1/(s - \hat{b}) = 1/\rho u$ from the leading term in equation (7.11) into equation (7.14) to obtain

$$z = \frac{-f_0 \rho}{\hat{\mu}} \left(w + \frac{\check{\mu}}{1 - \check{b} s} - h \log(\rho u) + h \log(\check{b} s - 1) \right) + p(u), \tag{7.19}$$

which is a well-determined form for the problem $z(w)$ in the central Frobenius disk. The term $\log(\rho u)$ is small compared to w .

For the inverse solution $w(z)$, we substitute the leading term in equation (7.11) by the leading term of equation (7.14) to obtain the well-determined form

$$w = -\hat{\mu} \frac{z - p(u)}{\rho f_0} - \frac{\check{\mu}}{1 - \check{b} s} + h \log \left(\frac{\rho f_0}{z - p(u)} \right) - h \log(\check{b} s - 1), \tag{7.20}$$

where s is again first found iteratively from equation (7.12).

From equations (7.18) and (7.20), it is clear that w and z are properly matched at $z \rightarrow \infty$. The fact that the point $s = 0$ is mapped on some finite point in the z -plane does not matter at all. What counts is that the singularity of $w(s)$ is situated at the point $s = \hat{b}$ which is mapped on $z = \infty$.

The flow over an external polygon is shown in Figures 7.4a and 7.4b. The circulation and direction of uniform flow has been adjusted in equation (7.11) by selecting particular corners

on the circle as leading and trailing stagnation points. The figures also show that overlapping regions may occur in external polygons. There may also be winding points, which are points with turning angle $-\alpha > \pi$. The discontinuity of the potential is not visible in the streamlines, and such a potential is only possible in pseudo-potential problems, like irrotational flow and magnetic fields.

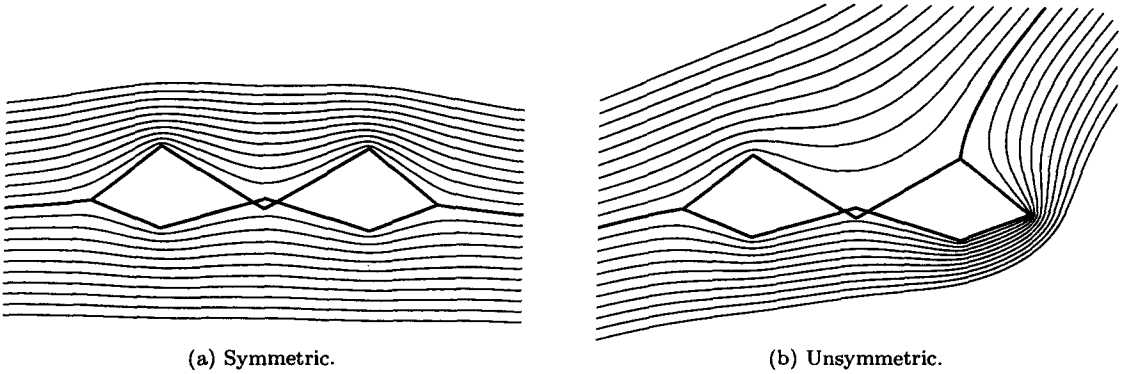


Figure 7.4. Uniform flow with circulation over external polygon.

8. PERIODIC POLYGON

8.1. Introduction

The periodic polygon has been computed successfully by numerical integration by Floryan [38]. Using the upper half of the complex t -plane, with the infinite straight line as boundary, he extends the SCT formula to the infinite number of corners of the periodic polygon. The method is based on his discovery that only a finite number m of corners have to be used for the actual computation. Therefore Floryan [38] computes a polygon with a number m of similar polygon sides, and two straight half-infinite sides. This is the same as using the well-known fact that the details of a far enough part of the boundary has an asymptotically decreasing influence on the near solution. In fact, theoretical infinities are such an approximation in reverse of any real polygon. In our method of using the unit disk as premapping plane, such an approach is not feasible because decreasingly small Frobenius disks will be crowded infinitesimally at the infinity point.

The disadvantage of the method of [38], albeit small in numerical integration methods, is that m times as many product terms have to be computed than actual different sides of the polygon.

8.2. Periodic Mapping

The formula given in equations (4.1) and (4.7), and derived in Appendix B, is an explicit closed exact formula, with only the required number of terms and singularities, which is well adapted to our method requiring a finite number of convergence disks. A Möbius transformation of equation (4.1) results in

$$\frac{dz}{ds} = \int (s - \hat{b})^{-1} (1 - s \frac{\check{x}}{\hat{b}})^{-1} \prod (s - s_{ai})^{-\alpha_i} ds, \quad \sum \alpha_i = 0 \quad (8.1)$$

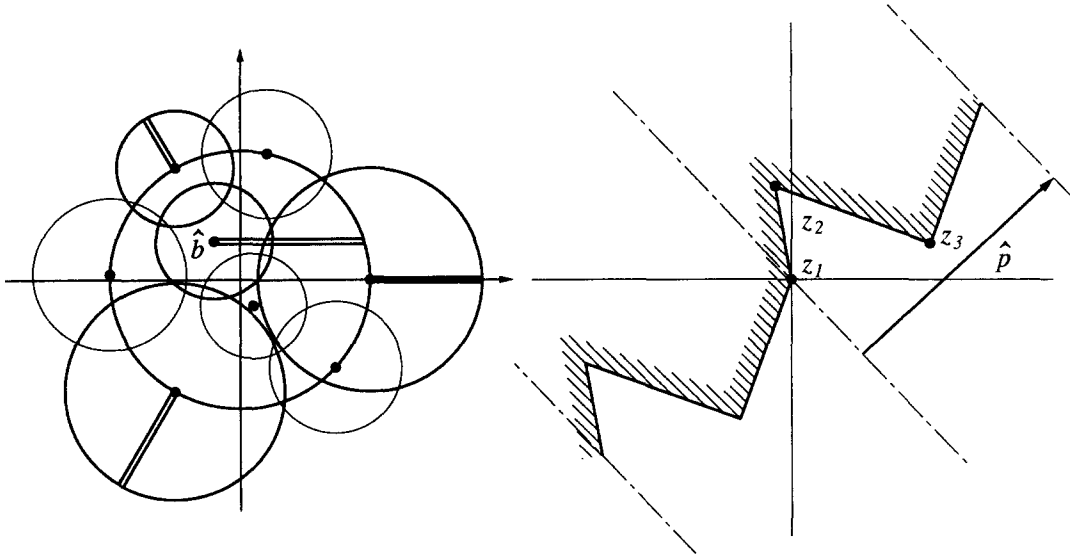
$$\equiv \int g(s) ds. \quad (8.2)$$

The form of equation (8.1) is invariant under bilinear transformation, and allows favourable adjustment of the distribution of corners on the circle.

The central Frobenius series around point \hat{b} is

$$z = g_0 \log (s - \hat{b}) + \underline{U} \cdot \bar{z}_F. \quad (8.3)$$

The logarithmic term is the one providing the multivalued periodical values of the the SC integral $z(s)$. The function $z(s)$ is not a continuous function in the s -disc as was the case with the previous polygons. The s -disc, considered as reverse function $s(z)$, consists therefore of infinitely many sheets of a Riemann plane. The singularity at \hat{b} causes an additional limit of the convergence disks. An example of typical convergence disks is shown in Figure 8.1a, with the discontinuity branch from \hat{b} . The mapping of the boundary is shown in Figure 8.1b, yet without any particular scaling constant \hat{c}_2 , where the resulting complex period \hat{p} is indicated.



(a) Periodic regions for 3 corners.

(b) Periodic boundary with 3 corners.

Figure 8.1.

The Frobenius, and additional Laurent and Taylor, expansions are obtained by convolution algebra as in the previous sections. Matching of the series is done such that the centers of the convergence disks are in one consistent sheet of the Riemann plane. The overlapping of some of the disks occurs in different sheets. Here only the central expansion needs special attention.

There is no particular constraint equation for the choice of the parameter \hat{b} as was the case in the external polygon. But the complex period \hat{p} is a function of \hat{b} . The factor in the logarithmic term is g_0 of the central Frobenius series, which is from a theorem in convolution algebra [20] directly obtained from the function $g(s)$ of equation (8.2)

$$g_0 = g(\hat{b}) \tag{8.4}$$

and the complex period is

$$\hat{p} = 2\pi\hat{g}_0. \tag{8.5}$$

The periodic polygon can then be lined up as required with the z -axes, as shown in Figure 8.2a, with a particular possible flow field $w(z)$. The complex potential is shown in the s -plane in Figure 8.2b,

$$w = \frac{-\hat{i}K}{2\pi} \left(\log(s - \hat{b}) + \log\left(s \overset{\times}{\hat{b}} - 1\right) \right). \tag{8.6}$$

Therefore, near infinity of the z -plane we obtain the perturbation form

$$w = \frac{K}{\hat{p}} \left(z - \underline{U} \cdot \overline{z}_F \right) - \frac{\hat{i}K}{2\pi} \log\left(s \overset{\times}{\hat{b}} - 1\right) \tag{8.7}$$

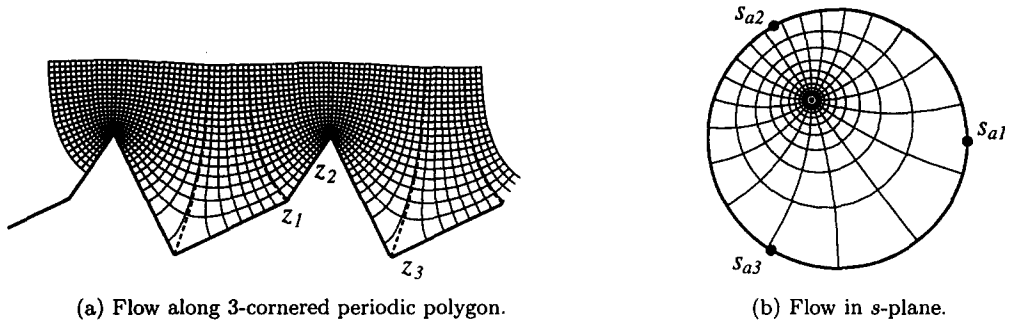


Figure 8.2.

$$\frac{s}{\hat{b}} \rightarrow \frac{K}{\hat{p}} z - \frac{\hat{i} K}{2\pi} \log(b^2 - 1). \quad (8.8)$$

From equation (8.8) the constant K is determined to satisfy the infinity boundary condition.

Comparing the flow of Figure 8.2a with the flow along a wall in Section 5.1, it is clear that the periodic polygon can be interpreted as interior polygon. As such, it can have infinity points on the boundary, such as shown in Figure 8.3a. The corresponding complex potential in the s -plane is

$$w = \frac{h - \hat{i}\Gamma}{2\pi} \log(s - \hat{b}) + \frac{h + \hat{i}\Gamma}{2\pi} \log(s - \hat{b}) - \frac{2h_1}{2\pi} \log(s - s_1) - \frac{2h_2}{2\pi} \log(s - s_2), \quad (8.9)$$

where $h_1 + h_2 = h$. By adjusting the constants, any stagnation points between the channels can be chosen, or *vice versa*. The streamlines of the potential flow of equation (8.9) are shown in Figure 8.3b, as they pass through all the disks. Similar to the exposition above, perturbation forms can be derived for each of the infinities in the z -plane. Infinities in each period can branch out as any of the infinities of the interior polygon, in overlapping periodic sheets.

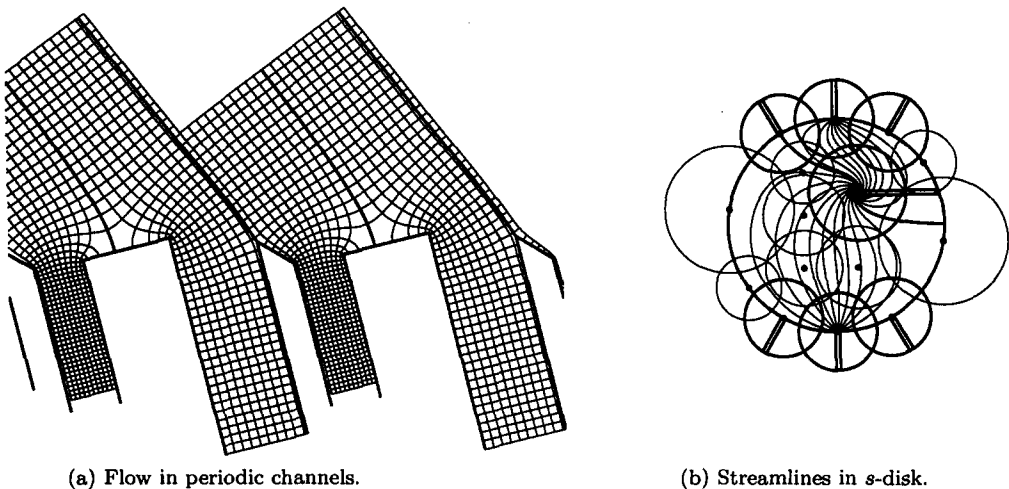


Figure 8.3.

8.3. Elliptic Integral III

There may be winding points in a periodic polygon, as shown in Figure 8.4a, with a turning angle of -270° at z_3 . A possible flow, like $w(s)$ in equation (8.6), is shown in one period only so that the overlapping regions can be distinguished.

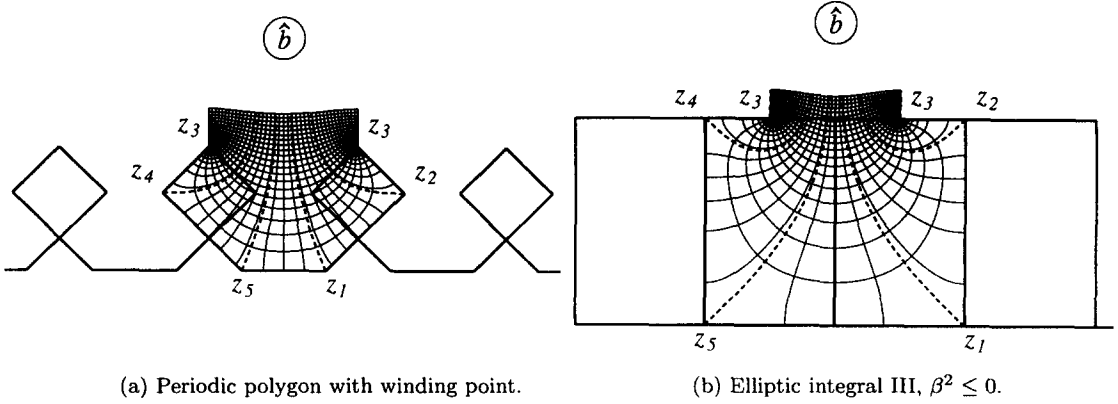


Figure 8.4.

When mapping the real axis of the t -plane on the unit circle in the s -plane by the bilinear transformation

$$s = \frac{1 + \hat{t}}{1 - \hat{t}}, \quad t = \hat{t} \frac{1 - s}{1 + s}, \tag{8.10}$$

the elliptic integral of the third kind

$$z = \int \frac{dt}{(1 - \beta^2 t^2) \sqrt{(1 - t^2)(1 - k^2 t^2)}} \tag{8.11}$$

is transformed to

$$z = \hat{c} \int (s - b)^{-1} (1 - bs)^{-1} \prod_{i=1}^5 (s - s_{ai})^{-\alpha_i} ds, \quad \sum_{i=1}^5 \alpha_i = 0. \tag{8.12}$$

For real $\beta^2 < 0$, called circular cases [21],

$$b = \frac{1 - \beta}{1 + \beta}, \quad \alpha_i = \begin{cases} \frac{1}{2}, & i \leq 4, \\ -2, & i = 5, \end{cases} \tag{8.13}$$

which in this form is seen to be a mapping of the s -circle on a 5-cornered periodic polygon, with the two singular points b and $1/b$ not on the circle. The mapping is like a further distortion of the mapping of Figure 8.4a, with 4 corners of 90° , and where the winding angle is increased to -360° . The winding corner is not visible in the real form of equation (8.11), because it happens at infinity on the real axis, which is mapped on the finite point $s = -1$.

The same flow from equation (8.6), Figure 8.2b, is shown mapped into one period in Figure 8.4b, with two adjacent overlapping rectangles. The adjacent periods are joined at the vertical potential line above the rectangle.

8.4. Nonperiodic Flow

The stream or potential function in the examples above is continuous in the s -disk, resulting in periodic flow in the z -plane. If for any reason nonperiodic flow exists, then the mapping of the periodic polygon on the upper half of the t -plane is required, with all periods of the z -plane mapped on a continuous sequence of rectangular half-infinite strips of the t -plane. This is accomplished by mapping all sheets of the Riemann plane in the s -disk on the t -plane by the transformation

$$t = \frac{1}{2\pi\hat{t}} \log s, \quad s = e^{2\pi\hat{t}t}, \tag{8.14}$$

where the point \hat{b} is shifted to 0 by a bilinear mapping first. The central Frobenius series then becomes

$$\begin{aligned} z &= \hat{c}_2 \hat{g}_0 \log s + \sum f_{zk} s^k \\ &= t + \sum f_{zk} e^{2\pi k \hat{t}} \\ &\xrightarrow[0]{s} t \end{aligned} \quad (8.15)$$

using equation (8.5), and choosing the constant $\hat{c}_2 = 1/\hat{p}$. Equation (8.15) constitutes a uniform map plus a Fourier series, valid for $\Im(t) > (-\log \rho)/2\pi$. On the boundary the different Frobenius, Laurent, or Taylor series apply.

It is therefore easy, once the periodic mapping solution is available, to map any flow in the upper half of the t -plane on the periodic polygon in the z -plane. An example is shown in Figure 8.5.

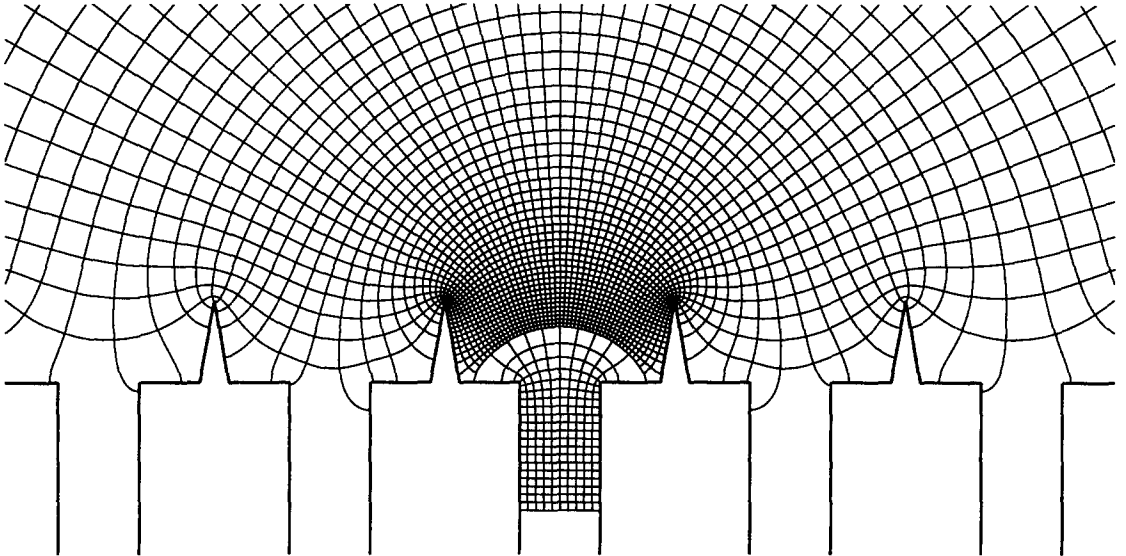


Figure 8.5. Nonperiodic flow in periodic mapping.

9. CYCLIC POLYGON

The purpose of the SCT for cyclic polygon is a time saver, considering that all polygons can be mapped with the three basic forms of internal, periodic, and external forms.

Let the original disk be in the ζ -plane, and consider the regular SCT formula of equation (4.1) for a polygon with m cycles and n corners in each cycle. If the points of each cycle are spaced in equal sectors of the circumference of the ζ -disk, then the SCT formula of equation (4.1) becomes the well-known SCT formula for the cyclic polygon, see [34,35],

$$z = \int \zeta^j \prod_{i=1}^n (\zeta^m - \zeta_{ai}^m)^{-\alpha_i} d\zeta, \quad (9.1)$$

where $j = 0$ for the internal and $j = -2$ for the external polygon. The SCT of the cyclic polygon with m cycles is obtained from the symmetric form of equation (9.1) to a new s -disk by the transformation, see [28],

$$s = \zeta^m, \quad (9.2)$$

with the result as given by equations (4.1), (4.5), and (4.6). On this a bilinear transformation which shifts the center to a point \hat{b} produces then the invariant form

$$z = \int (s - \hat{b})^{(1-m)/m} \left(1 - s \frac{\times}{\hat{b}}\right)^{(1-m)/m} \prod_{i=1}^n (s - s_{ai})^{-\alpha_i} ds. \tag{9.3}$$

In equation (9.3), a singularity is always present at the internal point \hat{b} . The advantage of equation (9.3) is that only the number of different corners n of one cycle appear as simple singularities on the circle in the s -disk, suitable for Frobenius series, with only as many Frobenius disks on the boundary. One cycle of the polygon is mapped by equation (9.3), using the simplest of the complex roots. The other cycles are obtained by multiplication with $e^{\hat{2}2\pi i/m}$. Any cyclic potential function in the polygon may be a mapping of the potential function in the s -disk, $w(s)$. But it does not have to be cyclic, in which case it is mapped from a potential function in the ζ -disk, $w(\zeta)$.

9.1. Internal Cyclic Polygon

The central Frobenius series has the form

$$z = (s - \hat{b})^{1/m} \times \underline{U} \cdot \bar{z}_F. \tag{9.4}$$

The one chosen of the m different roots of the first term determine to which the sector the s -disk is mapped. The regions of a typical case are shown in Figure 9.1a, Frobenius disks in thick lines and Taylor disks in thin lines. The discontinuity branch from \hat{b} is taken in the real direction as shown. Expansion and integration in each other disk proceeds in the usual manner. Matching is started from the central Frobenius disk with integration constant of 0. All other disks are then matched in such a sequence that matching never crosses the discontinuity branch. In such a way, a continuous single sector of the polygon is obtained. The mapped polygon with a cyclic potential function is shown in Figure 9.1b.

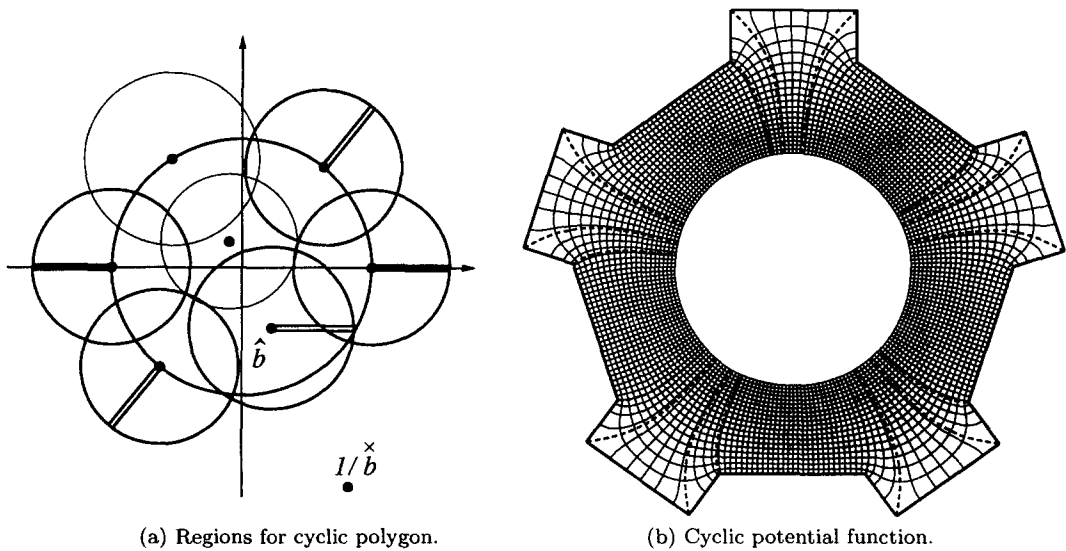


Figure 9.1. Mapping of internal cyclic polygon.

If a case with extremely many cycles, which means extremely large relative radius, has to be treated, then a combination of periodic and cyclic SCT will have to be derived, using a log-series for the central Frobenius disk.

9.2. External Cyclic Polygon

The central Frobenius series has the same form of equation (9.4), except that the number of cycles is counted with a negative number m . In contrast to the single external polygon, no logarithmic terms appear in the central Frobenius series for any finite m , and therefore no balancing of the position \hat{b} is required. Interestingly, if we, for example, treated an external polygon with m -cycles as simple external polygon with $-m \times n$ corners, then balancing would be required.

The only difference in the iteration computer program is that allowance must be made for negative m where this is used as counter.

An external cyclic polygon with the same geometry of corners is shown in Figure 9.2, the regions in Figure 9.2a, and a possible external potential function in Figure 9.2b.

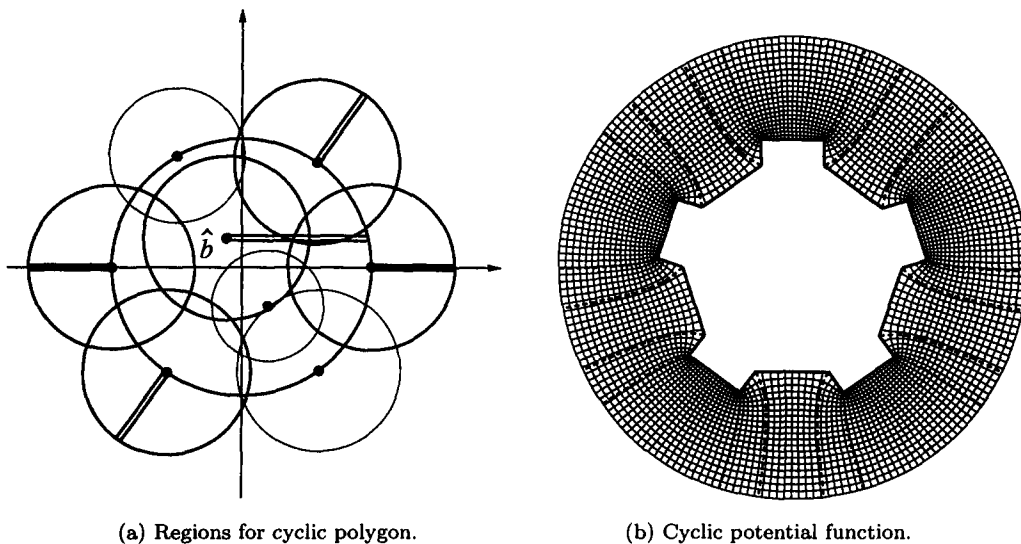


Figure 9.2. Mapping of external cyclic polygon.

10. PARAMETER ITERATION

Every SCT solution method needs an iteration routine. There are many satisfactory existing routines used in the numeric SCT solutions, and it only remains to implement one of them in terms of our analytical method, with some modifications that we have found useful.

The constants s_i in the SCT, equation (4.1), are the known as the parameters. They are distinguished from the constants α_i , which are of course also parameters of the SCT formula, because in all known applications the latter are always given. Generally the posed problem is the mapping on a given polygon, where the cornerpoints z_{α_i} are given. Then the parameters s_i in the SCT are unknown, and must be determined by iteration, which makes them so important in the so-called *parameter problem* [28,37]. In [3], they are called accessory parameters, and everybody else quoting Trefethen's method calls them so, e.g., Henrici in [4], perhaps having the cornerpoints z_{α_i} as primary parameters in mind, which are parameters of the problem, but not of the SCT formula. Accessory parameters are actually the parameters of Schwarz's differential equation which maps the circular arc polygon on the circle of the half-plane [28,37].

The parameter problem is posed as a set of nonlinear equations. These are solved numerically by an optimization method by Costamagna [5]. Howe [1] uses a Simplex least squares method. Successive approximation using relations between particular constants and polygon sides are used by Minuhin [18], thus avoiding the Jacobian matrix, i.e., a scalar iteration. Also a scalar iteration is the method by Chaudhry and Schinzinger [7], who relate the parameters to the next sides of

the polygon, starting from the fixed parameter. Trefethen [3] uses the Newton-Raphson iteration, substituting the Jacobian matrix by a finite difference matrix as used in an available nonlinear equation solver. Nearer to an analytical Jacobian matrix, Chuang *et al.* [8] approximate the derivative by a Lagrange interpolation over a few numerically determined variations.

We have chosen the Newton-Raphson method, and present here first the development of the nonlinear equations. As z -plane parameters we use coordinates of cornerpoints rather than ratios of lengths of sides. Consequently, we have to include the integration and multiplicative complex constants \hat{c}_1 and \hat{c}_2 in the general SCT for the n -sided polygon

$$z = \hat{c}_1 + \hat{c}_2 \int_{s_0}^s \prod_{i=1}^n (s - s_i)^{-\alpha_i} ds. \tag{10.1}$$

The complex symbol $\hat{}$ is used for the constants to emphasize the number of scalar components.

10.1. The Nonlinear Equations

Our first modification of the existing methods is to use the Cartesian dimensions of the coordinates as target values in the nonlinear parameter equations. Let us follow Figure 10.1a, and treat it as a general irregular polygon with six corners, two at infinity. All points are marked in a positive turning sequence, i.e., counterclockwise. To start with any finite point, say point 1 without loss of generality, we need the two coordinates x_1 and y_1 . These first two coordinates are stored as the first two elements of an array of scalar fixed values, \overline{z}^c , as z^{c1} and z^{c2} . We draw both backward and forward direction lines from point 1 according to the prescribed turning angles. To reach point 2, we enter x_2 as next element, $z^{c3} = x_2$, and draw the direction line towards point 3. To fix point 3, we have the choice of using either ordinate x_3 or y_3 . In practice we would use the rule: the ordinate to be used is the one which is best conditioned to define point 3 coming from point 2. If line 2-3 slopes $> 45^\circ$ then we use y_3 , if it slopes $\leq 45^\circ$ then we use x_3 , which is the case here, therefore $z^{c4} = x_3$. Actually this rule was already employed using $z^{c3} = x_2$. The infinity point 4 cannot be drawn, therefore we do not attempt to attach any coordinates to it. But so is point 5. The way to draw the partial line 4-5 is to use the height h above point 1. We have marked a point P with a \bullet on this line, with otherwise no specified coordinates. We will call it a degenerate point, adapted from Trefethen [3], who calls it a degenerate vertex. The height h and the direction of line 4-5 is sufficient to draw this line. We enter $z^{c5} = h$. We will not allow to use y_4 or y_5 in the place of h , considering z_4 and z_5 infinite in general nonaligned axes. The next finite point is 6. Because the direction 1-6 is already drawn, we need only one ordinate to fix it, and because of the slope of 1-6 being $< 45^\circ$, it is best fixed by x_6 , so that $z^{c6} = x_6$. We have now defined a 6-sided polygon with given 6 turning angles, by 6 dimensions.

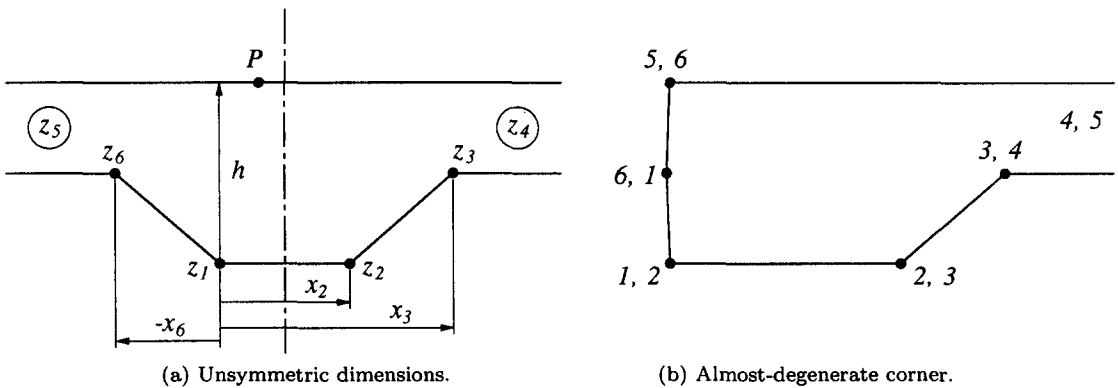


Figure 10.1. Typical 6-sided polygons.

To introduce an ill-condition in selecting a sequence of independent dimensions, we show in Figure 10.1b a polygon with two possible numberings of corner points, and with a turning angle

of α of 0 or nearly 0, at a point which we call a degenerate vertex, in analogy of Trefethen's terminology. Just like we have to be prepared for an occasional 0 turning up in computations, we have to allow for an occasional degenerate vertex. This might happen if we do a study on varying angles where α might pass through 0 on its way from positive to negative. If we number the polygon starting with 1 at the degenerate corner, then giving the sequence of dimensions $x_1, y_1, y_2, x_3, x_4, y_6$ will define every corner in a well-conditioned manner, particularly corner 6 which is defined last by two orthogonal lines. But if we start numbering one point below, making the lower left corner point 1 and giving the sequence of dimensions $x_1, y_1, x_2, x_3, y_4, x_6$, then the degenerate corner 6 is not defined at all. If what is now α_6 is not 0 but near to 0, then the definition of corner 6 is ill-conditioned. Such arbitrariness is unacceptable and a well-posed method is presented further below.

The next step in data preparation is to designate the point to fix the origin of the z -plane, which is determined by adjustment of the positioning constant \hat{c}_1 . This must be a point with two coordinates, for example point 1, i.e., elements z^{c1} and z^{c2} .

Next we choose one coordinate to determine the magnitude $|\hat{c}_2|$. This may be x_2 , but preferably the largest coordinate in the array, which is element $z^{c5} = h$. We collect the remaining elements into a new array of target values

$$\bar{z}^t : z^{t1} = z^{c3}, \quad z^{t2} = z^{c4}, \quad z^{t3} = z^{c6}. \quad (10.2)$$

These are the values to which another variable array \bar{z}^e must converge during iteration, where $z^{c1} = x_1$ and $z^{c2} = y_1$ have been left out because they are used for \hat{c}_1 . The error during iteration is called $d\bar{z}^e$, computed as

$$d\bar{z}^e = \bar{z}^e - \bar{z}^t, \quad (10.3)$$

where $d\bar{z}^e = \bar{0}$ when the solution is met. Note that we have used the perhaps slightly inconsistent name z for the real elements in the vectors in equation (10.3), while z in equation (10.1) is the notation of the complex variable. In this section, all vector and matrix elements are real but denoted by z .

We turn now to the points s_i on the circle, defined by the phase angles ϕ_i . Three points must be fixed, according to Riemann's mapping theorem. For lack of better information, or intuition, we fix those points which lie closest to three uniformly distributed points, i.e., closest to 120° spacing. In this example, we may fix $\phi_1 = 0, \phi_3 = 120^\circ, \phi_5 = 240^\circ$. Note that Trefethen [3] has avoided fixing more than one point by choosing a point z_0 (w_c in his notation) to be the mapping of $s = 0$, to ensure best uniformity. But we believe that the two methods are equivalent in not guaranteeing any uniformity in the end result whatsoever.

The remaining angles which are free to be shifted during iteration are collected into an array $\bar{\phi}^v$, $\phi^{v1} = \phi_2, \phi^{v2} = \phi_4, \phi^{v3} = \phi_6$. The amount that they are shifted during each iteration step is $d\bar{\phi}^v$. The number of elements in $\bar{\phi}^v$ are the degrees of freedom $n_v = n - 3$, which is 3 in this case. The angles $\bar{\phi}^v$ are used in the SCT to compute the estimates \bar{z}^e , which we write functionally as

$$\bar{z}^e(\bar{\phi}^v) = \bar{z}^e. \quad (10.4)$$

Equation (10.4) is the set of nonlinear equations to be solved for the three correct positions $\bar{\phi}^v$ to obtain the three target values $\bar{z}^e = \bar{z}^t$ in equation (10.2).

The iteration process starts with the solution of the SCT using the initial estimated $\bar{\phi}^v$, augmented with the fixed positions to $\bar{\phi}^n$, to compute the initial approximation $\bar{z}^e \neq \bar{z}^t$.

The differential of equation (10.4) is

$$\frac{d\bar{z}^e}{d\bar{\phi}^v} \cdot d\bar{\phi}^v = d\bar{z}^e. \quad (10.5)$$

$\frac{dz^e}{d\bar{\phi}^v}$ is the Jacobian matrix. The N-R method consists of solving the matrix equation (10.5), at each iteration step, by Gauss elimination, which we write formally as a matrix left division

$$d\bar{\phi}^v = \frac{dz^e}{d\bar{\phi}^v} \setminus dz^e. \quad (10.6)$$

The Jacobian matrix in equation (10.5) is computed by two alternative means to be described later.

We construct a distribution matrix \underline{D}_v^n , which directs the solution $d\bar{\phi}^v$ to the change of all angles $\bar{\phi}^n$ during iteration,

$$\underline{D}_v^n \cdot d\bar{\phi}^v = d\bar{\phi}^n. \quad (10.7)$$

In this example, the distribution matrix is

$$\underline{D}_v^n = \begin{bmatrix} 0 & 0 & 0 \\ 1 & 0 & 0 \\ 0 & 0 & 0 \\ 0 & 1 & 0 \\ 0 & 0 & 0 \\ 0 & 0 & 1 \end{bmatrix}. \quad (10.8)$$

The empty rows in the distribution matrix are the mathematical implementation of keeping angles ϕ_1 , ϕ_3 , and ϕ_5 fixed. Note that with a slight rearrangement in the vector \bar{z}^c , we have a transposed relation

$$\bar{z}^e = [\underline{D}_v^n]^T \cdot \bar{z}^c. \quad (10.9)$$

In any N-R iteration method, the solution of equation (10.6) has to be clipped to advance in a curved fashion in $\bar{\phi}^n$ -space to the solution to prevent spurious overshooting, which is well indicated by the differential symbols. In the SCT in particular, the solution has to be clipped at least to satisfy the distribution of the angles

$$\phi_1 < \phi_2 < \dots < \phi_n. \quad (10.10)$$

Trefethen [3] eliminates the constraint of the unknown variable by a mathematically elegant and numerically efficient transformation of the variable ϕ_v in each interval. We have not yet incorporated his method in our computations.

By a simple linear computation we determine the smallest vector $\Delta\bar{\phi}^n$ proportional to $d\bar{\phi}^n$ that makes one of the inequalities in equation (10.10) an equality. The solution $d\bar{\phi}^n$ is then clipped to

$$d\bar{\phi}_c^n = c_r \Delta\bar{\phi}^n, \quad (10.11)$$

where $c_r < 1$ is a clipping ratio. By this means we satisfy both conditions of equation (10.10) and of a curved approach to the solution. The clipping is released as soon as $d\bar{\phi}^n / \Delta\bar{\phi}^n < c_r$.

The N-R iteration step ends with

$$\bar{\phi}^n(\text{new}) = \bar{\phi}^n(\text{previous}) - d\bar{\phi}_c^n. \quad (10.12)$$

To get from the solution $\bar{\phi}^n$ to the values \bar{z}^e , we define the intermediate functions

$$I(\phi) \equiv \int \prod_{i=1}^n (s - s_i)^{-\alpha_i} ds + f_{0k}, \quad (10.13)$$

$$z = f(\phi) = \hat{c}_1 + \hat{c}_2 I(\phi), \quad (10.14)$$

so that a particular cornerpoint is determined by

$$z_k = \hat{c}_1 + \hat{c}_2 I_k, \quad (10.15)$$

where $I_k = I(\phi_k)$, and the constants f_{0k} are determined by matching. For all finite points, the integrals $I(\phi_k)$ are equal to the constants in the functions in the Frobenius disks after matching; see Section 4.3. Degenerate points, like P in Figure 10.1a, must be determined by evaluating the function $I(\phi_P) = I_P$ for a suitable value of ϕ , for which we choose

$$\phi_P = \frac{\phi_{i1} + \phi_{i2}}{2}, \quad (10.16)$$

where $i1$ and $i2$ are the numbers of the corners before and behind P .

Two options to determine the scaling constant \hat{c}_2 will be used. The first is to use the complex target length between any two finite points A and B , $\hat{l} = z_B^t - z_A^t$, so that from equation (10.15) follows

$$\hat{c}_2 = \frac{\hat{l}}{I_B - I_A}, \quad (10.17)$$

where z^t indicates a target dimension, so that \hat{c}_2 is determined during the iteration before the iterated values of z are known. The second option is to specify orientation and magnitude separately,

$$\hat{c}_2 = |c| e^{i\gamma} \equiv |c| \hat{e}_c. \quad (10.18)$$

The desired orientation is prescribed by a complex direction number

$$\hat{e}_r \equiv e^{i\beta} \quad (10.19)$$

by which we choose the direction of a particular line to be, in the example the direction of the line 4-5 is given by $\hat{e}_r = -1$, which happens to be real. The direction of the line is given by the original SC differential equation by the direction of the differential dz , which is directly after the corner r

$$\frac{dz}{d\phi} \equiv \left| \frac{dz}{d\phi} \right| \hat{e}_r = \hat{c}_2 \prod_{i \neq i_1} (s_r - s_i)^{-\alpha_i} \times (\hat{i} s_r)^{1-\alpha_r} \equiv \hat{c}_2 \hat{d}. \quad (10.20)$$

Write $\hat{d} = |d| e^{i\delta} \equiv |d| \hat{e}_d$, then

$$\hat{e}_c = \frac{\hat{e}_r}{\hat{e}_d}. \quad (10.21)$$

The magnitude is prescribed by the required normal distance h from a point Q to the line containing the degenerate point P ,

$$b + \hat{i} h = \frac{z_P - z_Q}{-\hat{e}_r} \quad (10.22)$$

$$= \hat{c}_2 \frac{I_P - I_Q}{-\hat{e}_r} \quad (10.23)$$

$$= |c| \hat{e}_c \frac{I_P - I_Q}{-\hat{e}_r}, \quad (10.24)$$

where b is an unknown parallel distance, along the line through P . From the imaginary part of equation (10.24), the magnitude $|c|$ is determined.

We are only now ready to determine \hat{c}_1 . Let the finite point to be used to fix \hat{c}_1 be z_O^t , then from equation (10.15)

$$\hat{c}_1 = z_O^t - \hat{c}_2 I_O. \quad (10.25)$$

We may also specify the middle of two points z_O^t and z_T^t such that

$$\hat{c}_1 = \frac{1}{2} (z_O^t + z_T^t) - \hat{c}_2 \frac{1}{2} (I_O + I_T). \quad (10.26)$$

The end effect is the same as equation (10.25). The purpose of equation (10.26) is to get a symmetric display of the iterated polygon on the computer screen during iteration on a PC.

In the iteration loop, we have now arrived at a point that we can determine the cornerpoints from equation (10.15). Independent of the option to determine the constant \hat{c}_2 , we want to include any possible dimensions of degenerate points, like h in Figure 10.1a, of which there may be two in the worst case, or even more in rather abstract overlapping polygons. Such dimensions are determined by equation (10.15), where now \hat{c}_2 is already known. All the cornerpoints, including degenerate dimensions, but also \hat{c}_1 and \hat{c}_2 , are values that vary during the iteration.

This brings us to the beginning of the loop with the new error in equation (10.3). The iteration can proceed once the Jacobian matrix is determined, described below.

10.2. The Quotient Matrix

All numerical Newton-Raphson method approximations employ an approximation of the Jacobian matrix by a Quotient matrix, even if indirectly by Chuang *et al.* [8], or by a packaged solver [3]. The Quotient matrix is

$$\frac{d\bar{z}^e}{d\bar{\phi}^v} \approx \frac{\Delta\bar{z}^e}{\Delta\bar{\phi}^v}. \quad (10.27)$$

First we compute the columns of the larger matrix $\Delta\bar{z}^n/\Delta\bar{\phi}^v$ by solving the SCT by the same routine n_v times with positions $\phi_1, \phi_2, \dots, \phi_i + \Delta\phi_i, \dots, \phi_n$, subtracting the basic solution $\bar{z}^n(\bar{\phi}^n)$, and dividing by $\Delta\phi_i$ (hence, *Quotient matrix*), which is the customary method. Each variation $\Delta\phi_i$ corresponds to a column

$$\Delta\bar{\phi}_i^n = \bar{D}_i^n \Delta\phi_i. \quad (10.28)$$

The solution is in terms of the expansions in convergence disks, which only need to cover the circle boundary during iteration. The computational effort in our analytical method is getting the expansions, while the determination of the cornerpoints afterwards is trivial, all n points being available after matching. The evaluation of the series is necessary for the matching, only any degenerate points will require additional series evaluation. Therefore it is no more effort to compute the complete column $\Delta\bar{z}^n/\Delta\phi_i$ than to compute the partitioned column $\Delta\bar{z}^e/\Delta\phi_i$.

The stepsize $\Delta\phi_i$ is controlled to ensure both that $\phi_i + \Delta\phi_i$ remains in the available gap, and that the column $\Delta\bar{z}^e/\Delta\phi_i$ is a reasonable finite approximation of the partial derivative $\frac{\partial\bar{z}^e}{\partial\phi_i}$.

The n_v expansions and evaluations for matching are the equivalent of the $n_v \times n_v$ numerical integrations of the numerical method.

The Quotient matrix $\Delta\bar{z}^e/\Delta\bar{\phi}^v$ is a partition of the independent rows of $\Delta\bar{z}^n/\Delta\bar{\phi}^v$ with which the Gauss elimination in equation (10.6) can now proceed. But that is not what we are going to do.

10.3. The H-Matrix

Instead of solving equation (10.5), we solve the overdetermined matrix equation

$$\frac{dz^{-n}}{d\phi^v} \cdot d\phi^v = dz^{-n} \quad (10.29)$$

by Gauss elimination with total pivot search. We call this the H-matrix method for short because it is usually introduced in matrix algebra texts under homogeneous equations [49]. The right vector is the difference between iterated computed values of all finite corner points and all target dimensions,

$$dz^{-n} = \bar{z}^n - z^{tn} \quad (10.30)$$

instead of equation (10.3). Therefore, we supply all finite target coordinate dimensions instead of having to determine an independent set at the input stage. The pivot search elimination routine will select exactly n_v independent rows, and the solution is unique because the right vector is compatible. But not only will the pivot search select independent rows, it will also select the best conditioned independent rows. In the example of Figure 10.1a, it will select the dimension x_2 from both x_2 and y_2 . If the coordinate axis direction changes, the selection will change. The computational effort is not more since only n_v rows are used for computation. The extra computer storage of the larger matrix is trivial compared to the convolution numbers. We have followed the selection of rows by the H-matrix routine in some examples, and found it quite surprising in what sequence a figure can be drawn instead of the sequence described in Section 10.1. The angles and dimensions of a polygon are determined by a problem orientated subroutine, which also computes \hat{c}_1 and \hat{c}_2 . Therefore we do not have to give the information to the main program of which dimensions are now redundant, the H-matrix routine will simply eliminate those rows. We can change the reference points for \hat{c}_1 and \hat{c}_2 without any information to the main program; the H-matrix routine will just select appropriate other rows. We can also use any other conceivable consistent method to compute \hat{c}_1 and \hat{c}_2 in the problem routine without any effect on the main routine at all. This method also solves the problem of full or almost degenerate vertices of a polygon. We have compared the H-matrix method with the normal determined method and found no difference in performance. But it relieves us of all the constraints of posing the problem dimensions; the H-matrix sorts it out, better than we can prepare it by limited insight.

10.4. Fixpoints

We call a particular distribution of ϕ_i a *constellation*. We have made experiments with crowded points in a constellation and found the rather surprising result that crowding does not slow the convergence down, it merely affects the final accuracy, although this end effect is undesirable in itself, and limits the range of problems we can compute. But what we did find is that the choice of the three fixed points on the circle influence the convergence rate very much. As demonstration, we show a typical path of the vector $\bar{\phi}^n$ during iteration projected on the plane ϕ_3, ϕ_4 for ill-chosen fixed points in Figure 10.2a. In Figure 10.2b, a typical path for better chosen fixed points is shown, projected on the plane ϕ_2, ϕ_4 . The starting point is marked by a \bullet in the figures.

As a remedy, it is not sufficient to place evenly distributed fixed points on the circle at the beginning of the iteration, because these may be badly chosen in the final constellation.

Although we may choose best 120° spaced fixpoints, a regular 3-pointed star pattern, intuitively, there is no theory available to confirm this. Therefore we have made some experiments with different problems as follows. We used no fixpoints at all, contrary to Riemann's mapping theorem, and constructed a larger H-matrix $\Delta z^{-n} / \Delta \bar{\phi}^n$, still containing all the overdetermined rows. The total pivot search in the H-matrix solution covers all rows and columns. We prescribed

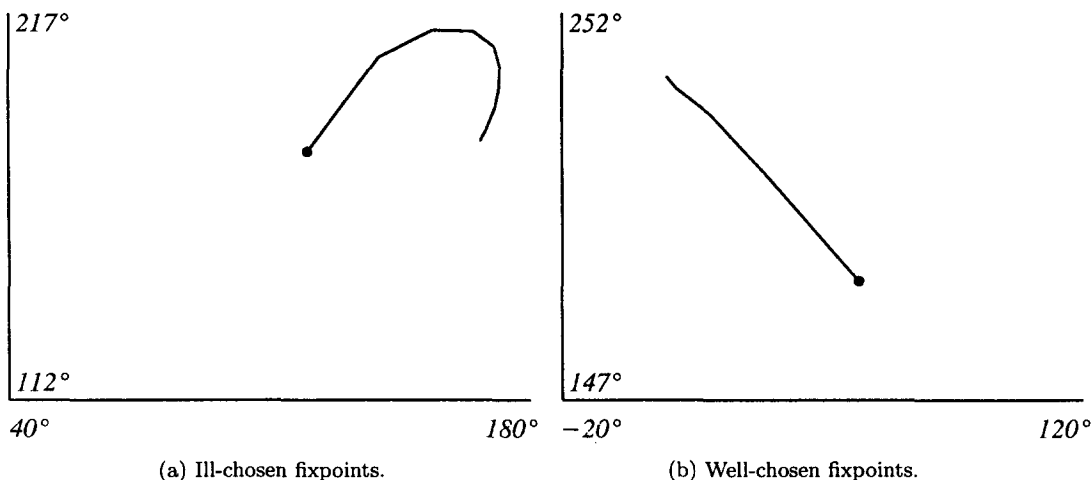


Figure 10.2. Projected convergence path in ϕ -space.

the rank of the matrix as $n_v = n - 3$ and followed now which three columns are not selected. These are the fixpoints. The other points were then used in the continuing iteration.

The result was almost as expected. Throughout the iteration, the three fixpoints were always selected (i.e., omitted in the H-matrix) in almost the regular star pattern. The only strange result was that within a few degrees not the best possible regular star pattern was selected. Therefore we use the empirically determined rule to use fixpoints as near as possible to a regular star pattern. This is determined by a search-like routine at each iteration step, and the routine continues with new variable points at each iteration. In this way, we start with a regular star pattern at the beginning and we end with a best approximated one. Perhaps in the future such a rule can be confirmed theoretically, along the lines of condition number of matrices.

We cannot use the larger H-matrix method to determine the fixpoints during the iteration because we would waste the computation of three extra columns, i.e., three full SCT computations.

It was further interesting to find out whether the rank of the larger H-matrix is in fact $n - 3$. This was difficult to determine, as the matrices are often quite ill-conditioned, and a suitable small ϵ to determine numerical rank could not be estimated. But towards the end of each iteration the distinction was quite clear; the rank could confidently be established as $n - 3$, which is actually a numerical verification of Riemann's mapping theorem.

10.5. Bilinear Conditioning

It has been noted before that an iteration routine like the one above may tend to crowd some points unfavourably. Trefethen [3] has noted that this can always be alleviated by a Möbius transformation. But this is too late after convergence. Crowding causes inaccuracies due to small differences in ϕ_i while ϕ is a potential-like function with a range of 2π .

We have therefore introduced a Möbius transformation, also called bilinear transformation, after each iteration step. This consists of selecting the two smallest gaps and make them equal and on opposite positions of a diameter, which makes them a maximum. If the gaps are adjacent, then the maximum will be obtained by an equilateral of the three points on the circle. But this will make other gaps smaller again. Therefore, the bilinear transformation is done in small increments at a time. A bilinear transformation can be considered as a shift of the center of the circle by a complex number \hat{b} to another point. We calculate the number \hat{b} to effect the maximizing of the two smallest gaps, but then transform only by a small fraction $\Delta\hat{b}$. After this, we look for the new two smallest gaps and continue. The process stops if either the two gaps are equal and opposite, or if a third, previously larger, gap becomes as small. We found that with approximately one to five such steps our goal has been achieved. We have not yet made experiments to relate the size of $\Delta\hat{b}$ to the number n of the polygon. Each iteration step

starts then with the best possible condition of a constellation. In the example of Trefethen's Figure 10b [3] (see Figure 5.7b), we get without bilinear conditioning, a smallest gap of 0.05240° and an accuracy of $4 \cdot 10^{-5}h$ at convergence after 16 iterations, where h is the channel width. With bilinear conditioning, we get two smallest gaps of 2.0082° and an accuracy of $5 \cdot 10^{-6}h$ at convergence after 15 iterations. The problem gets worse with small gaps; we have constructed a more difficult 6-cornered example, where without bilinear conditioning the smallest gap is $.0009^\circ$, which reduced to $.04^\circ$ with conditioning. If no better initial information is available, the iteration is started with uniformly distributed points. After convergence, the constellation is unique for each problem, independent of the fixpoints.

We show in Figure 10.3 the projected path of the iterated solution vector with bilinear conditioning, with ill-chosen fixpoints in (a) and well-chosen fixpoints in (b), for the same problem. In an alternative graphical display, the convergence of a 12-sided polygon is shown in a $(\phi, \text{iteration-step})$ -diagram in Figure 10.4a and Figure 10.4b, without and with bilinear conditioning.

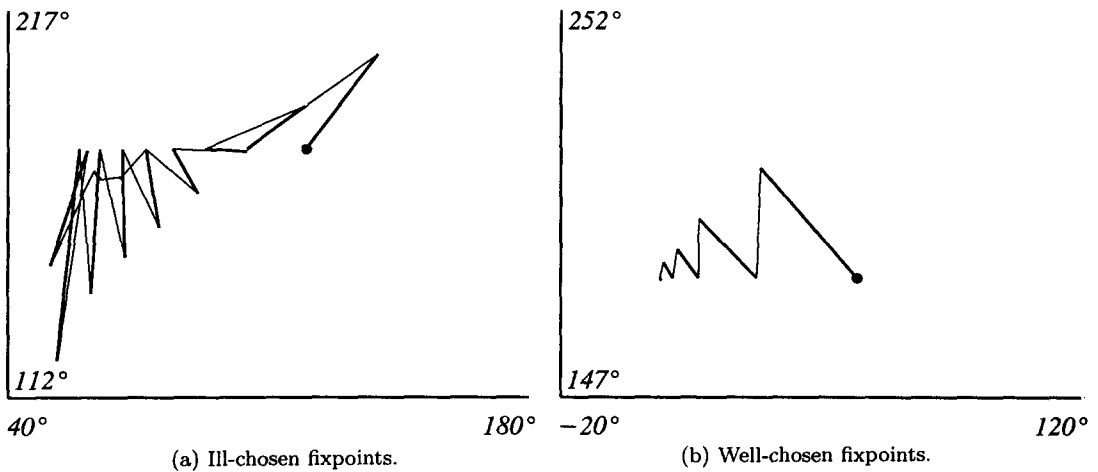


Figure 10.3. Projected convergence path in ϕ -space, with bilinear conditioning.

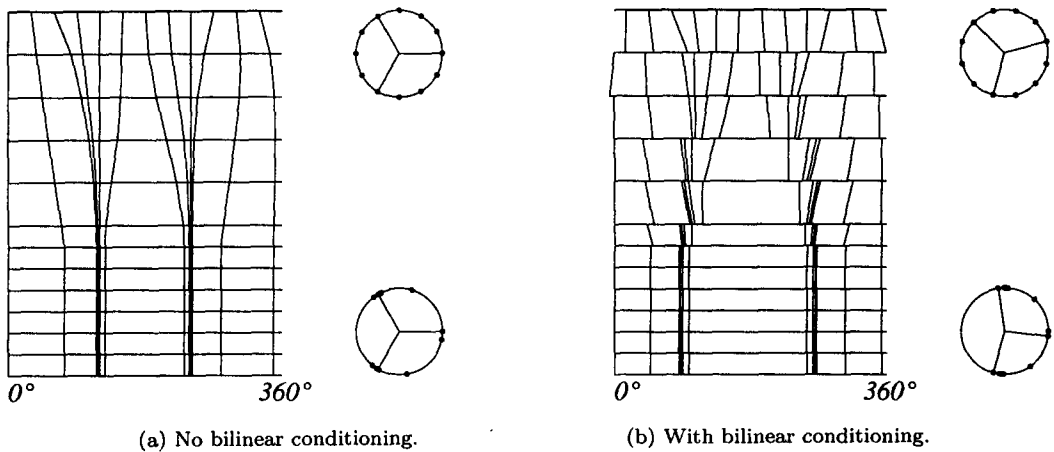


Figure 10.4. Convergence path $(\phi^n, \text{iteration-step})$.

The small gap and corresponding inaccuracy is also associated with an ill-conditioned Quotient matrix. Results of the used rows of the Quotient matrix and the Euclidean matrix condition number k_E , see [46,50], are presented in Table 9.1, for the polygon in Figure 10.1a. In Case (a), bad fixpoints and no bilinear conditioning were applied, and in Case (b), the fixpoints and bilinear conditioning were applied as described above. While the condition number in the latter case is still acceptable, it indicates the trend towards an ill-condition.

Table 9.1.

	Gap	Quotient Matrix			Condition Number k_E
Case (a)	2.8311°	.1052708 .0628882 0	.0862352 -.6993138 .0101056	-.0205346 -.0215445 .650712	7.02321
Case (b)	.0674°	1.631816 -10.70067 9.942525	-1.068623 34.51363 -29.60374	-3.711639 -1.489695 1.302242	73.0026

One might suggest that the bilinear conditioning could be incorporated in the Newton-Raphson iteration as a constraint condition. But this is not desirable for two reasons. The first is that in the beginning of the iteration the correction steps $d\bar{\phi}^n$ are quite large, while the bilinear conditioning steps need to be small. The second is that there is no need to. Imagining the convergence paths of all possible constellations in Figure 10.3b, then it is clear that the previous Newton-Raphson routine always follows the best available path anyway.

10.6. Convergence Disks

The regions in which the different series are valid are the convergence disks. During the iteration, only the covering of circular boundary of the s -plane is necessary. While the Frobenius disks are prescribed by the centers s_{ai} , the remaining gaps must be covered by Taylor or Laurent disks.

The Laurent disks are introduced to prevent too many small Taylor disks starting from the tiny at crowded points. We have constructed a routine that seeks clusters of points that are suitable to be enclosed by a Laurent disk, which is an annulus. Suitability is defined as a prescribed ratio of at least 2 of r_o/r_i . For each cluster, the Laurent disk information is placed in the Laurent regions table, until all possible clusters are exhausted. By definition of clusters, it may happen that Laurent disks lie within another Laurent annulus. The still remaining gaps are covered by Taylor disks. In each gap, as few as possible Taylor disks are placed on the circle, with the constraints of the nearest singular point on either side of the gap, as well as other singularities on the circle. It is important that the numerical radius of convergence is > 0.5 times the theoretical, so that consecutive Taylor disks away from a tiny Frobenius disk will become larger.

Any open regions within the unit s -disk are not covered during iteration.

At the end of this routine, the disk $F1$ is chosen as reference and a sequence of match points is established and entered in a match table to be used when matching of the series is done. For each iteration step, new tables have to be set up. In the Quotient matrix method, new tables have to be set up even for each difference step. It is therefore imperative that this covering is done automatically during iteration.

The boundary disks only have to touch each other. Only for the full disk covering is an overlapping better. Only at the application of the iterated converged result, additional Taylor disks are inserted to cover the remaining open spaces. This is not part of the iteration routine and we have not programmed such a routine. Instead we enter suitable Taylor disk centers as input interactively on the screen. As visual aid, three different colors are used for the three different types of disks. A suitable set is then placed in the data tables; see Section 4.4.

10.7. Results

The convergence of the polygon of Figure 10.1a is shown in Figure 10.5a, and that of Figure 10.1b in Figure 10.5b. In many practical applications accuracy of 10^{-3} is quite sufficient, and

this is achieved in six iterations. Convergence accuracy of 10^{-5} was achieved in 10 iterations for Figure 10.5a, and 10^{-6} was achieved in eight iterations for Figure 10.5b. It is obvious that our approach is cautious rather than fast.

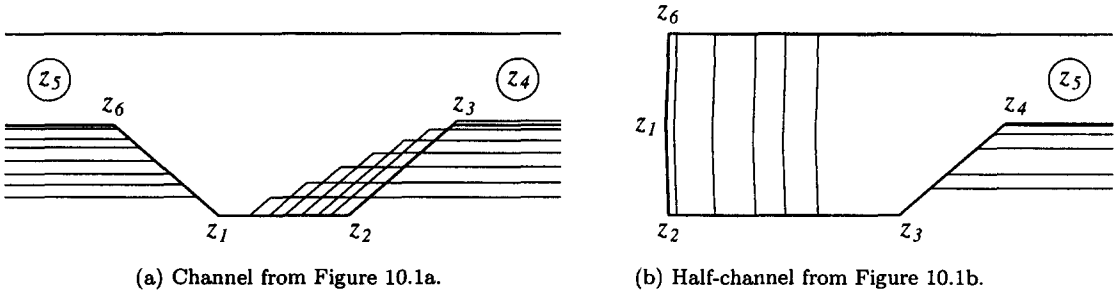


Figure 10.5. Iterated polygon convergence.

To shorten computation time, we start with a small convolution number length, typical 6. Then as soon as clipping is released, the number is increased to a final value, typical 20. This is the advantage of the convolution number, that length can be changed so easily within the maximum storage designated initially. If after the change the error increases again, clipping will just resume, and be released again at a later stage, no harm done. In the Quotient matrix method, we start with a rather large step size $\Delta\phi$, and decrease it to a small value as soon as clipping is released. These two measures correspond to change of integration step size and selection of best suited Quotient step size in a solver package of the numerical integration method [51].

We also note that the Quotient matrix has often off-diagonal terms that are orders of magnitude larger than the diagonal. Therefore, any scalar, or linear, method that uses in effect diagonal terms only will pay dearly in terms of number of iterations.

10.8. Symmetric Polygon

Symmetric polygons appear often enough in practice to warrant separate treatment to take advantage of the almost halving of computations. As an example, we take the same polygon of Figure 10.1a and pose it as symmetric polygon, shown in Figure 10.6a. Only the three angles ϕ_2 , ϕ_3 , and ϕ_4 have to be iterated. Using point 1 as reference for \hat{c}_1 ; the distribution matrix is

$$\underline{\underline{D}}_v^n = \begin{bmatrix} 0 & 0 \\ 0 & 0 \\ 1 & 0 \\ 0 & 1 \\ 0 & -1 \\ -1 & 0 \end{bmatrix}. \quad (10.31)$$

There are only $n_v = 2$ degrees of freedom left. Two angles are changed in the construction of each column of the Quotient matrix, still according to equation (10.28) but with the new $\underline{\underline{D}}_v^n$ matrix of equation (10.31).

In the symmetric case, only the upper half of the boundary has to be covered by convergence disks during iteration, and only those expansions have to be done. In any evaluation of the function $w(s)$ inside the circle, the full covering is again necessary because $w(s)$ may still be unsymmetric in a symmetric polygon. If the number of points s_i on the axis is n_a , which may be 0, or 1, or 2, then the half boundary has the number of points

$$n_k = \frac{(n + n_a)}{2}. \quad (10.32)$$

The three fixpoints due to Riemann's mapping theorem are reduced by one if the symmetry about the axis is fixed. The remaining two fixpoints are kept symmetric, therefore only one symmetric

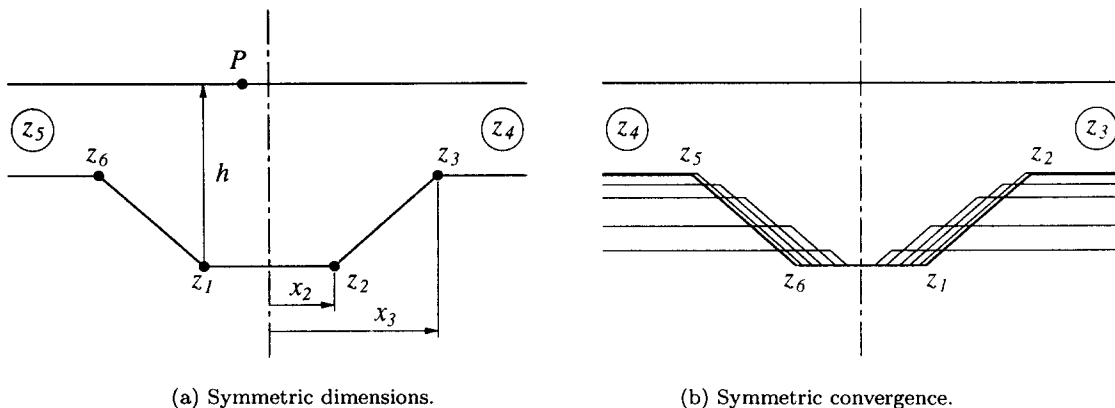


Figure 10.6. Symmetric polygon channel.

fixpoint has to be chosen. The degrees of freedom are then

$$n_v = \frac{(n - n_a)}{2} - 1. \tag{10.33}$$

For example, treating the rectangle as symmetric leaves only one degree of freedom which is reflected in the modulus k of elliptic integrals.

The symmetric constellation of $\overline{\phi}^n$ is due to the fact that symmetry can be kept invariant during transformation $z(s)$. Therefore, the bilinear conditioning must be done by a symmetric routine that searches for the two smallest gaps only above the symmetry axis, and allows only axial displacement $\Delta \hat{b}$.

We have made another set of experiments with a full overdetermined H-matrix of the symmetric points, and it confirmed that the best fixpoint is nearly normal to the axis. It may depend on the number n_a of points on the axis, but it is not worthwhile to make that distinction in the selection of the fixpoint. Therefore, for the symmetric case, another fixpoint routine is implemented that seeks the point nearest to the normal to the axis. Note that the final constellation is independent of the fixpoint. For example, the symmetric triangle, with zero degrees of freedom, will be mapped on equally 120° spaced points on the circle due to bilinear conditioning.

The symmetric convergence of the polygon in Figure 10.6a is shown in Figure 10.6b. Accuracy of 10^{-3} was achieved in seven iteration steps, and convergence of 10^{-6} in nine iteration steps.

10.9. Jacobian Matrix

The Jacobian matrix in equation (10.29) is

$$\frac{dz}{d\phi} = \begin{bmatrix} \frac{\partial z_1}{\partial \phi_1} & \cdots & \frac{\partial z_1}{\partial \phi_n} \\ \vdots & \ddots & \vdots \\ \frac{\partial z_n}{\partial \phi_1} & & \frac{\partial z_n}{\partial \phi_n} \end{bmatrix}. \tag{10.34}$$

A Jacobian matrix is actually square, therefore we will call the analytical version of the H-Matrix in equation (10.29) the Jacobian H-Matrix if the distinction is necessary.

While the Quotient matrix is computed by known right-hand sides of equation (10.29), for the analytical Jacobian it is the other way round: the partial derivatives are determined first. The partial derivatives are transformed to analytical complex derivatives by the transformation

$$\frac{\partial z_k}{\partial \phi_j} = \frac{\partial z_k}{\partial s_j} \frac{ds_j}{d\phi_j} = \frac{\partial z_k}{\partial s_j} \hat{i} s_j, \tag{10.35}$$

where the complex derivative is the derivative of equation (10.15)

$$\frac{\partial z_k}{\partial s_j} = \frac{\partial \hat{c}_1}{\partial s_j} + \frac{\partial \hat{c}_2}{\partial s_j} I_k + \hat{c}_2 \frac{\partial I_k}{\partial s_j}. \quad (10.36)$$

But we never use the integrals at the corners s_k , which is clear when we review the procedure of Section 4.3 to compute I_k by matching of the series expansions. The integrals I_k are obtained from the series integration without a specific constant first, a function which we designate now by $F_k(s)$, and integration f_{0k} constants are found from matching. Let us define the notation

$$F(s) \equiv \int \prod_{i=1}^n (s - s_i)^{-\alpha_i} ds + f_{0k}, \quad (10.37)$$

$F_k(s)$ = expansion of the SC-function in disk k ,

$$F_k = F_k(s_k),$$

$$I_k(s) = F_k(s) + f_{0k},$$

$$I_k = I_k(s_k).$$

At all finite corner points s_k the functions $F_k(s_k) = 0$, and we use point 1 as reference, $f_{01} = 0$. Therefore $I_1 = 0$, $I_k = f_{0k}$. If point 1 is an infinite point, we use $f_{01} = 0$ anyway. To get the integration constant in a disk at point k from a previous disk in the matching sequence at point r , we use a matching point s_m in the overlapping region, where the series values are set equal, $I_k(s_m) = I_r(s_m)$, so that

$$f_{0k} = F_r(s_m) + f_{0r} - F_k(s_m).$$

Therefore, the corner integrals are actually determined by the functions at the matching points by the sequence of matching

$$I_1 = 0, \quad (10.38)$$

$$I_2 = F_1(s_m) - F_2(s_m),$$

$$\vdots$$

$$I_k - I_r = F_r(s_m) - F_k(s_m), \quad (10.39)$$

where s_m is a different value in every matching equation. Finite values of I_k in the equations above corresponding to infinite corners are simply ignored in equation (10.15).

Similarly, we define the notation

$$\frac{\partial F_k}{\partial s_j} = \text{expansion of the Leibniz integral in disk } k,$$

$$\frac{\partial F_k}{\partial s_j} = \frac{\partial F_k(s_k)}{\partial s_j},$$

$$\frac{\partial I_k(s)}{\partial s_j} = \frac{\partial F_k(s)}{\partial s_j} + l_{0k},$$

$$\frac{\partial I_k}{\partial s_j} = \frac{\partial I_k(s_k)}{\partial s_j},$$

where the integration constants l_{0k} are found by the same matching of the Leibniz integral functions. Therefore,

$$\frac{\partial I_1}{\partial s_j} = 0, \quad (10.40)$$

$$\begin{aligned} \frac{\partial I_2}{\partial s_j} &= \frac{\partial F_1(s_m)}{\partial s_j} - \frac{\partial F_2(s_m)}{\partial s_j}, \\ &\vdots \\ \frac{\partial I_k}{\partial s_j} - \frac{\partial I_r}{\partial s_j} &= \frac{\partial F_r(s_m)}{\partial s_j} - \frac{\partial F_k(s_m)}{\partial s_j}. \end{aligned} \quad (10.41)$$

From equation (10.37)

$$\frac{\partial F}{\partial s_j} = \frac{\partial}{\partial s_j} \int \prod_{i=1}^n (s - s_i)^{-\alpha_i} ds. \quad (10.42)$$

From Leibniz' formula we get

$$\frac{\partial F}{\partial s_j} = \alpha_j \int (s - s_j)^{-\alpha_j - 1} \prod_{i \neq j}^n (s - s_i)^{-\alpha_i} ds \equiv J_j(s), \quad (10.43)$$

which is a SCT integral that can be evaluated by the same method as the original integral in equation (10.13). Let us refer to the l.h.s. as the Leibniz derivative, and the r.h.s. as the Leibniz integral.

To our knowledge, no record exists of evaluating the integral in equation (10.43) to obtain the Jacobian directly. The nearest to a numerical evaluation of the analytical Jacobian is presented by Chuang *et al.* [8], who give equation (10.42), but do not continue to the Leibniz integral. Instead, they use an interpolation formula to obtain the derivative from five varied computations of I_k , which means that they use five times as many computations as are necessary to compute the derivative directly from equation (10.43).

The Leibniz integrals $J_j(s)$ are computed by convolution numbers in terms of Frobenius, Laurent, and Taylor series using the same channels of computation as for the basic SC integral. In the computer program, we start each iteration with one computation of the SC integral, with the exponents in equation (10.13), to get the present iterate values of z_k . For later reference, we call this stage of the program the direct mode. Then we use the same covering convergence disks, the same transformation

$$u = \frac{s - s_i}{\rho_i}, \quad (10.44)$$

to compute the Leibniz integral, by simply substituting the exponents of equation (10.13) by those of equation (10.43), and multiplying the result by α_i . We call this stage of the program the derivative mode. The Leibniz integrals $J_{jk} = J_j(s_k)$ are finite when the corner z_k is finite, and infinite when the corner z_k is at infinity, except for the diagonal term $\frac{\partial I_k}{\partial s_k} = J_{kk}$. The analysis of the diagonal term is presented in Appendix C, including the case $\alpha_i = 0$.

The derivatives of the constants in equation (10.36) (which should be seen as variationals in this context to avoid a contradiction of terms) are obtained by taking the derivatives of their mode of calculation. From equations (10.17) and (10.15)

$$\frac{\partial \hat{c}_2}{\partial s_j} = -\hat{c}_2 \frac{\frac{\partial I_B}{\partial s_j} - \frac{\partial I_A}{\partial s_j}}{I_B - I_A}; \quad (10.45)$$

then from equation (10.26)

$$\frac{\partial \hat{c}_1}{\partial s_j} = -\frac{\partial \hat{c}_2}{\partial s_j} \frac{1}{2} (I_O - I_T) - \hat{c}_2 \frac{1}{2} \left(\frac{\partial I_O}{\partial s_j} - \frac{\partial I_T}{\partial s_j} \right). \quad (10.46)$$

The second option for \hat{c}_2 is more complicated. The derivative of equation (10.18) is

$$\frac{d\hat{c}_2}{d\phi_k} = \frac{d|c|}{d\phi_k} e^{\hat{i}\gamma} + \hat{i} \hat{c}_2 \frac{d\gamma}{d\phi_k}. \quad (10.47)$$

From the derivative of the logarithm of equation (10.20), and using equation (10.21), we obtain

$$\frac{d}{d\phi_k} \log |d| - \hat{i} \frac{d\gamma}{d\phi_k} = \alpha_k \frac{\hat{i} s_k}{s_r - s_k}, \quad \text{if } r \neq k, \quad (10.48)$$

$$= \sum_{i \neq k} -\alpha_i \frac{\hat{i} s_k}{s_k - s_i} + \hat{i} (1 - \alpha_k), \quad \text{if } r = k, \quad (10.49)$$

from which $\frac{d\gamma}{d\phi_k}$ is obtained by the Imaginary Part of the r.h.s.

Taking the derivative of equation (10.23),

$$\frac{db}{d\phi_k} + \hat{i} \frac{dh}{d\phi_k} = \frac{\left(\frac{d\hat{c}_2}{d\phi_k} (I_P - I_Q) + \hat{c}_2 \left(\frac{dI_P}{d\phi_k} - \frac{dI_Q}{d\phi_k} \right) \right)}{-\hat{e}_r}. \quad (10.50)$$

In this equation, the value h is a given constant, so that $\frac{dh}{d\phi_k} = 0$. Then $\frac{d|c|}{d\phi_k}$ is extracted from the known Imaginary Part, which completes the values required for equation (10.36).

Finally, for any degenerate dimension h , we use the Imaginary Part of equation (10.50) again, this time with known $\frac{d\hat{c}_2}{d\phi_k}$, to compute $\frac{dh}{d\phi_k}$ on the l.h.s.

The derivatives in the Jacobian H-matrix matrix can now be computed by equation (10.35). This matrix is supplied in the place of equation (10.29), while the iteration steps are computed exactly as in the Quotient matrix method.

The problem orientated routine must now also supply the information about the details of the different options of specifying the constants \hat{c}_1 and \hat{c}_2 so that the appropriate derivatives can be computed in the Main program. Any other options are not permitted unless the derivatives of their construction are added to the Main program. This is quite different from the Quotient matrix Main program which is not concerned about which method is employed.

The symmetric problem routine is much more complicated to construct. The missing Leibniz integrals must be constructed by using certain symmetries. But to obtain these symmetries, the whole complex algebra must be made symmetric as well. For example, the complex logarithms and exponents must be taken on a Riemann plane from $-\pi < \phi < \pi$. In view of our conclusions in Section 10.10 below, we have not completed such a program.

10.10. Results

To verify correct computation, the Jacobian matrix was compiled for a symmetric polygon, showing that the elements are consistent within six digits. Comparison with the Quotient matrix showed that the approximations were correct within two to three digits. Yet the convergence was not significantly affected. In the initial iteration stages the steps are clipped anyway, therefore the better accuracy of the Jacobian matrix is ineffective. Towards the end of the iteration, it seems that the limitation of crowded points is more severe than an accurate Jacobian matrix. Perhaps we may still come across ill-conditioned problems where the accuracy of the analytical Jacobian is an advantage. But in the meantime, we conclude that a well-constructed Quotient matrix is just as effective as the analytical Jacobian matrix in the SCT parameter iteration problem. The approximation of the analytical Jacobian matrix by the Quotient matrix as a means of course does not effect the accuracy of the final analytic solution in terms of series as a result.

10.11. External Polygon

The same Quotient matrix iteration with the H-matrix is applied for the iteration of the external polygon parameters ϕ_i . In [28], it is stated that the balance to eliminate the residue is an additional equation to be satisfied in the parameter problem. But with our construction of \hat{b} according to equation (7.7), \hat{b} is dependent on the parameters ϕ_i , and is computed merely as one additional step in every iteration as well as every column computation of the H-matrix. This is quite similar to the computation of the constants \hat{c}_1 and \hat{c}_2 . The initial value of \hat{b} may be hard to find, but the consecutive values during iteration are close enough, due to clipping, to be found quickly.

Therefore, we need the same three fixed points, and the H-matrix has the same $n - 3$ columns as for the internal problem. In all practical cases there are no infinity points of the external polygon (see Section 7.1), therefore the H-matrix consists of the full $2n$ rows. If there are theoretical infinity points, then there are fewer rows.

The convergence disks must cover the boundary, and there must be a connected sequence to the inner disk at \hat{b} .

An example of the convergence of an external polygon is shown in Figure 10.7. This is the same example of which the boundary disks are shown in Figure 7.1.

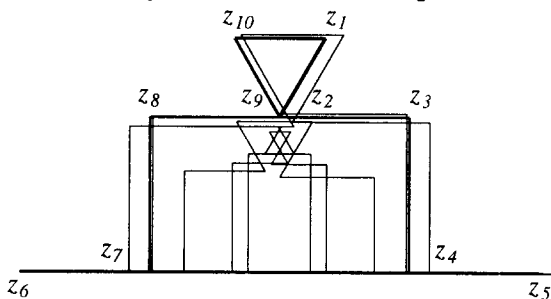


Figure 10.7. Convergence of external polygon.

10.12. Periodic Polygon

To develop a rational method for the periodic polygon parameter iteration, we consider the remaining independent parameters that define the geometric shape of the polygon, if the turning angles α_i are given. To be free from dimensions and orientation, we choose the period $\hat{p} = 1$, which is implemented by the scaling constant

$$\hat{c}_2 = \frac{1}{\hat{p}_I}, \tag{10.51}$$

where \hat{p}_I is the period from the integral before scaling. Starting from point 1, we need one direction relative to \hat{p} . The the last line through point n is then also fixed, then the polygon is defined by $n - 2$ lengths in between. Therefore, there are altogether

$$n_v = n - 1 \tag{10.52}$$

independent parameters, which have to be satisfied by the available parameters in the SCT formula. The available set for variation during iteration is $\overline{\phi}^n, \hat{b}$, which are $n + 2$ parameters; therefore, we will have to fix three of these. Note that the components of \hat{b} do not occur as single complex number in equation (8.1). If we consider that any variation of these parameters which constitute a bilinear transformation, will leave the geometry of the polygon invariant; the safest way is to fix the point \hat{b} during the iteration step. Then we may choose ϕ_1 as fixed third parameter, or some other measure like $\phi_1 + \phi_n$, to fix an axis. In the periodic mapping the

parameter \hat{b} has a special influence, somewhat between being free in the internal polygon and dependent in the external polygon, which causes the unique choice of only one fixed point on the circle. Note that such a choice allows the same procedure down to the smallest possible number of $n = 2$ of the periodic polygon.

To get a better understanding of the influence of the variation of parameters, consider as example the triangular wave, $n = 2$, $\alpha_1 = 90^\circ$, and a choice of $\phi_1 = 0$, $\phi_2 = \pi$ on the circle, as shown in Figure 10.8a. The triangular wave can then vary with its vertex along a circular arc as shown in Figure 10.8b. Any variation of \hat{b} from its shown position along a circular arc through points 1 and 2, indicated by the dotted line, is a bilinear transformation and will not influence the triangular wave. The best variation is therefore a variation in a normal direction, along the shown y -axis. This variation will provide all possible triangular waves with 90° vertex. Now we show how we get exactly the same end result by our iteration procedure, which consists of the following three steps:

- variation of only ϕ_2 in the matrix iteration correction;
- bilinear conditioning—this will bring ϕ_1 and ϕ_2 diagonally opposite each other, and will shift \hat{b} ;
- rotation to bring ϕ_1 back to 0.

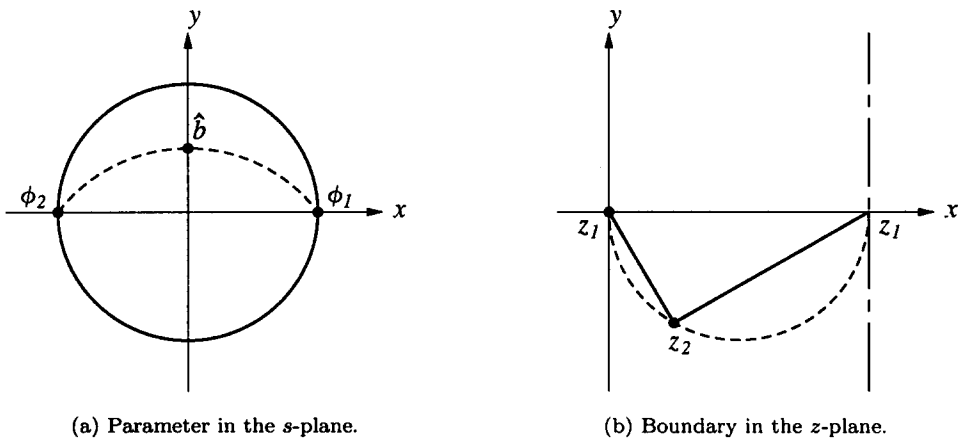


Figure 10.8. Mapping of the triangular polygon wave.

We use the same H-matrix method of specifying all $2n$ coordinates of the n corners with any infinities left out, in the target array \bar{z}^e , and construct the $n_v = n - 1$ columns of the Quotient matrix $\frac{dz}{d\phi}$ as before.

In special cases, no finite length may appear, or perhaps only a very small one. In that case, a slope of a half-infinite line may be given as coordinate. In exotic cases where infinite lines are included, degenerate dimensions will have to be used. These coordinates are all calculated in the problem subroutine; the quotient matrix will simply consider them as numbers and use the corresponding finite differences.

A typical convergence during iteration is shown in Figure 10.9a (not making use of symmetry), and a potential flow in such a polygon boundary is shown in Figure 10.9b.

10.13. Cyclic Internal Polygon

The free parameters are the same as for the periodic polygon, $n_v = n - 1$. Therefore, also the central point \hat{b} and the position ϕ_1 are held constant during the iteration step, then bilinear conditioning is applied. The essential difference compared to the periodic polygon is the selection of a norm. Taking the constant $\hat{c}_1 = 0$ places the center of the polygon at $z = 0$ because the

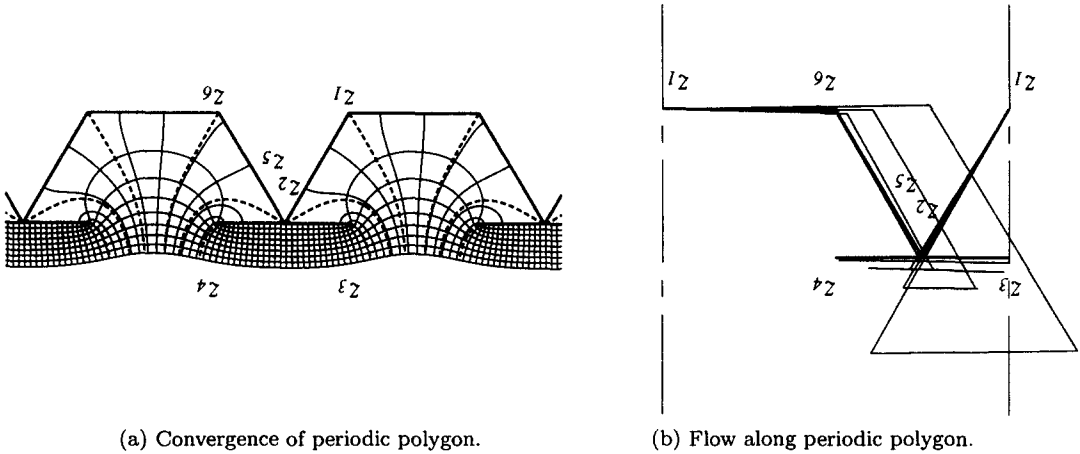


Figure 10.9.

central Frobenius disk is chosen as reference. Then any one point relative to the corners is chosen as fixed. In the example of Section 9.1, the point $(z_1 + z_4)/2 = \hat{z}$ was chosen. The constant \hat{c}_2 is determined accordingly by

$$\hat{c}_2 = \frac{\hat{z}}{(I_1 + I_4)/2}, \tag{10.53}$$

where I_i are the integrals of equations (10.38)–(10.39), in each iteration step and for each Quotient matrix column. All finite coordinates are given as target values for the H-matrix method. Only when exotic infinite corners occur will a slope or degenerate dimension have to be specified.

The smallest number of different corners in a cyclic polygon is $n = 1$, which is the regular m -sided polygon. No iteration is necessary for only that case.

Convergence during iteration of the example in Section 9.1 is shown in Figure 10.10a. The initial conditions were deliberately set unsymmetric.

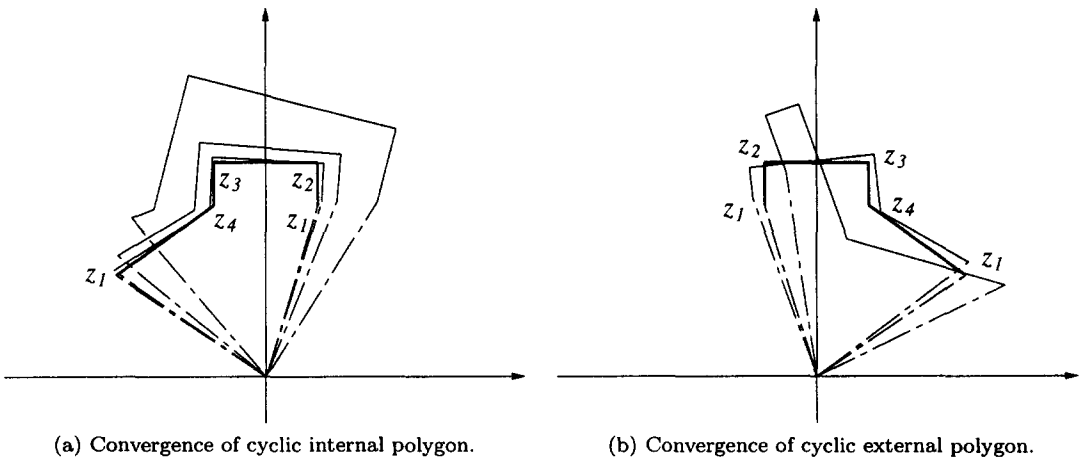


Figure 10.10.

10.14. Cyclic External Polygon

The iteration of the cyclic external polygon follows exactly the same iteration routine as the cyclic internal polygon, with the proper negative number m used for the number of cycles.

Convergence during iteration of the example in Section 9.2 is shown in Figure 10.10b, with the same initial conditions as for Figure 10.10a.

11. CONCLUSION

The Schwarz-Christoffel integral is solved with convolution number algebra for internal, external, periodic, and cyclic polygons. The solution is analytic, relying on a computer environment. The parameter problem is solved with the quotient H-matrix method which simplifies data input for a specific case. The analytical Jacobian matrix is also obtained, but not found to deliver any better results than a well-groomed quotient matrix method, while being cumbersome in programming and data preparation.

Any SCT solution is not quite sufficient for practical purposes yet. The corners that produce infinities of velocity in potential flow, of temperature, magnetic, electrostatic, or electrodynamic fields are physically not possible. In potential flow, the infinities are avoided by separation, or at least smoothed by a boundary layer. In temperature fields, the material is either dissipating heat or melting away. In magnetic fields, the infinite flux is avoided by oversaturation, altering the potential equation, and in alternating magnetic fields by eddy current heating. In electrodynamic fields, the current is heating up the material until the current density is changed to such a finite value that equilibrium between heating and cooling exists, similar to a boundary layer. In electrostatic fields, the dielectric will break down and released current will flow.

True potential solutions are only possible if the convex corners are rounded. This can be approximated for practical purposes by the replacement of a factor in the SC integrand, see [35]. An example of such use appears in [52]. It is beyond the scope of the present treatise to give an analysis of this method in terms of convolution algebra; suffice it to note that corresponding additional singularities appear. Whether more elaborate treatment of curvature, as by Floryan [39], can be treated efficiently with convolution number algebra we cannot predict. Alternatively, as practical approximation the close vicinity of a corner may be mapped locally to a corner with a curve if the radius is small.

A further practical application may be the approximation of other than polygon boundaries. This again may be put into two classes. We agree with Trefethen [3] that polygonal approximation of a boundary with a large number of corners renders the parameter iteration impractical, in our case especially so with the convergence disks that convolution algebra requires. In the past, there were such suggestions, as in [6], without actually executing them, although in [17] Costamagna *et al.* has reported such approximation with up to 100 corners. Instead we propose that a compromise may be useful. Arbitrary boundaries may be surrounded by a polygon, and the SCT will then transform the boundary to a near-circle, from where it can be treated with near-circle iteration methods. For example, all the contours around the external polygon in Figure 7.3a are transformed to circles. In fact, the oldest example is the Joukowski transformation to map an airfoil on a circle. We do not, however, suggest that it may be easy to find a rational method for such an approximation. The computational advantage is that the near-circle region may be sufficiently well approximated by only a central Taylor series. A very short truncated Taylor series has been used by Muskhelishvili [53].

Another class of approximation may be to use the SCT with other than the theoretical SCT sum of angles, resulting in a polygon with curved sides. In Figure 10.11 we show a channel obtained with $n = 2$ corners, 360° on the left end and 180° on the right end. In Figure 10.12 we show a curved side polygon which may be used to map a curved boundary with the same angles at the corners to a smooth near-circle boundary.

It is up to the user to decide whether he prefers the existing efficient numerical solutions that are available or the analytical method that we have presented here as a first attempt and not quite complete—we have not yet got a full-region automatic disk covering routine. To this end, we cannot furnish useful information of computer operating time. Our analytical method has been programmed during the research period and is not optimized. The solution of the parameter problem, in QuickBASIC, takes minutes rather than seconds as reported by Trefethen [3]. During each iteration step we have several screen outputs, particularly color display of all regions and

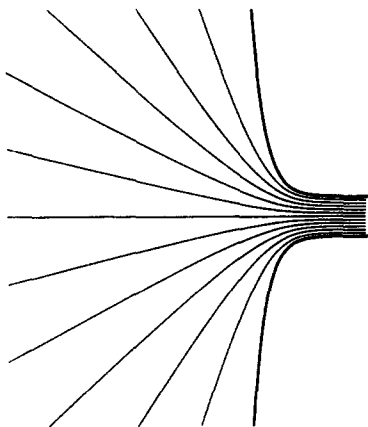


Figure 10.11. Curved boundary channel.

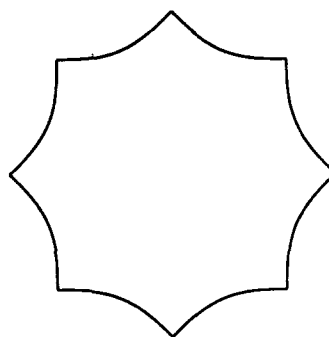


Figure 10.12. Curved boundary octagon.

the present iterated boundary, all of which use time, but during research, time well spent in experiencing the mathematics graphically, as it were.

APPENDIX A SCALED VARIABLE

During the large range of proportions of the intervals between singular points of elliptic integrals or the SCT, convergence disks may range from very small radius ϵ to very large radius $1/\epsilon$. Let the value of the the k^{th} term of a series on the edge of a disk with radius r have the value Δ , which is computed as $\Delta = c_k r^k$. During the expansion, the coefficient will therefore be computed as

$$c_k = \frac{\Delta}{r^k} = \frac{\Delta}{\epsilon^k}, \quad \text{in a small disk,}$$

$$= \Delta \times \epsilon^k, \quad \text{in a large disk.}$$

In the first case, the coefficient c_k may become so large that it may overflow long before the end of the convolution number. In the second case, it may become zero before the end of the convolution number, and a multiplication with r^k will not recover the value Δ .

To alleviate this numerical problem, a scaled variable is used in each disk

$$u = \frac{z}{\rho_i}, \tag{A.1}$$

so that the coefficient comes into a suitable numerical range $c_k \times \rho^k$. For a Taylor and Frobenius disk, we use the radius of the disk as scaling parameter, $\rho = r_T$ and $\rho = r_F$. For a Laurent disk, we have used the inner radius as scaling parameter, $\rho = r_i$, which is of the order of the Frobenius disks inside the Laurent annulus.

Consider the integration of a function with scaled variable

$$h = \int \underline{U} * \bar{g} dz = \rho \int \underline{U} * \bar{g} du = \rho \underline{U} * \bar{f}$$

$$= \underline{U} * \bar{h},$$

where $\bar{f} = \int \bar{g}$ and $\bar{h} = \rho \bar{f}$. Here we have the choice to evaluate the result as $h = \rho \times f(u)$ or as $h = hu$. In the first case, we have a scaled value $f(u)$ available, which may be used to gauge local accuracy. In the second case, we obtain directly an unscaled value of $h(u)$ with global accuracy.

When the inner radius of the Laurent disk $\rightarrow 0$, the scaling will still be appropriate for the enclosed Frobenius series, but not possible for the Laurent series. Also, considering the Laurent

series as the product or sum of two independent series which each has a different radius of convergence, a consistent method of two separate scaling parameters can be used. The product and separation in Section 2.2 must then be adapted to obtain new separated series

$$a(u) \times b(v) = g(u) + h(v). \quad (\text{A.2})$$

Let the scaled variables be

$$\begin{aligned} u &= \frac{z}{\rho}, & \text{for the Taylor series,} \\ v &= \frac{z}{\gamma}, & \text{for the half-Laurent series,} \end{aligned}$$

and the two series

$$\begin{aligned} a(u) &= a_0 + a_1u + a_2u^2 + a_3u^3 + \dots, \\ b(v) &= b_0 + \frac{b_1}{v} + \frac{b_2}{v^2} + \frac{b_3}{v^3} + \dots. \end{aligned}$$

The coefficients of the product can be conveniently displayed as in Figure 2.1, from which it can be shown that the separated series

$$\begin{aligned} g(u) &= g_0 + g_1u + g_2u^2 + g_3u^3 + \dots, \\ h(v) &= h_0 + \frac{h_1}{v} + \frac{h_2}{v^2} + \frac{h_3}{v^3} + \dots, \end{aligned}$$

have the coefficients

$$\begin{aligned} g_i &= \sum_{j=0}^{n-i} a_{i+j} b_j \left(\frac{\gamma}{\rho} \right)^j, \\ h_i &= \sum_{j=0}^{n-i} a_j b_{i+j} \left(\frac{\gamma}{\rho} \right)^j. \end{aligned}$$

When the scaled variable occurs in the logarithmic series of equation (2.26), the integration constant C that was chosen for equation (2.26) depends on the scaling parameter ρ . This is irrelevant in the series solution of the SCT, where the scaling parameter in each disk is fixed and integration constants are obtained by matching. But when the same function is evaluated with different scaling parameters, the dependency $C(\rho)$ must be taken into account to obtain the same function values.

Denote the logarithmic series in equation (2.26) by $l_s(z)$, and the exponent $\alpha + m = \epsilon$,

$$\int z^{-1+\epsilon} dz = -\frac{1}{\epsilon} + \frac{z^\epsilon}{\epsilon} = l_s(\log z). \quad (\text{A.3})$$

The integral of the scaled variable is, using the same value of the constant C consistently,

$$\begin{aligned} \int (\rho u)^{-1+\epsilon} dz &= \rho^\epsilon \int (\rho u)^{-1+\epsilon} du \\ &= -\frac{1}{\epsilon} + \rho^\epsilon \times \frac{u^\epsilon}{\epsilon} \\ &= \rho^\epsilon \left(-\frac{1}{\epsilon} + \frac{u^\epsilon}{\epsilon} \right) - \frac{1}{\epsilon} + \frac{\rho^\epsilon}{\epsilon} \\ &= \rho^\epsilon l_s(\log u) + l_s(\log \rho). \end{aligned} \quad (\text{A.4})$$

The factor ρ^ϵ follows directly from the transformation of the differential, but a log- ρ series, which is the part $l_s(\log \rho)$ in equation (A.4), must be added to keep the integration constant invariant.

APPENDIX B SCHWARZ-CHRISTOFFEL FORMULA FOR THE STRAIGHT PERIODIC POLYGON

Let the angles of the polygon in the z -plane be a, b, c, \dots , measured as in Figure 4.1f, and the exponents $\alpha = a/\pi, \beta = b/\pi, \gamma = c/\pi, \dots$, then

$$\alpha + \beta + \gamma + \dots = 0. \tag{B.1}$$

The mapped points on the circle in the s -plane are $s_a = e^{ia}, s_b = e^{ib}, s_c = e^{ic}, \dots$. To obtain a straight periodic mapping we require that the inside of the circle in the s -plane maps into the half-infinite strip in the z -plane; therefore for $s \rightarrow 0$ we require $z \rightarrow \log s$, and $\frac{dz}{ds} \rightarrow 1/s$. The function that satisfies these conditions is

$$\frac{dz}{ds} = \frac{(s - s_a)^\alpha (s - s_b)^\beta (s - s_c)^\gamma \dots}{s}. \tag{B.2}$$

To prove that the function of equation (B.2) satisfies the conditions on the perimeter, we follow the proof as in [31] for the closed polygon. On the circle $s = e^{i\phi}$, $ds = i e^{i\phi} d\phi$, therefore

$$dz = \frac{(e^{i\phi} - e^{ia})^\alpha (e^{i\phi} - e^{ib})^\beta (e^{i\phi} - e^{ic})^\gamma \dots i e^{i\phi}}{e^{i\phi}} d\phi. \tag{B.3}$$

The factor $e^{i\phi}$ cancels. From each term in brackets like $(e^{i\phi} - e^{ia})$ extract a factor like $e^{i(\phi/2)} e^{i(a/2)}$, and then separate complex and real factors,

$$dz = \hat{C} \left(\sin \frac{1}{2}(\phi - a) \right)^\alpha \left(\sin \frac{1}{2}(\phi - b) \right)^\beta \left(\sin \frac{1}{2}(\phi - c) \right)^\gamma \dots d\phi, \tag{B.4}$$

where the complex constant

$$\hat{C} = i 2 i e^{i(a/2)\alpha} 2 i e^{i(b/2)\beta} 2 i e^{i(c/2)\gamma} \dots$$

and the factor

$$e^{i(\phi/2)(\alpha + \beta + \gamma + \dots)} = 1 \tag{B.5}$$

in view of the sum in equation (B.1). From here the proof carries on as in [31], that equation (B.4) is the equation of a straight line segment in the direction of \hat{C} as long as $\phi > a, b, c, \dots$. The angle ϕ changes from 0 to 2π on the circle. Each time that ϕ becomes larger than the next angle, the factor -1 is extracted from the sin-term, changing the direction of the segment dz by $\pi\alpha, \pi\beta, \pi\gamma, \dots$, at each corner. In the cases where any one of the angles a, b, c, \dots , are outside the range from 0 to 2π , the appropriate multiple of 2π is subtracted in the sin-terms in equation (B.4).

The customary proof for the cyclic periodic polygon uses a transformation of a $1/n$ segment of a circle on the full circle, see [28], which cannot be applied to the straight periodic polygon with infinite n . But the proof for the cyclic polygon can be carried out as above, changing equation (B.1) to the correct sum, $2\pi/n$ for the internal and $-2\pi/n$ for the external polygon, and then dividing in equation (B.2) by a power of s such that equation (B.5), now with an uncanceled factor from equation (B.3), becomes true again. Then it is easy to see that the formula is also true for n not an integer.

APPENDIX C DIAGONAL JACOBIAN MATRIX ELEMENT

In the case of the diagonal of the Jacobian matrix of equation (10.34), the derivative in equation (10.42) is

$$\frac{\partial F_k}{\partial s_k} = \frac{\partial}{\partial s_k} \int (s - s_k)^{-\alpha_k} \prod_{i \neq k}^n (s - s_i)^{-\alpha_i} ds. \quad (\text{C.1})$$

From Leibniz' formula we get

$$\frac{\partial F_k}{\partial s_k} = \alpha_k \int (s - s_k)^{-\alpha_k - 1} \prod_{i \neq k}^n (s - s_i)^{-\alpha_i} ds. \quad (\text{C.2})$$

An alternative expression of the derivative is obtained if we do partial integration first and apply Leibniz' formula to the integral in the second term, with the result

$$\frac{\partial F_k}{\partial s_k} = -(s - s_k)^{-\alpha_k} \int \prod_{i \neq k}^n (s - s_i)^{-\alpha_i} + \int (s - s_k)^{-\alpha_k - 1} \frac{\partial}{\partial s} \prod_{i \neq k}^n (s - s_i)^{-\alpha_i} ds. \quad (\text{C.3})$$

The fact that for finite corners the Leibniz integrals are finite is of no importance because we have to deal with the integral at infinite corners anyway. But there is a different implied constant in the two forms of the derivative. To make this clear, consider the expansion with the transformation

$$u = s - s_k. \quad (\text{C.4})$$

Then equation (C.2) becomes

$$\begin{aligned} \frac{\partial}{\partial s} \int u^{-\alpha_k} \times \underline{U} \cdot \bar{g} du &= \alpha_k \int u^{-\alpha_k - 1} \times \underline{U} \cdot \bar{g} du \\ &= \alpha_k u^{-\alpha_k} \times \underline{U} \cdot \int_{(-\alpha_k - 1)} \bar{g} \\ &= \alpha_k u^{-\alpha_k} \times \left(\frac{1}{-\alpha_k} g_0 + \frac{1}{-\alpha_k + 1} g_1 u + \frac{1}{-\alpha_k + 2} g_2 u^2 + \dots \right) \end{aligned} \quad (\text{C.5})$$

$$\frac{\alpha_k}{1} \rightarrow -g_0 u^{-1} + g_1 \log u + g_2 u^2 + \frac{1}{2} g_3 u^2 + \dots \quad (\text{C.6})$$

Equation (C.3) becomes

$$\begin{aligned} \frac{\partial}{\partial s} \int u^{-\alpha_k} \times \underline{U} \cdot \bar{g} du &= -u^{-\alpha_k} \times \underline{U} \cdot \bar{g} + \int u^{-\alpha_k} \times \underline{U} \cdot \bar{g}' du \\ &= -u^{-\alpha_k} \times \underline{U} \cdot \bar{g} + u^{-\alpha_k + 1} \times \underline{U} \cdot \int_{(-\alpha_k)} \bar{g}' \end{aligned} \quad (\text{C.7})$$

$$= u^{-\alpha_k} \left(-g_0 + \frac{\alpha_k}{-\alpha_k + 1} g_1 u + \frac{\alpha_k}{-\alpha_k + 2} g_2 u^2 + \dots \right) \quad (\text{C.8})$$

$$\frac{\alpha_k}{1} \rightarrow g_1 \log u - g_0 u^{-1} - g_1 + g_2 u^2 + \frac{1}{2} g_3 u^2 + \dots \quad (\text{C.9})$$

Equations (C.5) and (C.8) are the same, but equation (C.8) is well determined for $\alpha_k \rightarrow 0$ while equation (C.5) is not. Equation (C.9) differs from equation (C.6) by the constant $-g_1$, generally

when a logarithmic term $g_m \log u$ is present, by the constant $-g_m$. This is a result of the arbitrary constant implied in equation (2.26). Due to matching in equation (10.41), the constant would still be irrelevant were it not for the occasion that the logarithm may occur in the Frobenius series at the reference point 1. To find out which equation to use, we investigate the meaning of

$$\frac{\partial I_k}{\partial s_k} \approx \frac{\Delta I_k}{\Delta s_k} \tag{C.10}$$

as the quotient of two small quantities, true to the meaning of Leibniz' derivative symbol. In Figure C.1, two overlapping convergence disks at points 1 and k are shown with the variations that produce $\Delta I_k/\Delta s_k$. In each disk, the transformation $u_i = s - s_i$ is used for the convergent Frobenius series

$$F_1 = \int u_1^{-\alpha_1} \prod_{i \neq 1}^n (u_1 + s - s_i) du, \tag{C.11}$$

$$F_k = \int u_k^{-\alpha_k} \prod_{i \neq 1}^n (u_k + s - s_i) du. \tag{C.12}$$

The corner integral at point k is determined, according to equation (10.39), by the difference of the functions at the matchpoint

$$I_k - I_1 = F_1(s_k, u_{m1}) - F_k(s_k, u_{mk}). \tag{C.13}$$

The matchpoint is s_m , which is a distance u_{m1} from point 1 and a distance u_{mk} from point k , such that $s_k = u_{m1} - u_{mk}$. The point k is now moved by the amount ds_k to position $s_k + ds_k$. The difference in the functions F_i is due to the change of parameter s_k , but also due to change of distances u_{mi} , therefore

$$\begin{aligned} \frac{\partial I_k}{\partial s_k} - \frac{\partial I_1}{\partial s_k} &= \left. \frac{\partial F_1}{\partial s_k} \right|_{u_{m1}} (s_k, u_{m1}) + \left. \frac{\partial F_1}{\partial u_1} \right|_{s_k} (s_k, u_{m1}) \times \frac{du_{m1}}{ds_k} \\ &\quad - \left. \frac{\partial F_k}{\partial s_k} \right|_{u_{mk}} (s_k, u_{mk}) - \left. \frac{\partial F_k}{\partial u_k} \right|_{s_k} (s_k, u_{mk}) \times \frac{du_{mk}}{ds_k}. \end{aligned} \tag{C.14}$$

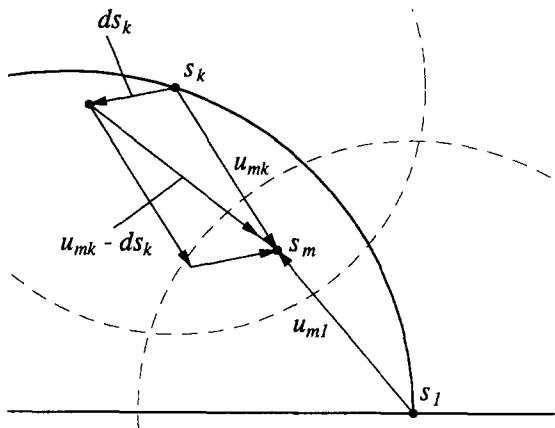


Figure C.1. Differentials in $\frac{\partial I_k}{\partial s_k}$.

We may assume that the matchpoint s_m remains the same. This is no restriction, because according to the convergence of series it does not matter where in the overlapping region the

matchpoint is chosen. Therefore $\frac{du_{m1}}{ds_k} = 0$ and $\frac{du_{mk}}{ds_k} = -1$, and equation (C.14) becomes

$$\frac{\partial I_k}{ds_k} - \frac{\partial I_1}{ds_k} = \frac{\partial F_1}{ds_k} \Big|_{u_{m1}} (s_k, u_{m1}) - \frac{\partial F_k}{ds_k} \Big|_{u_{mk}} (s_k, u_{mk}) + \frac{\partial F_k}{du_k} \Big|_{s_k} (s_k, u_{mk}). \quad (\text{C.15})$$

The first term in equation (C.15) is the Leibniz integral $\frac{\partial F_1}{ds_k}$ according to equation (10.42), because s_k appears in one of the product terms. Therefore we remain with the diagonal derivative

$$\frac{\partial F_k}{ds_k} = \frac{\partial F_k}{ds_k} \Big|_u - \frac{\partial F_k}{du} \Big|_{s_k}, \quad (\text{C.16})$$

which applied to equation (C.12) produces

$$\begin{aligned} \frac{\partial F_k}{ds_k} &= \int u_k^{-\alpha_k} \frac{\partial}{ds_k} \prod_{i \neq 1}^n (u + s_k - s_i) du - u_k^{-\alpha_k} \prod_{i \neq 1}^n (u + s_k - s_i) \\ &= \int u_k^{-\alpha_k} \frac{\partial}{du} \prod_{i \neq 1}^n (u + s_k - s_i) du - u_k^{-\alpha_k} \prod_{i \neq 1}^n (u + s_k - s_i), \end{aligned} \quad (\text{C.17})$$

and these are exactly the terms of equation (C.3) (in reverse sequence) with the transformation of equation (C.4). Therefore, we have the proper form of the diagonal derivative and its geometrical explanation. Equation (C.3) is also well conditioned for $\alpha_k \rightarrow 0$. Take, for instance, the example of $\alpha_k = 0$. Then

$$\begin{aligned} \frac{\partial F_i}{ds_k} &= 0, \quad \text{for all } i \neq k \text{ including } 1, \\ \frac{\partial F_k}{ds_k} &= -g_0. \end{aligned}$$

Therefore

$$\begin{aligned} \frac{\partial I_i}{ds_k} &= 0, \quad \text{for all } i \neq k \text{ including } 1, \\ \frac{\partial I_k}{ds_k} &= -g_0. \end{aligned}$$

Geometrically, this means that the polygon remains in the same position and only the degenerate point k moves. This is obvious because the factor of the degenerate point does not appear in the SCT equation. But if $\alpha_1 = 0$, then due to $I_1 = 0$, the degenerate point cannot move. Therefore, the whole polygon moves in the opposite direction. The derivatives are now

$$\begin{aligned} \frac{\partial F_1}{ds_1} &= -g_0, \\ \frac{\partial F_i}{ds_1} &= 0, \quad \text{for all } i \neq 1; \end{aligned}$$

therefore

$$\begin{aligned} \frac{\partial I_1}{ds_1} &= 0, \quad \text{by definition,} \\ \frac{\partial I_i}{ds_1} &= g_0, \quad \text{for all } i \neq 1, \end{aligned}$$

as expected.

In our applications, the transformation of equation (C.4) is actually replaced by the scaled variable transformation, see Section 2.4 and Appendix A,

$$u = \frac{s - s_k}{\rho}. \quad (\text{C.18})$$

To get the same Jacobian and Quotient matrix element in equation (C.10) when $\Delta s_k \rightarrow 0$, we must include the $\log-\rho$ series, see Appendix A, whenever a logarithm or logarithmic series appears in (C.9). But it turns out that due to the differences being taken in equation (10.41), this is not necessary.

REFERENCES

1. D. Howe, The application of numerical methods to the conformal transformation of polygonal boundaries, *J. Inst. Maths. Applics.* **12**, 125–136 (1973).
2. W. Squire, Computer implementation of the Schwarz-Christoffel transformation, *Journal of the Franklin Institute* **299** (5), 315–322 (1975).
3. L.N. Trefethen, Numerical computation of the Schwarz-Christoffel transformation, *SIAM J. Sci. Stat. Comput.* **1** (1), 82–102 (1980).
4. P. Henrici, *Applied and Computational Complex Analysis, Vol. 3. Discrete Fourier Analysis—Cauchy Integrals—Construction of Conformal Maps—Univalent Functions*, John Wiley, New York, (1986).
5. E. Costamagna, On the numerical inversion of the Schwarz-Christoffel conformal transformation, *IEEE Transactions on Microwave Theory and Techniques* **MTT-35** (1), 35–40 (1987).
6. A. Gilicz, Alternative, useful conformal mapping method can be used for odd-shaped fields, *Oil & Gas Journal* **85** (23), 57–58, 60, 62 (1987).
7. M.A. Chaudhry and R. Schinzinger, Numerical computation of the Schwarz-Christoffel transformation parameters for conformal mapping of arbitrarily shaped polygons with finite vertices, *COMPEL, The International Journal for Computation and Mathematics in Electrical and Electronic Engineering* **II** (1), 263–275 (1992).
8. J.M. Chuang, Q.Y. Gui and C.C. Hsiung, Numerical computation of Schwarz-Christoffel transformation for simply connected unbounded domain, *Computer Methods in Applied Mechanics and Engineering* **105**, 93–109 (1993).
9. L.H. Howell and L.N. Trefethen, A modified Schwarz-Christoffel transformation for elongated regions, *SIAM J. Sci. Stat. Comput.* **11** (5), 928–949 (1990).
10. T.A. Driscoll, Algorithm 756: A MATLAB toolbox for Schwarz-Christoffel mapping, *ACM Transactions on Mathematical Software* **22** (2), 168–186 (1996).
11. D.P. Levinson and A.D. Snider, Optimal trim patterns for low current noise, *The International Journal for Hybrid Microelectronics* **11** (4), 77–80 (1988).
12. Ç. Koç and P.F. Ordnung, Schwarz-Christoffel transformation for the simulation of two-dimensional capacitance,, *IEEE Transactions on Computer-Aided Design* **8** (9), 1025–1027 (1989).
13. E. Costamagna and A. Fanni, Asymmetric TEM cell impedance calculation, *IEEE Proceedings*, (Technical Memorandum) **137** (5), 35–40 (1990).
14. E. Costamagna and A. Fanni, Analysis of rectangular coaxial structures by numerical inversion of the Schwarz-Christoffel transformation, *IEEE Transactions on Magnetics* **28** (2), 35–40 (1992).
15. J.-S. Yang and C.-R. Chang, Magnetic field of an asymmetric ring head with an underlayer, *IEEE Transactions on Magnetics* **29** (2), 2069–2072 (1993).
16. M.A. Martens, R.W. Brown and E.M. Haacke, Conformal mapping analyses of microstrips with circular and elliptic cross-sections, *IEEE Transactions on Microwave Theory and Techniques* **40** (9), 1836–1840 (1992).
17. E. Costamagna, A. Fanni and M. Usai, Slab line impedances revisited, *IEEE Transactions on Microwave Theory and Techniques* **41** (1), 156–159 (1993).
18. V.B. Minuhin, A general solution for the field of polygonal electromagnet, *IEEE Transactions on Magnetics* **29** (6), 4121–4141 (1993).
19. M.D. Meyerson, Conformal mapping and fracture mechanics, *Engineering Fracture Mechanics* **41** (6), 951–953 (1992).
20. W.C. Hassenpflug, Convolution number, *Computers Math. Applic.* **26** (11), 3–135 (1993).
21. P.F. Byrd and M.D. Friedman, *Handbook of Elliptic Integrals for Engineers and Scientists*, Springer, Berlin, (1971).
22. M. Abramowitz and I.A. Stegun, *Handbook of Mathematical Functions*, Dover, New York, (1972).
23. F. Riegels, Formeln und Tabellen für ein in der räumlichen Potentialtheorie auftretendes elliptisches Integral, *Archiv der Mathematik* **2**, 117–125 (1949/50).
24. D. Kücheman and J. Weber, *Aerodynamics of Propulsion*, McGraw-Hill, New York, (1953).
25. R. Bulirsch, Numerical calculation of elliptic integrals and elliptic functions, *Numerische Mathematik* **7**, 78–90 (1965).
26. R. Bulirsch, Numerical calculation of elliptic integrals and elliptic functions, II, *Numerische Mathematik* **7**, 353–354 (1965).

27. T.F. Lemczyk and M.M. Yovanovich, Efficient evaluation of incomplete elliptic integrals and functions, *Computers Math. Applic.* **16** (9), 747–757 (1988).
28. W. von Koppenfels and F. Stallmann, *Praxis der Konformen Abbildung, Die Grundlehren der Mathematischen Wissenschaften*, Bd. 100, Springer, Berlin, (1959).
29. L.M. Milne-Thomson, *Plane Elastic Systems*, Springer, Berlin, (1968).
30. P.V. O'Neil, *Advanced Engineering Mathematics*, 3rd Edition, PWS Publishing, Boston, (1993).
31. L.M. Milne-Thomson, *Theoretical Hydrodynamics*, 5th Edition, Macmillan, London, (1968).
32. R.V. Churchill, *Complex Variables and Applications*, 2nd Edition, McGraw-Hill, New York, (1960).
33. E.T. Copson, *Theory of Functions of a Complex Variable*, Oxford University Press, (1935).
34. Z. Nehari, *Conformal Mapping*, Dover, New York, (1975).
35. P. Henrici, *Applied and Computational Complex Analysis, Vol. 1. Power Series—Integration—Conformal Mapping—Location of Zeros*, John Wiley, New York, (1974).
36. A. Betz, *Konforme Abbildung*, 2nd Edition, Springer, Berlin, (1964).
37. D. Gaier, *Konstruktive Methoden der Konformen Abbildung*, Springer, Berlin, (1964).
38. J.M. Floryan, Conformal-mapping-based coordinate generation method for channel flows, *Journal of Computational Physics* **58**, 229–245 (1985).
39. J.M. Floryan, Conformal-mapping-based coordinate generation method for flows in periodic configurations, *Journal of Computational Physics* **62**, 221–247 (1986).
40. L.C. Woods, *The Theory of Subsonic Plane Flow*, Cambridge, (1961).
41. H. Kober, *Dictionary of Conformal Representations*, Dover, New York, (1957).
42. L.I. Volkovyskii, I.G. Lunts and I.G. Aramanovich, *A Collection of Problems on Complex Analysis*, (Translated by J. Berry), Pergamon, Oxford, (1965).
43. E. Jahnke, F. Emde and F. Lösch, *Tables of Higher Functions*, 6th Edition, Stuttgart, (1960).
44. E.D. Rainville, *Special Functions*, Chelsea, New York, (1960).
45. J. Todd, Editor, *Survey of Numerical Analysis*, McGraw-Hill, New York, (1962).
46. L. Collatz, *Funktionanalysis und Numerische Mathematik*, Springer, Berlin, (1968).
47. S.P. Timoshenko and J.N. Goodier, *Theory of Elasticity*, (Reissue), McGraw-Hill, New York, (1987).
48. Y.S. Kim and H.J. Eom, Fourier-transform analysis of electrostatic potential distribution through a thick slit, *IEEE Transactions on Electromagnetic Compatibility* **38** (1), 35–40 (1996).
49. R. Zurmühl, *Matrizen*, Springer, Berlin, (1964).
50. R.A. Horn and C.R. Johnson, *Matrix Analysis*, Cambridge, (1985).
51. *IMSL User's Manual*, IMSL Customer Relations, Houston, (1984).
52. R. Ramaswami and H.C. Lin, Simulation of time-dependent tunneling characteristics of MOS structures, *Solid State Electronics* **34** (3), 291–299 (1991).
53. N.I. Muskhelishvili, *Some Basic Problems of the Mathematical Theory of Elasticity*, (English Translation by J.R.M. Radok), Noordhoff, Groningen, (1953).